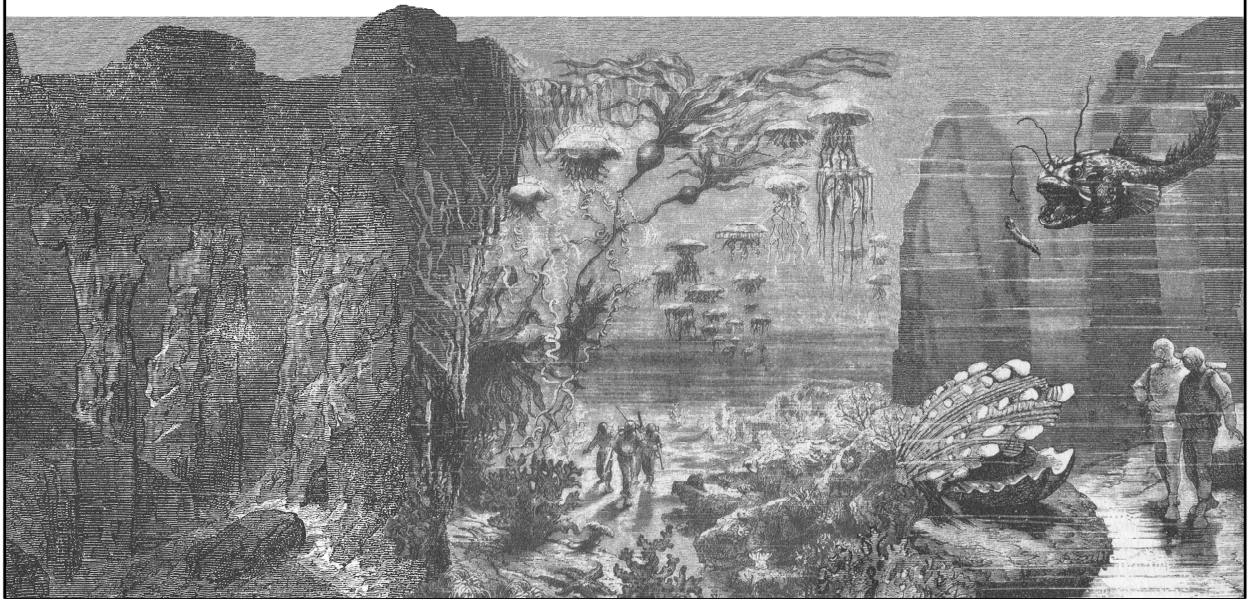GARMT DE VRIES-UITERWEERD

SIGNAL AND BACKGROUND

IN THE UNDERWATER NEUTRINO TELESCOPE ANTARES

Signal and Background in the Underwater Neutrino Telescope ANTARES

Signal and Background in the Underwater Neutrino Telescope ANTARES

Signaal en achtergrond in de onderwater neutrinotelescoop ANTARES

(met een samenvatting in het Nederlands)

Proefschrift

Garmt de Vries-Uiterweerd

Promotor: Prof.dr. P.M. Kooijman

CONTENTS

— Oh ! avec les chiffres on prouve tout ce qu'on veut !
— Et avec les faits, mon garçon, en est-il de même ?

Jules Verne, *Voyage au centre de la Terre*, Ch. VI

1
NEUTRINO ASTRONOMY

1.1 Photons, protons, neutrinos

For centuries man has explored the heavens by looking at the light coming from stars, planets, comets and other heavenly bodies. Until the early 20th century, all information about the universe was gained from the study of visible light (except for the odd meteorite that fell to Earth), and photons have remained the main source of astronomical knowledge, whether they were visible light, radio, X-ray or high energy γ radiation. But since almost a century, another source of information on the cosmos has been available: subatomic particles.

In 1911, Victor Hess discovered that energetic particles observed in the Earth's atmosphere were of extraterrestrial origin [1], a discovery that opened up the field of cosmic ray physics. Cosmic rays are a valuable source of knowledge of the goings-on in stars and other objects.

The study of photons and of charged particles does have some drawbacks, which make it difficult to explore the highest energies and the largest distances with these messengers.

Photons can easily be absorbed by gas clouds or other interstellar matter that they encounter on their way. The longer the distance they travel, the more likely it is that some matter will block their path. Additionally, photons with an energy of about 1 TeV may interact with visible light, creating an e^+e^- pair. More energetic photons can interact with the cosmic microwave background as well. This implies that high energy photons cannot cover large distances.

Protons and other charged particles can of course be absorbed as well, by gas clouds or by interactions with cosmic photons. At energies above $\sim 10^{19}$ eV, the universe becomes practically opaque because of pion production on the cosmic microwave background [2]:

$$p + \gamma \to \Delta^+ \to \pi + N. \tag{1.1}$$

This effect is known as the Greisen-Zatsepin-Kuzmin cutoff.

Also, since protons carry electric charge, they are deflected by the magnetic fields through which they travel. The universe is full of magnetic fields, especially
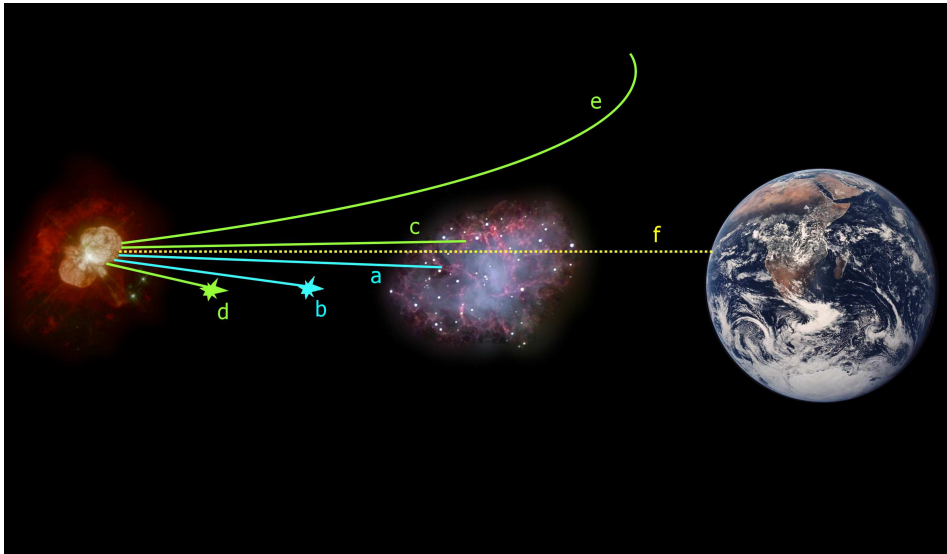
Figure 1.1: *Observing cosmic photons, protons and neutrinos. Photons are absorbed by gas clouds and other interstellar matter (a), or interact with background photons (b). Protons are absorbed by matter (c), interact with background photons (d) or are deflected by magnetic fields (e). Neutrinos are neither stopped nor deflected, and reach the Earth in a straight line (f).*

within galaxies. It is therefore difficult, if not impossible, to pinpoint the exact origin of an extragalactic proton observed on Earth.

Using neutrinos as a means to investigate cosmic processes is a valuable addition to the study of photons and protons. Neutrinos only interact through the weak interaction, which allows them to pass almost any amount of matter without being absorbed. Neither are they deflected by magnetic fields. If a neutrino is observed on Earth, and its direction can be determined, it is immediately clear from which position in the sky the neutrino originated (see Fig. 1.1).

Not only do neutrinos cross the cosmos without being absorbed or deflected, they can also provide information on stellar processes that cannot be gained from the study of protons and photons alone. For instance, there are various models to describe what processes take place in a Gamma-Ray Burst (GRB) [3]. Some of these models call for hadronic interactions, others do not. Observing neutrinos from a GRB is a powerful way to discriminate between these models.

1.2 Observing cosmic neutrinos

While it is an advantage that neutrinos can cross the cosmos without undergoing scattering, absorption or deflection, the fact that they only interact weakly also

means that they are very hard to detect. A large detector is needed in order to have any chance of a neutrino interaction occurring inside it.

Several large volume detectors have been used for this purpose. Kamiokande was originally built as a proton decay experiment, but its biggest achievement was the observation of neutrinos from supernova SN1987A [4] and the detection of solar and atmospheric neutrinos. Other detectors were built specifically for neutrino astronomy: Kamiokande's successor Super-Kamiokande [5] and the Sudbury Neutrino Observatory SNO [6] for instance. The detection strategy in these detectors is to look for Čerenkov light emitted by energetic leptons that are produced in interactions of neutrinos with the target material.

Another strategy used in early neutrino telescopes was to make use of nuclear reactions induced by neutrino interactions. For instance, a chlorine solution was used in the Homestake experiment [7], serving as a target for inverse β-interactions: $\nu_e + {}^{37}\text{Cl} \rightarrow {}^{37}\text{Ar} + e^-$. After a certain irradiation time, the concentration of ${}^{37}\text{Ar}$ was measured, and from this the neutrino flux could be determined.

These detectors were located underground, so as to shield them from muons produced in the Earth's atmosphere, and they were mainly meant to observe solar neutrinos.

As the need for bigger detectors grew, in order to measure the much smaller fluxes from sources outside our solar system, it became less convenient to set up large tanks with homemade target materials. Instead, physicists tried to use targets that were already in place, so that they only needed to install some detection mechanism.

Large detectors were designed to be built in the Antarctic ice (AMANDA [8], IceCube [9]) or in deep water (Baikal [10], ANTARES [11]), with the aim of studying galactic and extragalactic neutrinos. It has even been proposed to use the Earth's atmosphere as a target: the showers induced by neutrino interactions could be measured by air shower arrays like the Pierre Auger Observatory [12].

In the following, we will only consider neutrino detectors in water or ice.

1.2.1 Experimental signature

A neutrino traversing the Earth may interact weakly with nucleons in the atoms of the Earth's material. Interactions with electrons are kinematically disfavoured, and are negligible except at the $\bar{\nu}_e + e^- \rightarrow W^-$ resonance ($E_{\bar{\nu}_e} = 6.3$ PeV). If the interaction takes place in seawater or ice, or in the rock directly beneath it, the interaction products may be observed.

The neutrino can interact by exchanging either a Z boson (neutral current) or a W boson (charged current):

$$\nu_l + N \quad \rightarrow \quad \nu_l + X \tag{1.2}$$
$$\nu_l + N \quad \rightarrow \quad l + X \tag{1.3}$$

In the case of a charged current interaction, a lepton is produced of the same family as the incoming neutrino. These different scenarios give rise to different experimental signatures.

Neutral current interaction

When the neutrino undergoes a neutral current interaction, it transfers momentum to the nucleus with which it interacts. The interaction will, in general, break up the nucleon that is hit by the neutrino, causing a hadronic shower. Only this shower is observed, the neutrino escapes unnoticed (see Fig. 1.2).
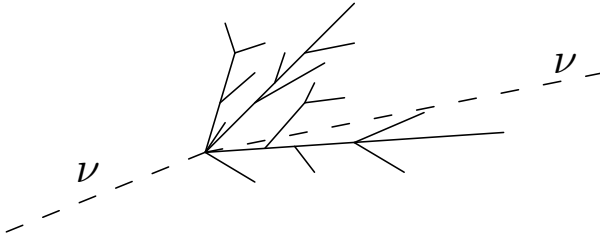
Figure 1.2: *Signature of a neutral current interaction: hadronic shower.*

Charged current interaction of electron neutrino

An electron neutrino undergoing a charged current interaction produces an electron. This highly energetic electron induces an electromagnetic shower, in addition to the hadronic shower from the break-up of the nucleon (see Fig. 1.3).
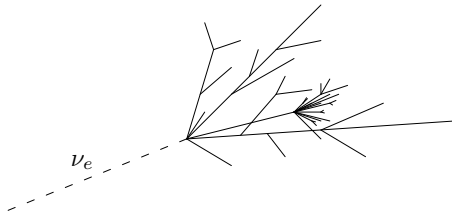
Figure 1.3: *Signature of a ν_e interaction: hadronic and electromagnetic showers.*

Charged current interaction of muon neutrino

In a charged current interaction of a muon neutrino with a nucleon, the usual hadronic shower is produced, as well as a high energy muon. The muon can travel a considerable distance before decaying. Because its speed is larger than the speed of light in the water or ice, it emits Čerenkov radiation. This radiation is emitted under a very specific angle $\theta_{\check{C}}$ with respect to the direction of the muon:

$$\theta_{\check{C}} = \arccos\left(\frac{1}{\beta n}\right), \tag{1.4}$$

where β is the speed of the muon in terms of the speed of light in vacuum, and n is the refractive index of the medium through which it travels.

The Čerenkov radiation from the muon gives a very clean signal, although it may be blurred a bit by the scattering of Čerenkov photons (see Fig. 1.4).
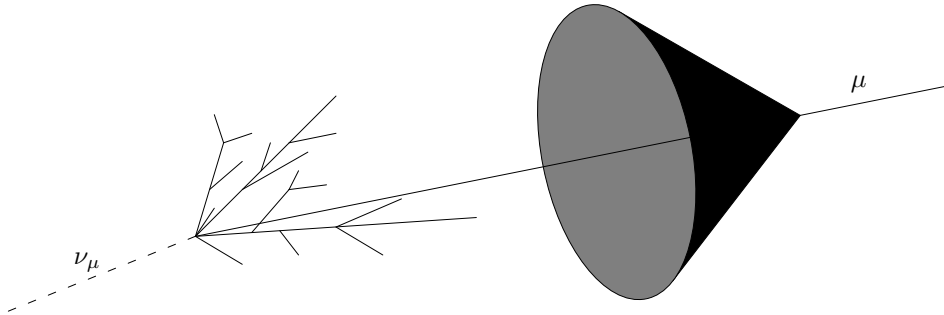
Figure 1.4: *Signature of a ν_μ interaction: hadronic shower and Čerenkov radiation from the energetic muon.*

Charged current interaction of tau neutrino

When a tau neutrino undergoes a charged current interaction, a hadronic shower and a τ are produced. Due to its short lifetime, the τ travels a short distance, depending on its energy, before decaying. Its decay generates a second shower. This 'double bang' signature is evidence of a τ interaction, but it is hard to recognise (see Fig. 1.5).
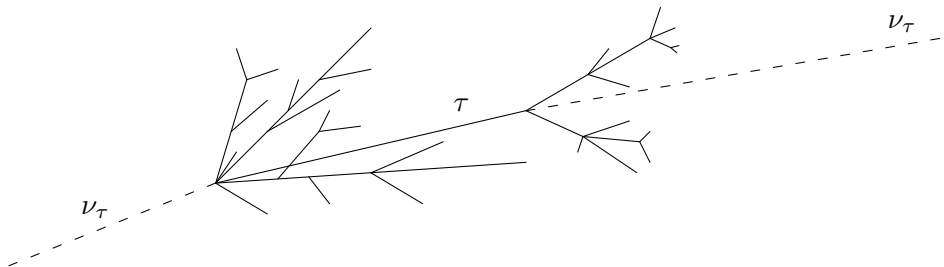
Figure 1.5: *Signature of a ν_τ interaction: hadronic shower and a second shower at the point where the τ decays.*

1.2.2 Standard strategy

The strategy of underwater/ice neutrino detectors is to detect the light produced by the products of a neutrino interaction. In general, such a detector consists of a three-dimensional array of light detectors, usually photomultiplier tubes (PMTs).

The positions of the PMTs and the arrival times of the observed photons are measured, possibly in the form of a waveform of the signal.

Most efforts are focused on recognising muon tracks, since the direction of the muon gives direct information on the neutrino's origin in the sky. From the arrival times of the photons, the muon track can be reconstructed. Additional information, such as pulse heights, may be used to improve the reconstruction.

The considerable length of the track makes it possible to reconstruct the direction with good accuracy. On average, the direction of the muon deviates from that of the original neutrino by an angle of

$$\theta = 1.5° \left(\frac{E_\nu}{1 \text{ TeV}} \right)^{-1/2},$$ (1.5)

where E_ν is the energy of the incoming neutrino. This means that the maximum accuracy with which the direction of the neutrino can be determined is given by this angle θ.

1.3 Physics background

Besides neutrinos from cosmic sources, particles originating closer to home are visible in a neutrino telescope.

Muons are produced when energetic cosmic rays interact with nucleons in the Earth's atmosphere. Muons with a sufficiently high energy can cross the entire atmosphere as well as the water or ice in which the telescope is located, and create a track through the detector. These muons come mainly from close to the zenith, as at larger zenith angles the muon has to cross a larger amount of matter before reaching the detector. This means that all but the extremely energetic muons lose so much energy that it is highly unlikely for them to arrive at the detector. A useful way to eliminate this background is therefore to reject all downgoing muons. Any muon coming from below the horizon must be due to a neutrino interaction.

Neutrinos are also produced as a result of cosmic rays entering the atmosphere. A muon created by an atmospheric neutrino cannot be distinguished from a muon created by a cosmic neutrino. Atmospheric neutrinos form an irreducible background that has to be taken care of statistically when analysing reconstructed muon tracks.

1.4 Low energy neutrinos

The higher the neutrino energy, the more accurate the determination of the original direction can be. Not only is the angle between the neutrino and the resulting muon smaller, but the muon also has a higher energy, hence a longer track length so that it produces more photons, which makes it easier to reconstruct the muon

path. Moreover, the longer muon track increases the effective volume for neutrino detection: muons can be produced farther away and still reach the detector. Also, the cross section is larger at higher energies, again increasing the effective volume. It is therefore altogether reasonable to focus on high energy muons.

However, as will be discussed in more detail in Chapter 4, most cosmic neutrino sources presumably have a neutrino energy spectrum that decreases as a power of E_ν:

$$\frac{dN}{dE_\nu} \sim E_\nu^{-\alpha_\nu}, \tag{1.6}$$

with α_ν typically around 2–3. This means that there are far fewer neutrinos with high energy than with low energy. If somehow these low energy neutrinos could be detected, additional information on processes within cosmic neutrino sources might be gained.

If a sufficiently large number of neutrinos from one direction crosses the detector, it may be possible, using the knowledge of the direction they come from, to detect a signal, even if each individual neutrino does not produce enough light to be detected on its own.

This thesis describes an effort to do just that. It focuses on the ANTARES detector, which is described in Chapter 2. In Chapter 3, the optical background is discussed, and a study of the contribution of bioluminescence to this background is presented. Chapter 4 describes an analysis, based on Monte Carlo simulations, of the possibility to detect a neutrino flux at low energies (1–100 GeV) from a given direction.

Les difficultés astronomiques, mécaniques, topographiques une fois résolues, vint la question d'argent. Il s'agissait de se procurer une somme énorme pour l'exécution du projet. Nul particulier, nul État même n'aurait pu disposer des millions nécessaires.

Jules Verne, *De la Terre à la Lune*, Ch. XII

2

THE ANTARES DETECTOR

The ANTARES[1] collaboration is currently building an underwater neutrino telescope in the Mediterranean, as a first step towards a km^3-scale detector [11]. The ANTARES site is located at 42°50' N and 6°10' E, some 40 km off the French coast, and at a depth of 2400 m (see Fig. 2.1). The ANTARES collaboration unites physicists, technicians and engineers from 24 institutes in seven countries.

The ANTARES detector uses the water of the Mediterranean as a Čerenkov medium. Photomultipliers are deployed in an area of about 0.1 km^2, and the data that are sent to shore are used to search for cosmic neutrinos. Other issues studied by the ANTARES collaboration include searches for non-baryonic dark matter. There is also interest in using the ANTARES infrastructure for measurements in the deep-sea environment.

In this chapter, we will describe the layout of the ANTARES detector, its method of data acquisition, filtering and reconstruction, and the software tools used to simulate the detector response under different circumstances.
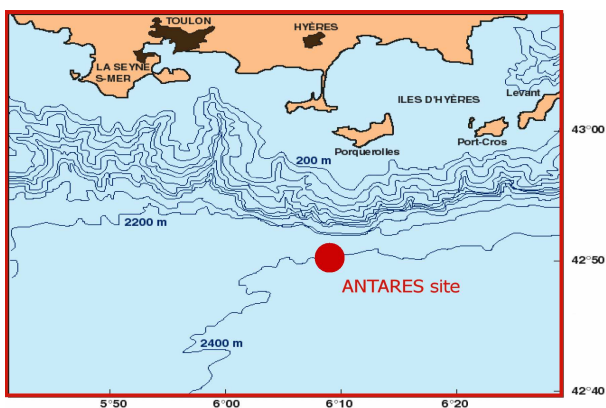
Figure 2.1: *Location of the ANTARES detector.*

---

[1]The name ANTARES is a backronym for 'Astronomy with a Neutrino Telescope and Abyss environmental RESearch', and refers to the star α Scorpii.

2.1 ANTARES layout

2.1.1 Optical Module

The basic building block of the ANTARES detector is the Optical Module (OM). An OM consists of a glass sphere, 17" in diameter, that contains a photomultiplier tube (PMT), the 10" Hamamatsu R7081-20. The PMT has a sensitive area of about 500 cm^2, a transit time spread of about 2.6 ns, and a maximum quantum efficiency of about 25%. A transparent gel is used to glue the PMT to the glass sphere. The gel, which has a refractive index comparable to that of glass, also serves to reduce light reflection on the glass surface.

Besides the PMT, the OM contains the electronics for high voltage supply. The glass of the OM is thick enough (15 mm) to resist the high pressure in the deep sea. The hemisphere behind the PMT is painted black, in order to reduce the sensitivity to photons arriving from that direction. A μ-metal shield protects the PMT from the Earth's magnetic field. The OM is described in more detail in [13]. A photograph of an OM is shown in Fig. 2.2.

Figure 2.2: *A photograph of an Optical Module. The 10" photomultiplier tube, the μ-metal shield and the black paint can be seen inside the glass sphere. The electronics and the connection point are not visible in this photograph.*

2.1.2 Storey

The OMs are grouped together in storeys, with three OMs in each storey. The OMs are mounted on the outside of a titanium frame, the Optical Module Frame (OMF), at 120° from each other. The main axis of the PMT is directed downward at an angle of 45° from the vertical (see Fig. 2.3).

The titanium frame also holds a Local Control Module (LCM), responsible for the distribution of power to the OMs, the digitisation of the OM signal, the processing of the signal, and the transfer of data to shore.

2.1.3 Sectors, strings, detector

The storeys are connected by an Electro-Mechanical Cable (EMC). The EMC provides the mechanical support for the OMFs as well as the means to transport power and signals to and from the storeys. It enters the OMF at the bottom, and
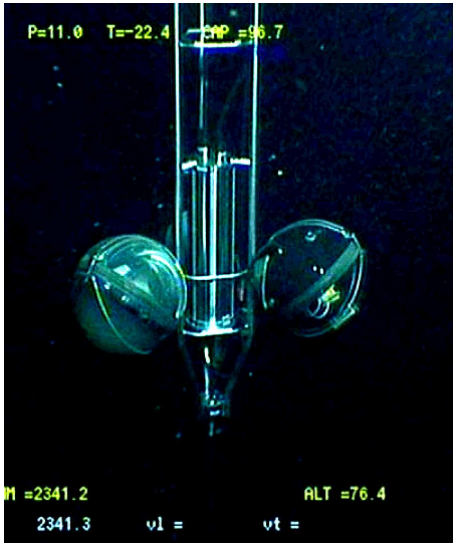
Figure 2.3: *A photograph of a floor, taken from the Remotely Operated Vehicle (ROV) that is used to connect the lines to the Junction Box. [14]*

is connected to the LCM. Another cable leaves the LCM and continues upwards to the next storey.

Storeys are grouped together in sectors of five storeys each. In each sector, there are some additional instruments: a hydrophone for acoustic positioning and a LED beacon for calibration purposes. One of the LCMs in the sector is a Master Local Cluster Module (MLCM), responsible for sending the data to shore.

A string contains five sectors, or 25 storeys. The distance between two storeys is 14.5 m. The bottom of the string is connected to an anchor, attaching it to the seafloor at a fixed position. A String Control Module (SCM), containing electronics for the slow control and the acoustic position calibration system, is attached to the line here. The first storey is placed at 100 m above the seafloor. At the top of the line, a buoy is attached that keeps the string more or less straight. The total length of the string is 463 m.

Finally, twelve strings are distributed in an area of about 200 m diameter, at distances of about 60 m from each other. The total instrumented volume is approximately 0.02 km^3. The EMCs from all the strings are attached to a junction box (JB), from where the main electro-optical cable (MEOC) connects the entire system to the shore.

The overall structure of the detector is shown in Fig. 2.4.

It should be noted that the exact number and spatial distribution of the strings has been subject to change throughout the planning phases of ANTARES. Some of the work described in this thesis was done under the assumption of a 10 string detector, with 30 storeys on each string.
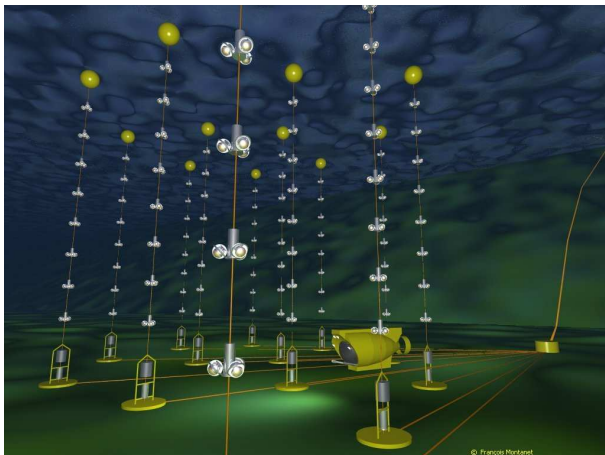
Figure 2.4: *An artist's view of the ANTARES detector.*

2.2 Calibration

In order to be able to reconstruct muon tracks through the detector to less than a degree accuracy, the positions of the PMTs must be known with an accuracy of 10–20 cm. The determination of their positions is done with an acoustic system. At the bottom of each line, in the SCM, there is an acoustic emitter that sends out pulses with a frequency of 40–60 kHz, and in each of the sectors on the line, there is a hydrophone. From the arrival times of the acoustic signals and a measurement of the sound velocity, the hydrophone positions can be calculated.

In addition, each storey contains a tiltmeter and a compass. The observed tilts and orientations of the LCMs, combined with the positions of the hydrophones, are used to reconstruct the shape of the string. With this method, an accuracy of about 10 cm is possible for the positions of the PMTs.

Knowing the relative positions of the OMs is important for the reconstruction of muon tracks. But in order to relate these tracks to astrophysical sources, one must also know the absolute position and orientation of the detector with respect to the Earth.

During deployment, the absolute position of each of the strings (latitude, longitude and depth) is determined with an accuracy of a few metres, which is more than sufficient. The orientation of the detector is determined with an acoustic system, consisting of four transponders located around the detector, at about 100 m from each other, two more transponders at a few kilometres from the detector, and a GPS system on a ship. This allows the orientation to be measured with an accuracy of about 0.1°. This is very accurate in comparison to both the angular resolution of the track reconstruction and the intrinsic uncertainty due to the muon scattering angle.

An independent method to calibrate the detector orientation is to search for the shadow of the moon in the distribution of atmospheric muons over the sky [15, 16]. The primary cosmic particles that create atmospheric muons cannot traverse the

moon, and a lower muon intensity is expected from the direction of the moon. The moon's position is known with a great accuracy. Comparing the position found from the shadow of the moon to its known position will give information on the orientation of the detector.

2.3   Data acquisition

Each of the PMTs in the detector is read out by two so-called Analogue Ring Samplers (ARS), chips that are used for the digitisation of the signal from the PMT. As soon as the voltage from the PMT exceeds a certain threshold, a 'hit' is created by the ARS, containing the charge collected on the anode over a fixed interval of time, and a timestamp provided by the local clock of the LCM. The LCM clocks are regularly synchronised to a master clock. A time-to-voltage converter (TVC) makes it possible to interpolate between two clock pulses. A precision of better than 1 ns can be reached this way.

Dead-time due to the digitisation process is compensated for by using two ARSs for each PMT, and operating them alternately.

The ARS threshold voltage, integration time, and other settings can be adjusted from shore, by configuring the run setup. Typical values are a threshold of 0.3 photo-electrons and an integration time of 30 ns.

The hits created by the ARSs are combined into frames of about 13 ms duration. These frames are then sent to the MLCM, which forwards them to shore via the optical fibres in the cable.

A computer farm located in the shore station combines simultaneous frames from each of the PMTs into 13 ms time slices. Hence, a time slice contains all data from the entire detector during a given time window. Since a muon takes about 2 μs to cross the detector, many separate tracks can be contained in one time slice. The time slices are sent to separate PCs, which analyse the data.

2.4   Triggering

It is important to note that no filtering or triggering is done off-shore, except for the threshold on the PMT voltage. The advantage of this 'all data to shore' concept is that the trigger system can be changed after or during construction of the detector, without the need to recover, adapt and redeploy the hardware that was already in place at the sea floor. Moreover, extra triggers can be built in at a later stage, with different scientific aims [17]. This section describes the standard trigger algorithm.

All data coming to shore are processed in real time by the computer farm in the shore station. The raw data are called level 0 (L0) hits. A first level (L1) trigger algorithm searches for L0 hits that form local coincidences (i.e. two or more simultaneous hits in a single storey), or have a large charge (which can be caused by two photons arriving simultaneously at the same PMT). This cut is based on

the fact that local coincidences are far more likely in the case of photons produced by an energetic muon than in the case of random background.

At the next level, correlations between pairs of L1 hits are searched, where the hits are required to satisfy a causality relation:

$$|\tau| \leq \frac{r}{v_g} + 20 \text{ ns}, \tag{2.1}$$

where τ and r are the time difference and the distance between the two hits, and v_g is the group velocity of light in the seawater. For two photon hits caused by Čerenkov photons from a relativistic muon, $\frac{r}{v_g}$ is the largest possible time difference between the two hits. The additional 20 ns time difference that is allowed in this step of the filter algorithm accommodates scattering and uncertainties in the calibration of the time and position of each hit. Hits that satisfy the causality relation 2.1 form a cluster.

Clusters are required to contain a minimum number of hits. A typical setting for the minimum cluster size is 5 hits. Smaller clusters are discarded.

An additional step can be taken to reduce the random background rate even further. In this special trigger algorithm, all L1 hits that form part of a cluster are subjected to a stricter causality relation, assuming a specific muon direction:

$$\frac{r_{\parallel}}{c} - \frac{r_{\perp}}{c} \tan\theta_{\check{C}} \leq \tau \leq \frac{r_{\parallel}}{c} + \frac{r_{\perp}}{c} \tan\theta_{\check{C}}, \tag{2.2}$$

where $r_{\parallel}$ is the longitudinal distance between the two hits, and $r_{\perp}$ the perpendicular distance. A large number of directions are tried, typically 200, all equidistant in angle.

When all trigger conditions are met, all data within 2 μs (the time it takes for a muon to cross the entire detector) are written to disk for further analysis. The physics events (i.e. the collections of hits) are stored on disk and studied afterwards.

2.5   Reconstruction

Various strategies have been devised to reconstruct the muon track from the times at which the photon hits occur in the OMs. We will outline the general approach, going into some detail regarding photon arrival times, which we will need later.

2.5.1   Track parameters and arrival times

The track of a muon is determined by its position $\vec{x}_0$ at some reference time t_0 and its velocity $\vec{v}$. Since we are only interested in relativistic muons, the speed of the muon is essentially equal to c. The direction $\hat{n} = \vec{v}/c$ can be expressed in terms of two independent variables. The parameters $\vec{x}_0$ and $\hat{n}$ completely determine the muon track.

Because Čerenkov radiation is emitted under a very specific angle $\theta_{\check{C}}$, the arrival time of a Čerenkov photon in a specific OM can be determined from the track parameters of the muon (see Fig. 2.5).
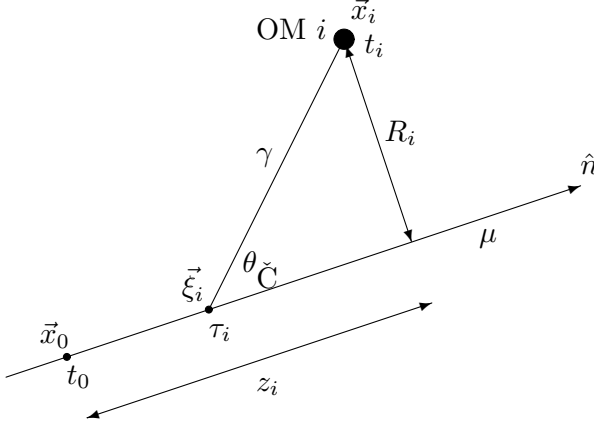
Figure 2.5: *Sketch of an OM detecting a Čerenkov photon. A muon passes through point $\vec{x}_0$ at time t_0, travelling in direction $\hat{n}$ at speed c. At time τ_i, it passes point $\vec{\xi}_i$, where it emits a photon. The photon is detected by an OM at $\vec{x}_i$ at time t_i.*

The muon passes point $\vec{x}_0$ at t_0. At time τ_i, the has reached point $\vec{\xi}_i$:

$$\vec{\xi}_i = \vec{x}_0 + c(\tau_i - t_0)\hat{n}. \tag{2.3}$$

At $\vec{\xi}_i$, the muon emits a Čerenkov photon. The photon reaches OM i, at $\vec{x}_i$, at time t_i:

$$t_i = \tau_i + \frac{|\vec{x}_i - \vec{\xi}_i|}{v_g}, \tag{2.4}$$

where v_g is the group velocity of light in seawater.

The photon is emitted under an angle $\theta_{\check{C}}$ with respect to the muon track:

$$\frac{\vec{x}_i - \vec{\xi}_i}{|\vec{x}_i - \vec{\xi}_i|} \cdot \hat{n} = \cos\theta_{\check{C}}. \tag{2.5}$$

In order to express the arrival time t_i of the photon in terms of the track parameters and OM location, it is convenient to introduce the transverse position R_i, which is the distance from OM i to the point of closest approach of the muon track. It can be written as:

$$R_i = \frac{|\vec{x}_i - \vec{\xi}_i|}{\sin\theta_{\check{C}}}. \tag{2.6}$$

We also introduce the longitudinal position z_i, which is the projection on the muon track of the position of OM i, measured from the reference point $\vec{x}_0$:

$$z_i = (\vec{x}_i - \vec{x}_0) \cdot \hat{n}. \tag{2.7}$$

It follows that

$$|\vec{\xi}_i - \vec{x}_0| = z_i - \frac{R_i}{tan\theta_{\check{C}}}. \tag{2.8}$$

Combining equations 2.3–2.5, and using 2.6–2.8, we find:

$$\begin{aligned} t_i &= t_0 + \frac{1}{c}\left(z_i - \frac{R_i}{tan\theta_{\check{C}}}\right) + \frac{1}{v_g}\frac{R_i}{\sin\theta_{\check{C}}} \\ &= t_0 + \frac{1}{c}(z_i + kR_i), \end{aligned} \tag{2.9}$$

where we introduced the constant

$$k = \frac{c}{v_g \sin\theta_{\check{C}}} - \frac{1}{\tan\theta_{\check{C}}}. \tag{2.10}$$

2.5.2 Maximum likelihood fit

In the standard track reconstruction, the five parameters that define a muon track, $\vec{x}_0$ and $\hat{n}$, are reconstructed from the observed arrival times t_i of photon hits in the OMs. These are expected to be close to the theoretical values given by Eq. 2.9, but may fluctuate due to scattering, transit-time spread in the PMT, and other effects. For a given set of hits, the challenge is thus to find the track that is most compatible with the observed arrival times.

The details of how this is done may vary. A common technique is to use a maximum likelihood fit. In a very simple approach, the likelihood $\mathcal{L}$ of an event (i.e. a set of hits), given a track defined by $\vec{x}_0$ and $\hat{n}$, is:

$$\mathcal{L}(\{t_i\}|\vec{x}_0, \hat{n}) = \prod_i P(t_i|\vec{x}_0, \hat{n}), \tag{2.11}$$

where i numbers the hits in the event, and $P(t_i|\vec{x}_0, \hat{n})$ is the probability for a hit in OM i to occur at the observed time t_i for the given muon track. The best estimate for the track parameters is the set of parameters for which $\mathcal{L}(\{t_i\}|\vec{x}_0, \hat{n})$ is maximal.

More advanced versions of the maximum likelihood technique include hit amplitudes, OM orientations and other variables in the analysis. A thorough treatment of muon track reconstruction is given in [18].

2.6 Simulation of neutrino events

A set of simulation tools has been developed within the ANTARES collaboration to study the response of the detector to an incoming flux of high energy neutrinos. A detailed description of this software is given in [18, 19].

The basic simulation scheme is as follows. First, neutrino interactions with rock or water are simulated. The resulting particles are then propagated to a point close to the detector. The final step is the propagation through the instrumented volume and the tracking of emitted Čerenkov photons.

The end result of the simulation chain is a list of hits in all the PMTs in the detector, giving the measured arrival time and intensity of each hit.

2.6.1 Neutrino interactions

Neutrino interactions are simulated with the package GENHEN [19]. Interactions of high energy neutrinos with rock or water are simulated in a large volume surrounding the detector. The size of this volume depends on the maximum muon range for each given interval of neutrino energy that is simulated. It is chosen such that all possible muon tracks that cause light in the detector are created inside the generation volume. For the highest energies that can be simulated in GENHEN, of the order of 10^8 GeV, this amounts to a generation volume of about $8 \cdot 10^4$ km^3.

The energy spectrum of generated neutrinos follows a power law $E^{-\gamma}$, with γ usually taken to be 1.4. A weight is associated with each event, so other spectra can be studied as well, while still simulating roughly equal numbers of neutrinos in each energy decade.

In the standard version of GENHEN, neutrinos from all upgoing directions are simulated. The distribution of neutrino directions is flat in azimuth, because of the cylindrical symmetry of the detector and the Earth. The probability that a neutrino is absorbed in the Earth before reaching the generation volume increases with the zenith angle: the closer the neutrino direction is to the vertical, the more material it has to cross. This effect is taken into account in the event weights.

For the analysis presented in Chapter 4, a modified version of GENHEN was used, in which the direction of the incoming neutrino is not selected at random, but can be specified by the user. This makes it possible to study neutrinos coming from one particular astrophysical source.

The main type of neutrino interaction is charged current deep inelastic scattering. The neutrino exchanges a W boson with a quark inside a nucleon, changing into a muon. This interaction and the subsequent hadronisation are simulated using the LEPTO package [20].

2.6.2 Propagation to the can

The muons that are produced in the neutrino interactions are propagated to a smaller volume, the so-called 'can'. This is a cylindrical volume that extends a few attenuation lengths around the detector. Its volume is about 0.1 km^3. Only Čerenkov light emitted inside the can needs to be simulated and propagated, any light produced outside the can will not reach the detector.

GENHEN uses the MUSIC package [21] to simulate energy loss and multiple Coulomb scattering of the muon on its way to the can. For neutrino interactions occurring inside the can, no propagation is performed by GENHEN. All the particles that are produced in the interaction are stored and used for the simulation of Čerenkov radiation.

2.6.3 Propagation through the can

The simulation of the muon propagation through the can is performed by the KM3 package [22], using a modified version of MUSIC. At energies less than about

500 GeV, the muon loses energy mainly by ionising atoms in the seawater. The energy loss due to this process is about 0.2 GeV/m. The muon track simulation continues until the muon is stopped or leaves the detector.

2.6.4 Photon generation and detection

Čerenkov photons are generated along the path of the muon. KM3 also simulates the emission, dispersion, absorption and scattering of the photons. The properties of the seawater at the location of the detector are used in the simulation of these processes.

For neutrino interactions inside the can, light from the hadronic shower can also reach the detector. In this case, the GEASIM package [23] is used to simulate the shower and to track individual particles through the detector.

When a photon reaches an OM, the PMT response is simulated. The optical properties of the glass sphere and the optical gel are taken into account, as well as the properties of the PMT, such as quantum efficiency and transit-time spread. Finally, the digitisation of the signal by the ARS chips is simulated.

In addition to Čerenkov photons, the background light from radioactive ^{40}K (see Section 3.1) can be simulated. KM3 simply assumes a fixed ^{40}K rate, to be specified by the user. Hits are generated according to a Poisson distribution, and added to the hits from Čerenkov photons.

Le *Nautilus* flottait au milieu d'une couche phosphorescente, qui dans cette obscurité devenait éblouissante. Elle était produite par des myriades d'animalcules lumineux, dont l'étincellement s'accroissait en glissant sur la coque métallique de l'appareil. Je surprenais alors des éclairs au milieu de ces nappes lumineuses, comme eussent été des coulées de plomb fondu dans une fournaise ardente, ou des masses métalliques portées au rouge blanc ; de telle sorte que par opposition, certaines portions lumineuses faisaient ombre dans ce milieu igné, dont toute ombre semblait devoir être bannie. Non ! ce n'était plus l'irradiation calme de notre éclairage habituel ! Il y avait là une vigueur et un mouvement insolites ! Cette lumière, on la sentait vivante !

En effet, c'était une agglomération infinie d'infusoires pélagiens, de noctiluques miliaires, véritables globules de gelée diaphane, pourvus d'un tentacule filiforme, et dont on a compté jusqu'à vingt-cinq mille dans trente centimètres cubes d'eau. Et leur lumière était encore doublée par ces lueurs particulières aux méduses, aux astéries, aux aurélies, aux pholadesdattes, et autres zoophytes phosphorescents, imprégnés du graissin des matières organiques décomposées par la mer, et peut-être du mucus sécrété par les poissons.

Jules Verne, *Vingt mille lieues sous les mers*, Vol. 1, Ch. XXIII

3

OPTICAL BACKGROUND

The light caused by neutrino interactions and muon tracks in or close to the detector is not the only light to reach the PMTs. Several other phenomena cause photons to be detected. The main sources of background photons are the β-decay of radioactive potassium (^{40}K) in the seawater, and the emission of light by luminescent organisms. Other light sources, such as other radioactive decays or sonoluminescence, are negligible.

It is important to know these sources of optical background, and to estimate the effect they have on the detector performance. Before constructing the complete ANTARES detector, a Prototype Sector Line (PSL) was built, deployed, operated and recovered. This chapter describes the study of the optical background performed with this PSL.

3.1   Potassium decay

One source of optical background is the salt of the sea. Seawater contains 400 ppm of potassium [24], of which the radioactive isotope ^{40}K makes up 0.0117%. ^{40}K has a half-life of $1.28 \cdot 10^9$ years. It decays mainly to ^{40}Ca by emitting an electron (89.3%) [25]. This electron has a maximum energy of 1.311 MeV, and is therefore above the threshold for Čerenkov radiation. Each decay of ^{40}K yields on average about 70 Čerenkov photons in the visible range of wavelengths between 300 and 600 nm [26].

Typically, the light is emitted in random directions due to the multiple scattering of the electron in the seawater. These photons can be observed in the PMTs. Calculations show that the ^{40}K decay produces a steady background rate of single photo-electrons of 30±7 kHz for the 10" diameter tube used in the ANTARES detector. Dark current and radioactive decays in the glass sphere add another 3–4 kHz to this background count rate [26, 27].

3.2 Bioluminescence

Another source of light is bioluminescence: living organisms such as plankton, shrimps and even fish are known to emit light for various biological purposes. We will give a brief overview of the main characteristics of this phenomenon.

3.2.1 Occurrence of bioluminescence

On land, bioluminescence is relatively rare; the luminescent organisms we are most familiar with are fireflies and glowworms. In the oceans, where sunlight does not penetrate deeper than several hundreds of metres, bioluminescence is a very common phenomenon. It is an efficient means of communication in the absence of background light, and since it is impossible for an animal to conceal itself in the open waters, luminescence is important for finding prey or defending against predators. Over 90% of animals living in the deep ocean are luminescent [28]. Strangely enough, luminescent species are almost absent from fresh water environments, even from deep lakes.

In the kingdom Monera[1], some light-emitting bacteria can be found. Among the many classes in the kingdom Plantae, the well-known dinophyceae (dinoflagellates) and two classes of fungi are luminescent. The ability to emit light is shared by none of the 'higher plants'. Bioluminescence is most common in the kingdom of Animalia. We will cite, just to give an impression of the wide variety of luminescent animals, a small selection of classes containing one or more luminescent species: scyphozoa (jellyfish), anthozoa (corals), gastropoda (snails), cephalopoda (squids, octopus, cuttlefish), polychaeta (bristle worms), insecta (insects), holothuroidea (sea cucumbers), and osteichthyes (bony fishes). There are no luminescent amphibians, reptiles, birds or mammals [29].

Since many marine species are luminescent, the biomass density is often a good indicator for the luminescent potential of a stretch of sea. In coastal regions, where a considerable abundance of nutrients is available, the biomass density is relatively high, and bioluminescence is expected to be intense.

3.2.2 Functions of bioluminescence

Bioluminescence is used for various purposes [30, 31]:

Communication This mainly means attracting mates. In some species, only the males can emit light, to which the females are attracted. Firefly males and females perform a complicated exchange of flashes to get together, each species emitting its own specific temporal pattern of flashes.

Finding prey Flashlight fish, for instance, got their name from their use of symbiotic bacteria to emit bright flashes, which enables them to see their prey in an otherwise dark sea.

---

[1]In this enumeration, we adhere to the old taxonomic system used in [29].

Attracting prey Several species of fish, such as the anglerfish, use a luminescent organ as a lure. The prey is attracted by the emitted light and when it comes close enough, the predator strikes.

Deterring predators Some organisms start emitting light when they feel threatened by a predator. This light serves as a 'burglar alarm': the predator becomes visible to its own predators and will, in many cases, withdraw instantly.

Decoy Producing a cloud of luminescent material can confuse a predator, allowing the prey to flee to safety.

Camouflage In relatively shallow waters, where some daylight still penetrates, an animal's silhouette stands out against the dim glow from above. This makes it easy for predators to spot their prey. Some fish and squids have luminescent organs on their bodies, emitting light that matches the colour and brightness of the background glow. This countershading helps them hide from their predators.

3.2.3 Mechanisms of bioluminescence

The light that a luminescent organism emits is produced in a chemical reaction, in which an enzyme called luciferase catalyses the oxidation of a chemical called luciferin. The reaction product, oxyluciferin, can be reconverted to luciferin, a reaction for which energy must be provided, for example in the form of adenosine triphosphate (ATP). The luciferin can be any of various organic molecules. Coelenterazine is most common, other examples are vargulin and reduced riboflavin phosphate. The luciferin and the luciferase can be combined in a single molecule called photoprotein. Adding a particular type of ion (Ca^{2+} is a common example) results in the emission of light [32, 33].

Luminescent body parts can have various configurations, and can be distributed in various ways over an animal's body [31]. The simplest structure is that of a single light-emitting cell, acting as a point source. This is the case for unicellular organisms like dinoflagellates of course, but some larger animals have single luminous cells scattered over their body, either practically uniformly or grouped in particular parts of the body. This pattern is uncommon in 'higher' species like fish, cephalopods and crustaceans.

Luminous substances can be produced in glandular organs, which may or may not be in connection with the exterior. In the first case, the luminous substance can be kept inside the body, or be expelled into the exterior. It is not clear whether luciferin and luciferase are created in separate cells, and only react after being secreted, or if they are created together as a single package of luminescent material.

Finally, many species of fish and some cephalopods possess symbiont glands, in which they keep luminescent bacteria. The host tissue itself is, in most cases, not luminescent at all.
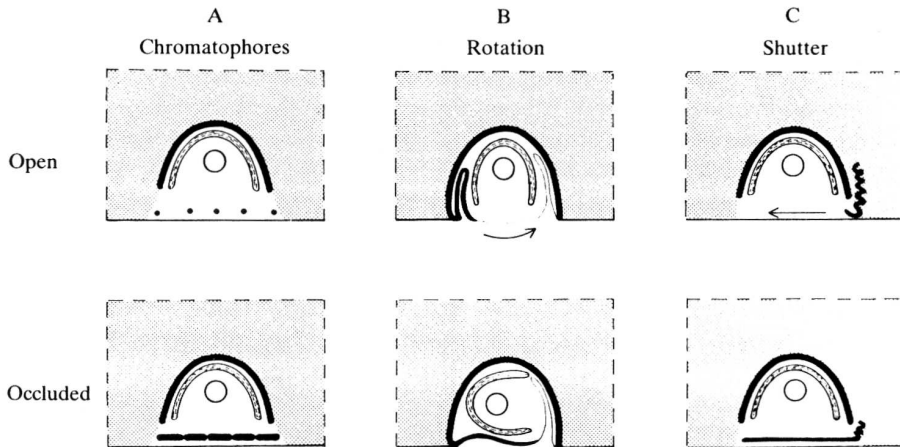
Figure 3.1: *Various mechanisms to regulate bioluminescence: (A) expanding and contracting chromatophores, (B) rotating the luminescent organ, and (C) the use of a pigmented shutter. Figure taken from [31].*

Many species have developed additional structures to regulate the direction of light emission. Pigmented cups and layers of reflecting tissue around light-emitting groups of cells allow for a more directional emission. Lenses, light guides and other collimating structures are also common.

Another feature that can be found in many species is the ability to regulate the timing of light emission. This can be done by using expanding and contracting chromatophores that occlude the photophores, by rotating the luminescent organ into a pigmented pocket, or by the use of a pigmented shutter that is drawn in front of the organ (see Fig. 3.1).

3.2.4 Physical properties of bioluminescence

It must be stressed that it is very difficult, in the lab, to find out what the physical properties of light emitted under natural circumstances are. For many deep-sea organisms, it is impossible to recreate a natural environment under controlled circumstances, and the behaviour observed in the lab may differ greatly from that in the wild [31].

Duration

Luminescent bacteria can emit a faint glow over periods as long as several days. The cell density must be large enough, because the synthesis of luciferase requires a critical concentration of a substance produced in the cells themselves [34]. Also, dinoflagellates have a steady, low intensity emission in addition to the flashes they emit [31]. Other luminescent organisms emit light in brief flashes.

The period of the emitted pulses varies from several milliseconds to a few minutes. Animals that produce the light themselves emit flashes of 50–2000 ms, fish that use bacteria to produce the light typically have longer pulses, of the order of a couple of seconds.

Stimulus and response

Although some species emit a series of flashes in response to a single stimulus, the majority of organisms give a 1:1 stimulus:response ratio. The exact in vivo behaviour of most species is not easy to determine; in the lab the stimuli most commonly used are electric stimuli, and results tend to differ depending on whether only a sample of luminous tissue or the living animal itself is studied. Repetitive emissions as seen in living animals sometimes cannot be reproduced in vitro.

Unicellular organisms emit light as a result of deformation of their cell surface. Multicellular organisms often have neural control over the luminescence.

Intensity

The light produced by luminescent bacteria has a relatively low intensity: about 10^3–10^4 photons per second. Dinoflagellates emit approximately 10^8–10^9 photons per 0.1 s flash reaching a maximum intensity of 10^{10}–10^{11} photons per second. Larger organisms, like jellyfish, octopus and fish can luminesce at an intensity of 10^{11} photons per second for seconds on end.

Wavelength spectrum

Most organisms emit mainly in the blue-green range, where the absorption in water is minimal. The range 450–490 nm is the most common, although some benthic species (i.e. species living at the seafloor) emit at 500–520 nm. This probably has to do with water properties being different close to the seabed. Temporal changes, individual variations and variations between different colonies all occur. Light used for communication between individuals of one species is usually concentrated in a narrow wavelength range, minimising the risk of being noticed by other species (predators). When light is used to search prey, or to scare off predators, the wavelength band is broader. A noteworthy exception to the general trend of emitting green-blue light is that some species of fish emit red light of about 700 nm, which they use as a searchlight to look for prey, without that prey noticing they are being watched.

3.2.5 Summary

To summarise, bioluminescence is very common in marine organisms. An optical background is expected at the location of the ANTARES detector, caused by organisms emitting light either spontaneously or on impact with the detector. The light is emitted in flashes of considerable intensity, at wavelengths for which water is most transparent.

3.3   Data taking with the Prototype Sector Line

Before proceeding to build the entire ANTARES detector, a Prototype Sector Line (PSL) and a Mini Instrumentation Line (MIL) were produced. The goal of these lines was threefold: first, to demonstrate the validity of the design, secondly to obtain experience with the DAQ system as a 'rehearsal' for the complete detector, and thirdly to perform studies of the optical background.

3.3.1   PSL layout and history

The PSL consisted of one sector as described in Section 2.1, with five storeys located at intervals of 12 m (see Fig. 3.2). It was deployed on 22 December, 2002. The MIL, deployed on 12 February, 2003, was equipped with a laser beacon, a LED beacon, acoustic positioning modules and devices to measure sound velocity, current profile, conductivity, temperature, density and light transmission. The PSL and the MIL were connected to the JB on 16 and 17 March, 2003. The PSL was operated until its disconnection and subsequent recovery on 9 July, 2003.

Unfortunately, due to a technical problem, it was impossible to measure individual photons, as had been intended [35]. The fibres in the cable of the PSL were protected by four plastic envelopes, containing twelve fibres each. One of these envelopes developed a fault as a result of the excessive pressure at 2500 m depth, causing strong attenuation in the fibres in this envelope. The signals sent through
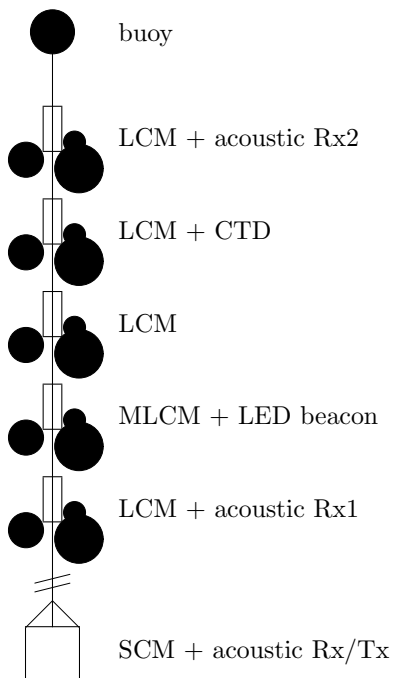
Figure 3.2: *Schematic drawing of the prototype sector line. The bottom of the line is anchored to the seabed and a buoy is attached to its top. Five stories of three OMs each are placed at 12 m intervals. The line also contains several additional measurement devices: a Conductivity-Temperature-Depth (CTD) probe, a LED beacon and acoustic transponders (Tx) and receivers (Rx). The drawing is not to scale.*

the affected fibres could not reach the LCMs; one of these was the clock signal. This made it impossible to synchronise the local clocks, and worse, to start data taking in the way that had been planned, because the command to enable the ARS chips was communicated through the reference clock signal. No hits were recorded at the intended nanosecond accuracy. The fibres in newer strings are protected by stainless steel envelopes, which should prevent this problem from occurring again.

The MIL had the same malfunction in its clock system. Moreover, a leak occurred which flooded two of the LCMs on the MIL. This caused a short circuit in the readout system, effectively disabling the entire MIL.

3.3.2 Determination of count rates

Even if no single photon events could be taken with the PSL, there was still the possibility of measuring count rates at the millisecond scale. Although the ARSs could not be enabled, they still created so-called count rate monitor (CRM) events. The rest of this chapter will be devoted to the study of these count rates.

LCM 3 never gave any data, because of an electrical short circuit. LCM 2 also gave problems; it often crashed and could only be recovered by means of a complete shutdown of the entire detector. No satisfying diagnosis could be made as to why LCM 2 did not work as expected. The data taken by this LCM do not seem to be reliable, and we will not take them into account in this study.

For each OM, a so-called 'precount' p could be set. The value of p could be varied from run to run, by configuring the run settings. Typical values are 10, 50 and 100. Each time the number of hits in the PMT reached this precount, a CRM event was written. Therefore, by looking at the number of events N_{ev} in each timeframe of duration Δt, the count rate f in the OM could be determined:

$$f = \frac{N_{\text{ev}}p}{\Delta t}. \tag{3.1}$$

There is, however, a particularity in the way the data was transmitted, that needs to be accounted for. Each event is 6 bytes long. At the end of the timeframe, the events are sent to shore, but for efficiency reasons, the communication between chip and processor takes place in multiples of 16 bytes. This means that not all the events are transmitted: some are lost in the process, and we do not know the number N_{ev}.

Consider the following example. In a certain 13 ms timeframe, 1358 hits occur in a given OM, where the precount has been set to 100. This means that there are 13 events. These 13 events together are 78 B long. The data are transmitted in multiples of 16 B, so in this case 64 B of data are transmitted, the remaining 14 B are discarded. The 64 B that are sent to shore contain 10 complete events, together 60 B long. The last 4 B are part of the next event, and cannot be used. All in all, 10 events are recorded, giving a count rate of

$$f = \frac{10 \cdot 100}{13 \text{ ms}} = 76.9 \text{ kHz}, \tag{3.2}$$

whereas the true count rate is

$$f = \frac{1358}{13 \text{ ms}} = 104 \text{ kHz}. \tag{3.3}$$

Thus, the count rate is generally underestimated when using the naïve formula 3.1.

We solved this problem in the following way. For all possible values f of the true count rate, ranging from 0 to 1000 kHz, with steps of 0.1 kHz, we sampled a number of hits N_h in a timeframe Δt, according to a Poisson distribution,

$$P(N_\text{h}) = \frac{e^{-f\,\Delta t}(f\,\Delta t)^{N_\text{h}}}{N_\text{h}!}, \tag{3.4}$$

and determined the number of events N_ev:

$$N_\text{ev} = \text{int}\left(\frac{N_\text{h}}{p}\right). \tag{3.5}$$

We then determined the observed number of events N_obs, i.e. the number of events that would be transmitted to shore:

$$N_\text{obs} = \text{int}\left(N_\text{ev} - \frac{(6N_\text{ev})\,\text{mod}16}{6}\right). \tag{3.6}$$

We repeated this calculation 100000 times, and stored the average value of N_obs for each count rate. The average number of events recorded as a function of the count rate is shown in Fig. 3.3, where we used $p = 50$ and $\Delta t = 13$ ms.

To convert an observed number of events N_obs in a given timeframe to a count rate, one could look up the first value of f for which the average observed number of events is equal to or larger than N_obs.

(a) Complete range

(b) Enlarged view at low values
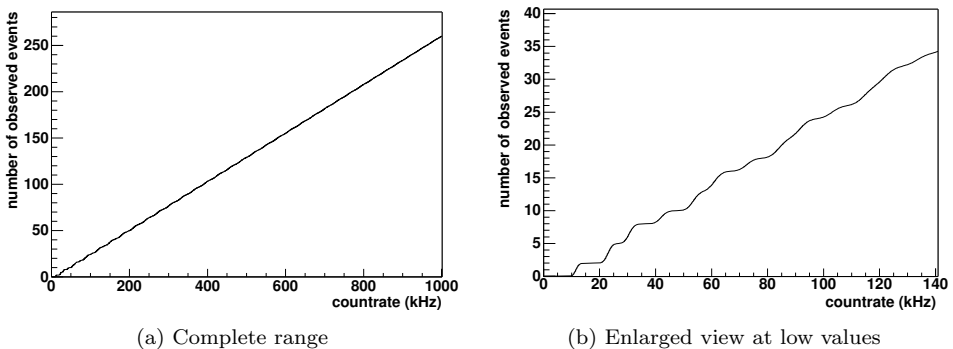
Figure 3.3: *Number of observed events as a function of the count rate.*

However, there are values of N_{obs} for which a small variation in N_{obs} corresponds to a large change in f, so that this method would give rise to wild variations of the observed count rate in these regimes. Instead of considering the observed number of items in a given frame, we therefore take the average value of N_{obs} in 20 consecutive frames. This means that the smallest timescale at which we can study count rates is 0.26 s rather than 13 ms, but this is sufficiently accurate for our purposes, as will be shown later.

Also, instead of taking the one value of f that corresponds to the average number of items $\overline{N}_{\mathrm{obs}}$, we pick f randomly in the interval $[f(\overline{N}_{\mathrm{obs}} - 0.05), f(\overline{N}_{\mathrm{obs}} + 0.05)]$. This smoothes the distribution of observed count rates, which would otherwise show gaps of almost 10 kHz at some places.

In this way, the count rate can at best be determined with an accuracy of about $2.7 \cdot p/\Delta t$, since on average 2.7 different values of N_{ev} are mapped to one and the same value of N_{obs}. For a precount of 50 and a frame length of 13 ms, this amounts to an uncertainty in the observed count rate of 10.4 kHz. This value is comparable to the error that is, for some values of the count rate, caused by the strong dependence of the count rate on the observed number of items.

3.4 Characteristics of PSL data

3.4.1 Time profiles

Some typical time profiles of the count rate are shown in Fig. 3.4. This figure shows the count rate in one particular PMT (PMT 1 on LCM 1), over different periods of 15 minutes each.

Various types of behaviour can be distinguished:

1. There is a steady, relatively low background rate, with occasional 'bursts' of up to several hundreds of kHz, as in Fig. 3.4a.

2. On top of this steady background rate, there are frequent bursts, as in Fig. 3.4b.

3. There are many overlapping bursts, individual bursts can hardly be distinguished, and the steady background is invisible, as in Fig. 3.4c.

4. There are no or few bursts, yet the background is relatively high, as in Fig. 3.4d.

An obvious characteristic of these time profiles is the fact that the count rate (almost) never drops below a certain value. For extended periods of time, it varies around a rather constant 'base rate'. During the entire period of data taking, the minimum observed base rate is about 60 kHz. This is over four standard deviations higher than the predicted rate of 30±7 kHz from ^{40}K (cf. Section 3.1). Subsequent measurements with other lines deployed by the ANTARES collaboration confirm the values measured by the PSL.

(a) Few bursts

(b) Frequent bursts

(c) Many overlapping bursts

(d) High rate, few bursts
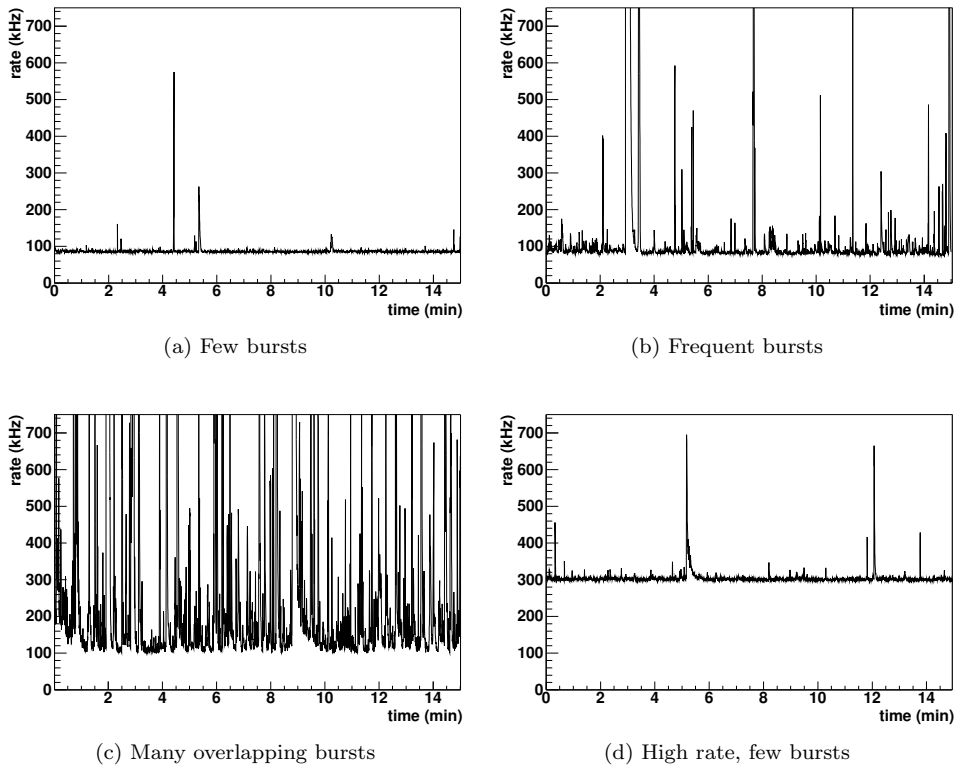
Figure 3.4: *Various typical time profiles of count rates as observed by PMT 1 in LCM 1.*

There are several effects that could explain this discrepancy. The ^{40}K count rate may have been underestimated in the calculations, because one or more of the relevant parameters (angular acceptance of the PMTs, absorption length of light in water, radioactivity in the glass sphere) differed from the assumed value. It is also possible that the observed count rates contain a contribution from steady bioluminescent activity, which always accounts for at least some 30 kHz. Finally, the calibration of the PMTs may have been erroneous. The fact that the observed base rate in a PMT varies with the height of the PMT along the line (cf. Section 3.5) points in this direction. The details of the discrepancy between calculation and observation are still under discussion.

Upon this 'base rate', individual peaks of a relatively short duration are superimposed. Sometimes two or more peaks overlap, and in extreme cases there are so many peaks that the base rate is not visible at all anymore.

These observations lead us to the definition of two quantities, the *base rate* and the *burst rate*. These will allow us to study the behaviour of the background over

longer periods of time, ignoring the individual bursts.

Base rate and burst rate are determined for periods of 15 minutes each. In the course of this time span, the minimum observed count rate does not change dramatically, and it makes sense to define one value of the base rate for the entire period. Of course, both base rate and burst rate are determined for each of the PMTs separately.

3.4.2 Base rate

In Fig. 3.5, the fraction of time that the count rate in a certain PMT is higher than a given value is plotted for the profiles from Fig. 3.4.

There is a clear turning point, at which this fraction starts to drop dramatically. A similar behaviour is observed in all other periods. This motivates the following definition of base rate.
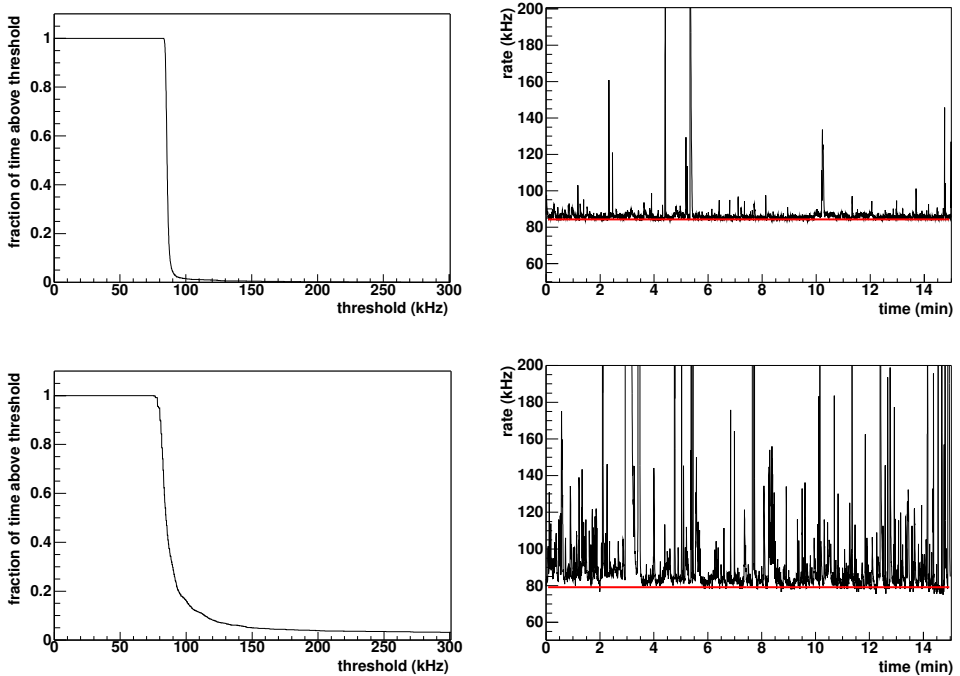
Figure 3.5: *Determination of the base rate. The plots on the left show the fraction of time that the count rate is above a certain threshold, for each of the profiles shown in Fig. 3.4. The plots on the right show the time profiles again, with the base rate indicated by a horizontal line. Note that the scale on the y-axis has been changed in order to show how the base rate depends on fluctuations. (Figure continued on next page.)*
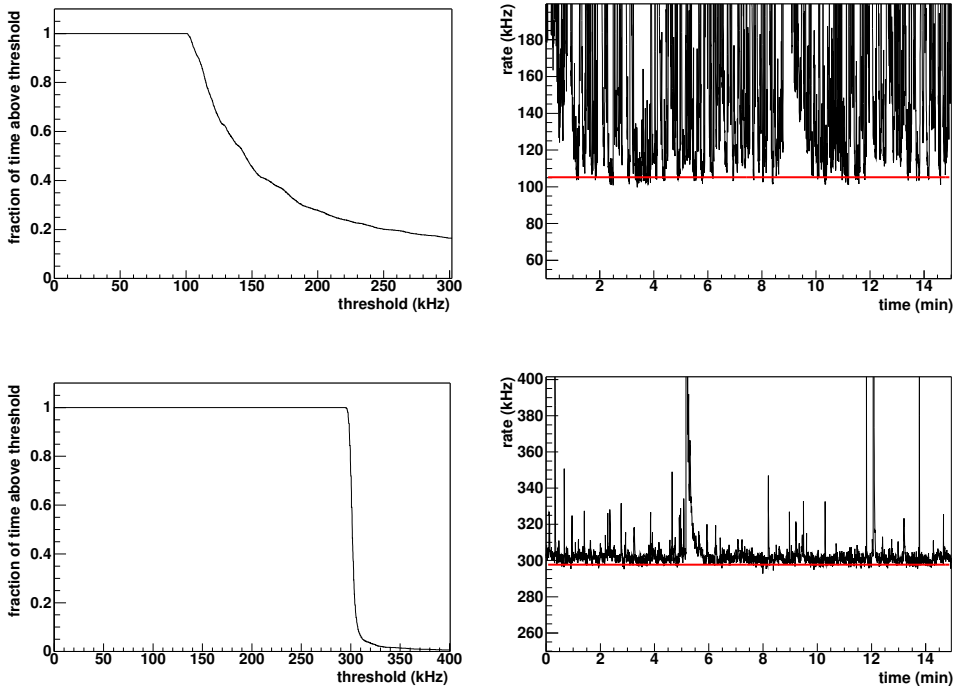
Figure 3.5: *Determination of the base rate (continued).*

We define the base rate as the value $\overline{f}$ for which, during 95% of the time, the count rate in the PMT is higher than $\overline{f}$. In principle, the count rate should never drop below a certain bare minimum, caused by ^{40}K decay and steady bioluminescence, but in practice this does happen occasionally, probably because of hardware or software glitches. Our definition of the base rate nicely eliminates these irregularities.

3.4.3 Burst rate

Within the ANTARES collaboration, a quantity that is often used to characterise the burst behaviour is the so-called burst fraction. This is defined as the fraction of time the count rate is higher than a certain value, typically 200 kHz, or 120% of the base rate, or something similar. It is, however, useful to be able to identify and count individual bursts. This is why we introduce the quantity burst rate, which is simply the number of bursts per unit time, averaged over a 15 minute period.

The challenge is of course to identify individual bursts. We try to do this in the following way.
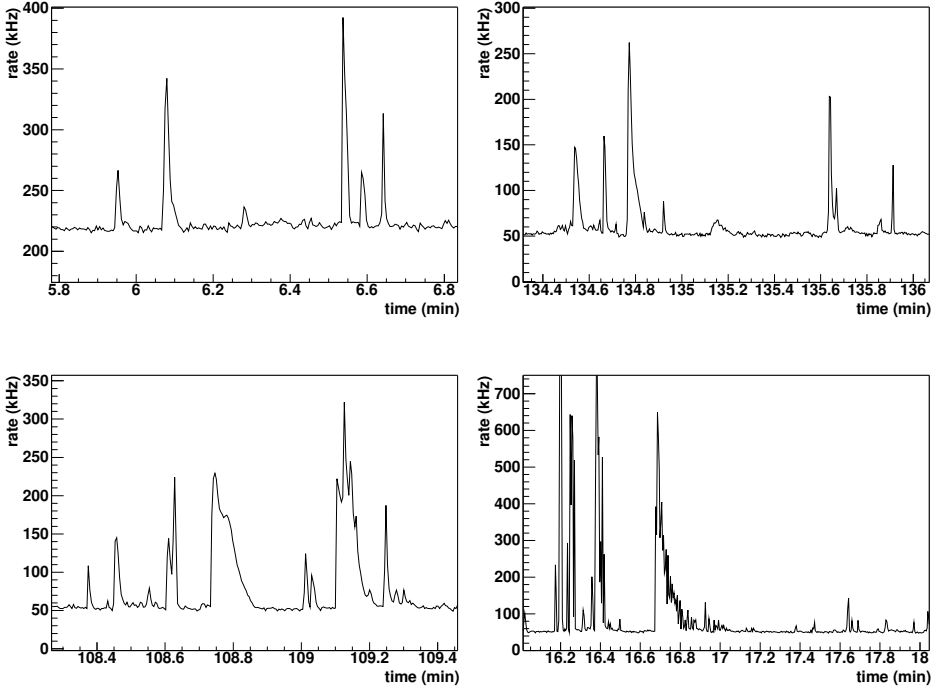
Figure 3.6: *Some examples of bursts.*

Some typical bursts are shown in Fig. 3.6. We notice that bursts typically start with a steep rise, after which they fall off more or less rapidly. It is this steep rise that we will exploit.

We assume that, without any bursts, the count rate would vary around the base rate $\overline{f}$. At any moment in time, the count rate would be a random variable, whose distribution can be described by a Gaussian. The mean of the distribution is equal to $\overline{f}$. The width depends on our method of determining the count rate.

In one time slice of duration τ, the expected number of hits is

$$\langle N \rangle = \overline{f}\tau. \tag{3.7}$$

The spread in the actual numbers of hits observed is

$$\sigma_N = \sqrt{\langle N \rangle} = \sqrt{\overline{f}\tau}. \tag{3.8}$$

We average over 20 consecutive time slices, which results in a decrease of the width by a factor of $\sqrt{20}$. Finally it is the spread in observed count rates we are interested

33

in rather than the spread in observed number of hits. The relevant width is:

$$\sigma_f = \frac{1}{\sqrt{20}} \frac{1}{\tau} \sigma_N = \sqrt{\frac{\overline{f}}{20\tau}}. \tag{3.9}$$

Let us now consider the difference Δf between two consecutive values of the count rate, in other words, the derivative of the time profile. The time profile from Fig. 3.4a is shown again in Fig. 3.7a; its derivative is shown in Fig. 3.7b.

In the absence of bursts and under the assumption of a Gaussian distribution of count rates, the values of the derivative would be distributed according to a Gaussian as well, with mean 0 and width

$$\sigma = \sqrt{2}\,\sigma_f = \sqrt{\frac{2f}{20\tau}}. \tag{3.10}$$

Any deviation would be due to the bursts.

The time profile in Fig. 3.7a features only a few bursts, and the distribution of derivative values is indeed nicely Gaussian, as is shown in Fig. 3.7c.

The profile from Fig. 3.4b and its derivative are shown in Figs. 3.7d and 3.7e, respectively. This profile shows a fairly large number of bursts, which gives a larger spread in derivative values, as is shown in Fig. 3.7f.

We can now go through the time profile, and for each moment determine the difference between the current and the previous count rate. If this difference is large enough, and the previous difference was not, we label this as a burst.

The question is which cut we should use to define a 'large enough' difference. Although a cut at 3σ or 5σ is adequate in most cases, it overestimates the burst rate for values of the count rate where df/dN_{obs} is large (see Fig. 3.3b). In this case, the spread on the observed count rate can be as high as a few kHz, much higher than the value given by Eq. 3.10. A more stringent cut is needed in order to obtain a reasonable estimate for the number of bursts. True bursts, even the smaller ones, stand a good chance of being found with a 10σ or even a 15σ threshold as well. This is illustrated in Fig. 3.8.

Using a 10σ or 15σ cut, we do miss a few small bursts that we would have found with a cut of 3σ, but this is not dramatic, since the larger bursts can still be identified. The effect of the choice of the threshold on the burst rate is shown in Fig. 3.9, where the observed burst rate is shown as a function of the threshold that is used, for each of the four periods from Fig. 3.4. The observed burst rate drops steeply until a threshold of about 3σ. For periods with few bursts, it levels out after 5σ. When there are more bursts, the burst rate becomes more or less stable at higher thresholds.

In order to define the burst rate in a consistent way for the complete period of data taking, we decided to use a 15σ threshold.
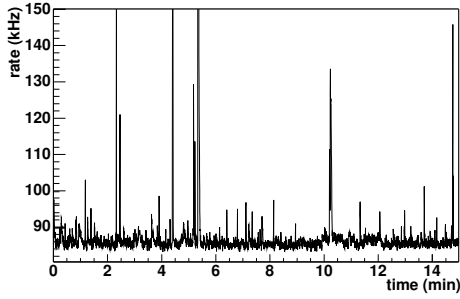
(a) Few bursts: count rate profile.
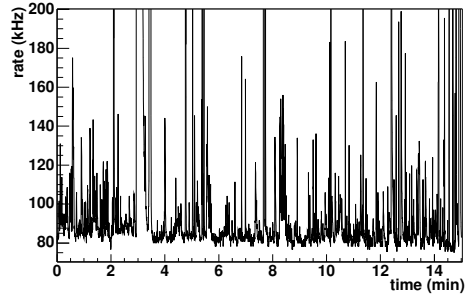
(d) Frequent bursts: count rate profile.
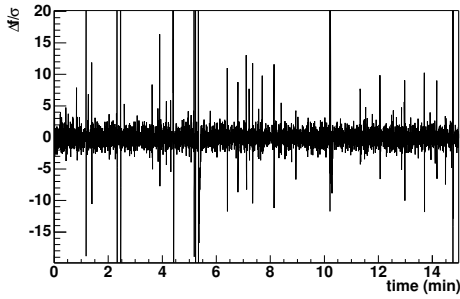
(b) Few bursts: derivative of count rate profile.
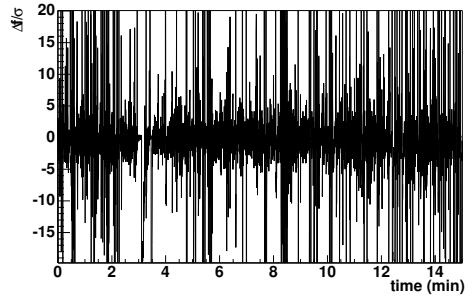
(e) Frequent bursts: derivative of count rate profile.
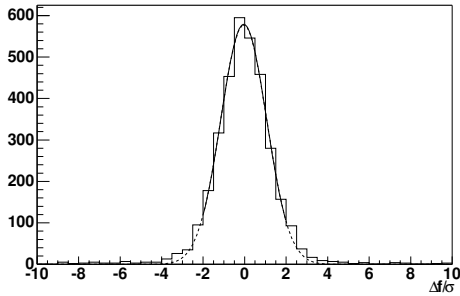
(c) Few bursts: distribution of derivatives.
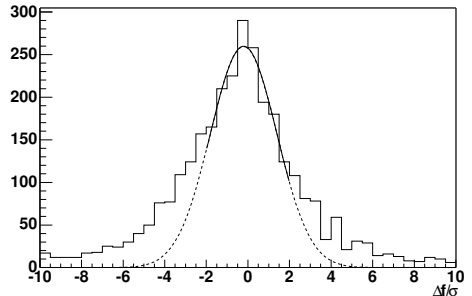
(f) Frequent bursts: distribution of derivatives.

Figure 3.7: *Determination of burst rate. For two periods, the count rate profile and its derivate are shown. The derivative is scaled to the value of σ, as calculated from the previous value of f according to Eq. 3.10. The distributions of $\Delta f/\sigma$ are shown along with a Gaussian fit. The solid line indicates the fit range, the dashed line indicates the extrapolation of the fitted function.*

(a) Two overlapping bursts: count rate.

(c) Fluctuations: count rate.

(b) Two overlapping bursts: derivative.

(d) Fluctuations: derivative.
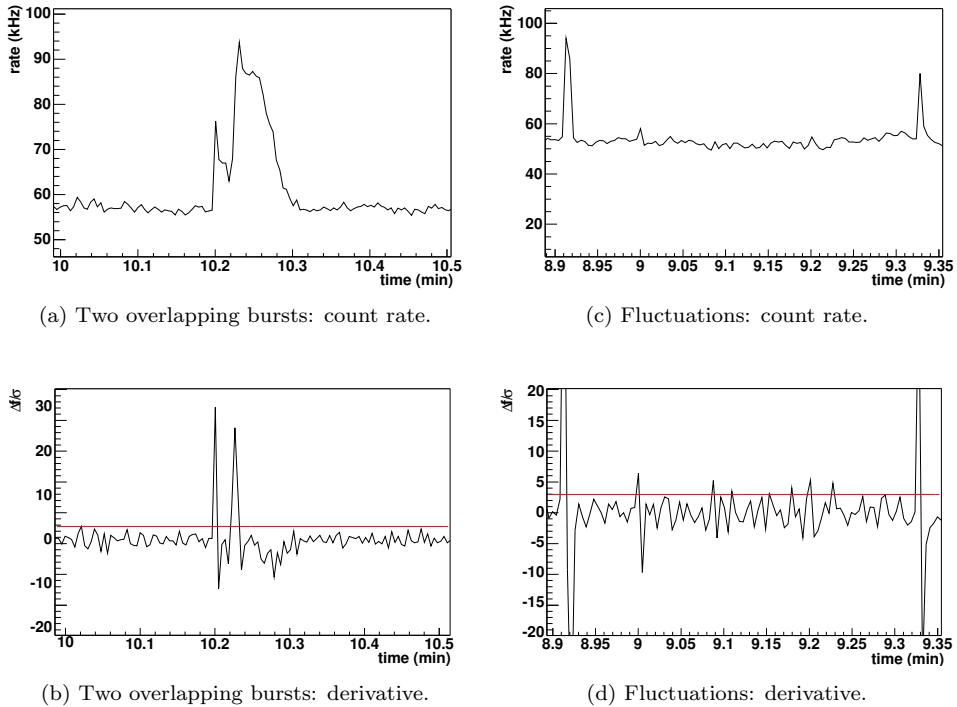
Figure 3.8: *Recognising bursts. A 3σ threshold gives too many bursts in the case of strong fluctuations in f. The real bursts are easily distinguished with a 10σ or 15σ cut as well. Overlapping bursts can be identified.*

3.5   Calibration

We will now compare the count rates measured by the different PMTs in the sector line.

In Fig. 3.10, the count rates in a five minute period are shown for each of the LCMs. One thing that stands out is that some of the stronger bursts are visible in more than one of the PMTs in an LCM. This can be understood as bioluminescence occurring at some distance from the LCM, where the light reaches two or even three of the PMTs.

Another striking feature is that the general aspect is the same for all of the PMTs, but their base rates are structurally different. If we want to compare the count rates in the different PMTs, we have to calibrate them with respect to each other.

On average, one would expect the base rates in different PMTs over the same 15-minute period to be equal. The amount of ^{40}K is constant over the volume of water occupied by the line, as is the amount of continuous bioluminescence. Of

(a) Few bursts

(b) Frequent bursts

(c) Many overlapping bursts

(d) High rate, few bursts
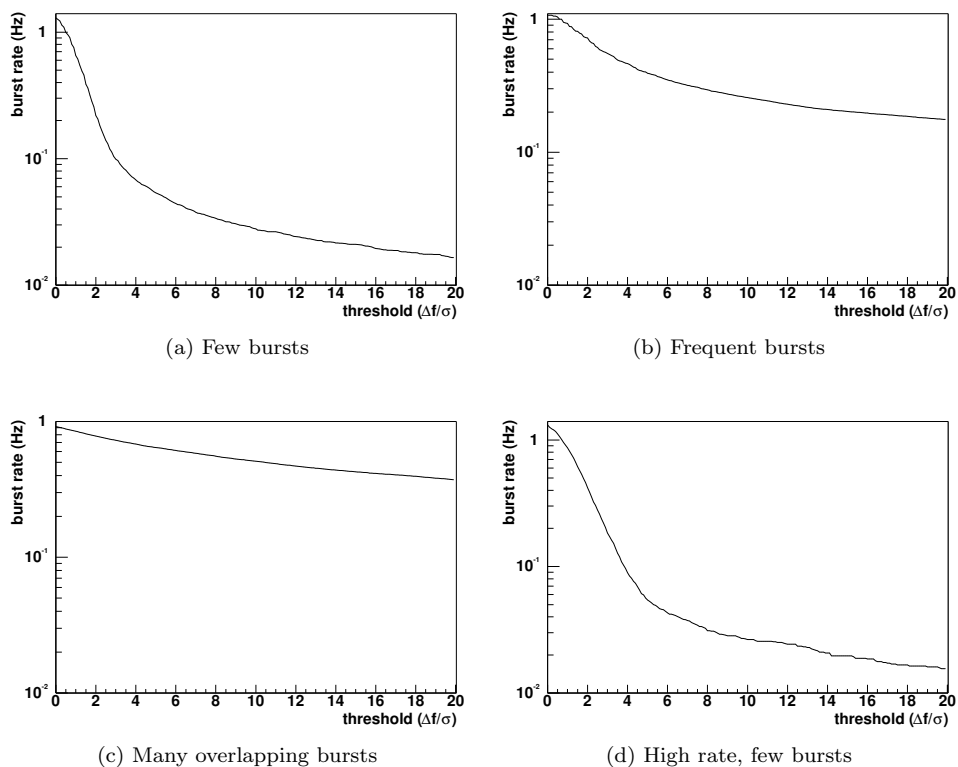
Figure 3.9: *Effect of the threshold choice on the burst rate.*

course, one PMT can occasionally happen to be very noisy when other PMTs are far quieter, but taken over the whole period of data taking, the base rates should be strongly correlated.

We use this correlation to calibrate the PMTs. Note that instantaneous count rates are calibrated using correlations between base rates, which are determined per 15 minute interval.

We choose one PMT, PMT 1 of LCM 1, as our reference, and plot all base rates observed in each of the other PMTs, $\overline{f}_i$, versus the base rate $\overline{f}_0$ observed in PMT 1 of LCM 1 at the same moment. The results for PMT 1 of LCM 5 are shown in Fig. 3.11a as an example. A more or less linear correlation can be distinguished. In addition, there are periods when one PMT registers a very high base rate and the other does not.

We ignore the points that are too far away from the diagonal, and restrict ourselves to relatively low values of the base rate ($\overline{f} \leq 140$ kHz), since these values correspond to a regime where the bursts are not too influential. We make a profile of $\overline{f}_i$ versus $\overline{f}_0$ (see Fig. 3.11b). We then fit a straight line through the
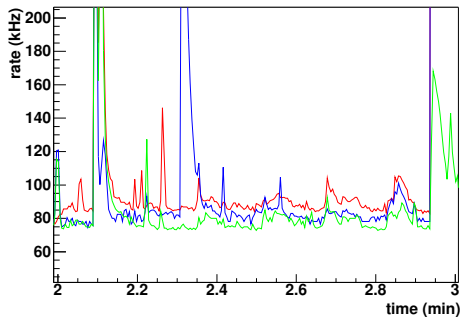
(a) LCM 1
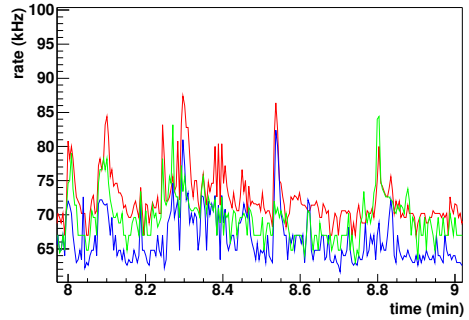
(b) LCM 4
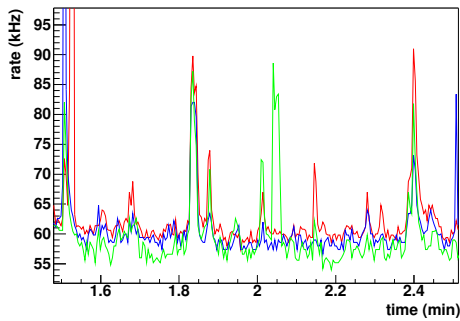
(c) LCM 5

Figure 3.10: *Count rates in LCMs 1, 4 and 5. For each LCM, the count rates in the three PMTs are shown separately.*
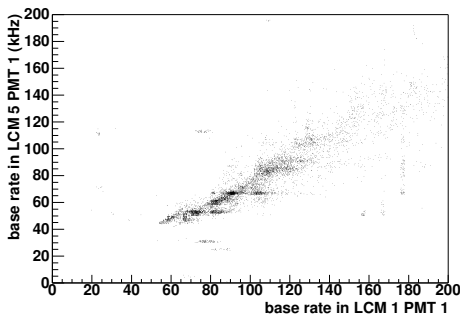
(a) Base rate in PMT 1 of LCM 5 versus base rate in PMT 1 of LCM 1.
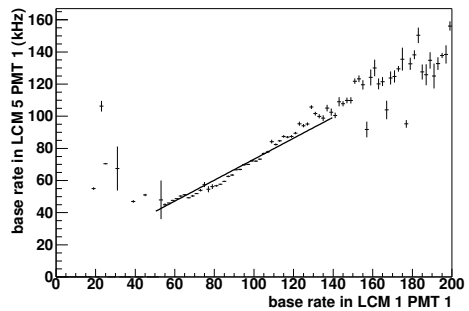
(b) Linear fit to the profile.

Figure 3.11: *Calibration of PMT 1 of LCM 5.*

LCM	PMT	a	b (kHz)
1	1	1	0
1	2	0.96	-0.79
1	3	0.93	-2.3
4	1	0.90	-1.5
4	2	0.78	0.58
4	3	0.86	0.43
5	1	0.65	8.06
5	2	0.67	6.05
5	3	0.71	-0.044

Table 3.1: *Calibration parameters.*

profile to determine the offset and the slope:

$$\overline{f}_i = a_i \overline{f}_0 + b_i. \tag{3.11}$$

The resulting parameters a_i and b_i for all PMTs are listed in Table 3.5.

A striking feature of these results is that the slope seems to be lower for LCMs higher up along the string. No explanation for this trend has been found.

We will use these parameters, obtained from the comparison of base rates, to calibrate the instantaneous count rates in each of the PMTs. If a count rate f_i^{raw} is seen in PMT i, we determine the calibrated count rate f_i^{cal} as:

$$f_i^{\mathrm{cal}} = \frac{f_i^{\mathrm{raw}} - b_i}{a_i}. \tag{3.12}$$

The effect of the calibration is shown in Fig. 3.12. The calibrated count rates agree quite well.

In the remainder of this chapter, only the calibrated data are used. Also, we recalculated the base rates and burst rates based on the calibrated data.

(a) Before calibration.

(b) After calibration.
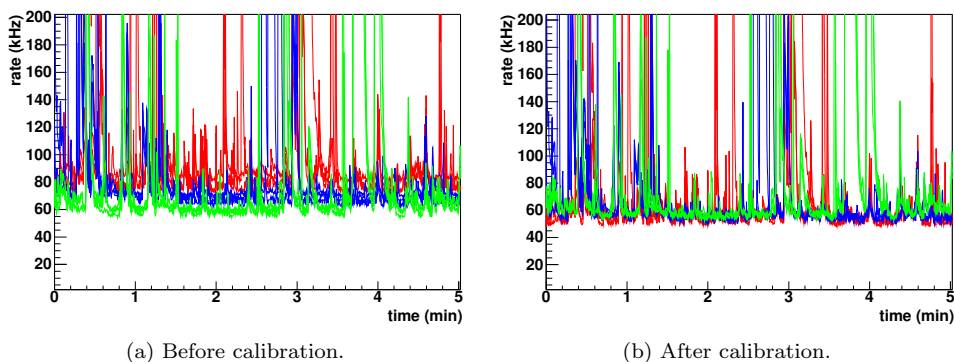
Figure 3.12: *The effect of calibrating the count rates. Data from all PMTs during a five minute period are shown before and after calibration.*

3.6 Base rate and burst rate over time

The time profiles of the base rate and the burst rate in one PMT, over the entire period of data taking, are shown in Fig. 3.13.
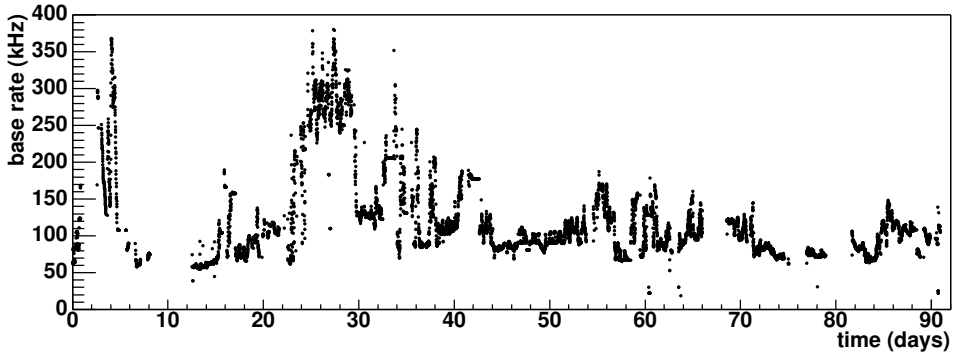
(a) Base rate.
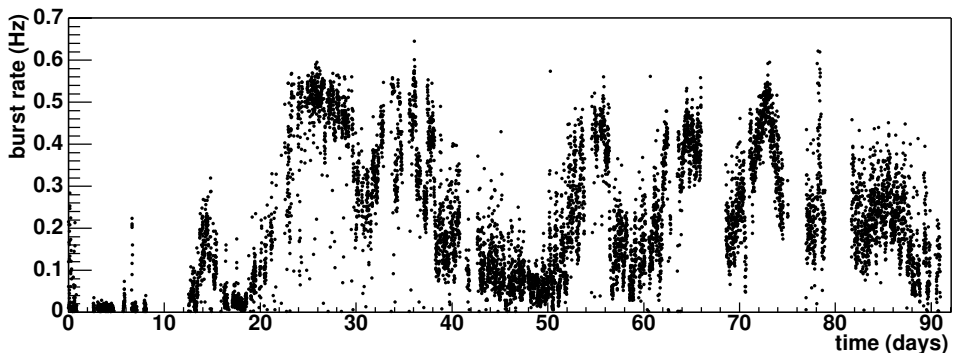
(b) Burst rate.

Figure 3.13: *Base rate and burst rate in PMT 1 of LCM 1. The behaviour in other PMTs is similar. Days are counted from 31 March, 0.00 am.*

Comparing these profiles, one can see that there is a clear correlation between the base rate and the burst rate. This correlation is shown more explicitly in Fig. 3.14, where the base rate is plotted against the burst rate.

During periods with a higher burst rate, the base rate tends to be higher. This can easily be understood: if there are many bursts, the observed count rate is higher for a significant fraction of time. In fact, the definition of the base rate as given in Section 3.4 hardly makes sense in the regime when there is always at least one burst taking place. In this case, the count rate never gets the chance to reach the 'true' base rate, since a new burst will begin before the previous one has finished.
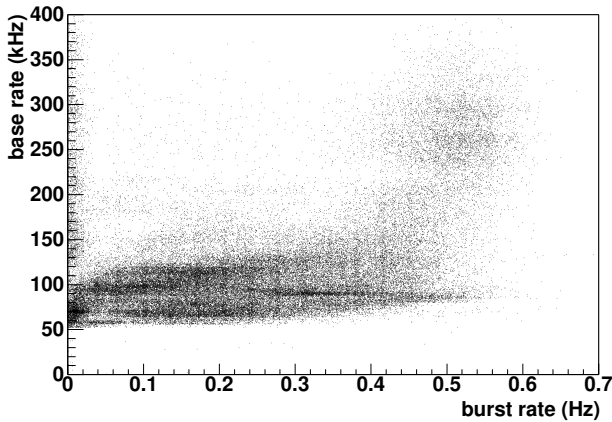
Figure 3.14: *Base rate versus burst rate.*

In addition, there are periods with a low burst rate that nevertheless show a high base rate. These are periods like the one shown in Fig. 3.4d.

3.7 Effect of water current

On 25 June, 2003, a frame equipped with various instruments was deployed at 42° 47.944' N and 06° 0.461' E, about 1 km from the ANTARES site. This frame, called 'test1.17', carried a 10" photomultiplier to measure the optical background and a velocimeter to measure the water current. The measured data were stored in the frame's memory, and read out when the frame was recovered on 10 July. Data on the water current were taken continuously during these 15 days, but unfortunately, the photomultiplier only took data during a 30-minute period.

Nevertheless, since 'test1.17' was located very close to the PSL, and the current velocity is not expected to vary significantly on this length scale, it makes sense to compare the current velocities measured by 'test1.17' with the count rates seen in the PSL.

Every 10 minutes, the current speed and heading were measured, averaging over 12 seconds of sampling. Current speed could only be measured above a threshold of 2.0 cm/s, with an accuracy of 1.0 cm/s. Current heading was measured with an accuracy of a few degrees, depending on the current speed.

In Fig. 3.15, the current speed is shown as a function of time for the entire period of data taking with 'test1.17'.

3.7.1 Correlation between water current and base and burst rates

In Fig. 3.16, the observed base and burst rates in the PSL are shown versus the speed of the water current. It is clear that at times when the current was stronger, both base rate and burst rate tend to be higher. This can be seen in
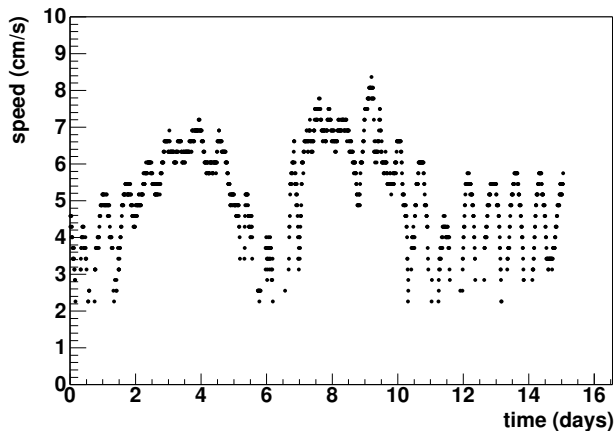
Figure 3.15: *Current speed as measured during the 15 days of data taking with 'test1.17'. Days are counted from 25 June, 6.00 am.*

more detail in Figs. 3.17 and 3.18, which show the distributions of base and burst rates, respectively, at different values of the current speed of the water.

The effect is clearest for the burst rates. The entire burst rate distribution shifts to higher values with stronger current. For the base rates, the situation is a bit more complicated. Part of the base rate distribution shifts to higher values as the current speed increases, but there is also a strong component that remains at about 60–80 kHz.

An explanation for the observed behaviour might be the following. At any given moment, bioluminescent organisms may or may not be present. When they are, their luminescent activity increases the base rate, and this effect is stronger at higher current speeds. In the absence of bioluminescence, the steady ^{40}K rate is observed.

In Fig. 3.19, the mean base and burst rate, as determined from Figs. 3.17 and 3.18, is shown as a function of the current speed. The errors shown are the widths
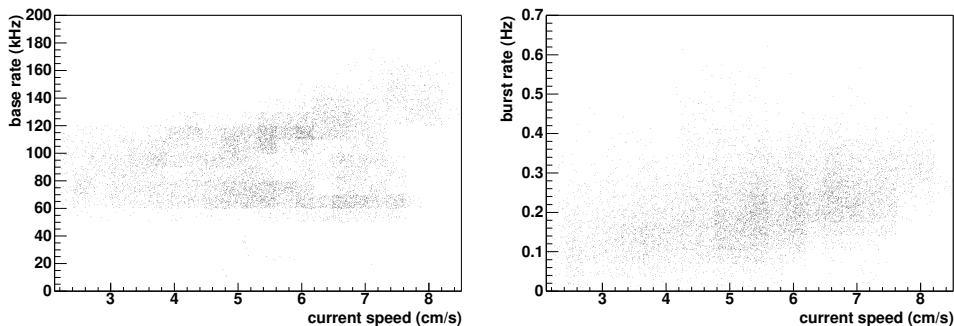
Figure 3.16: *Base rate (left) and burst rate (right) versus current speed.*
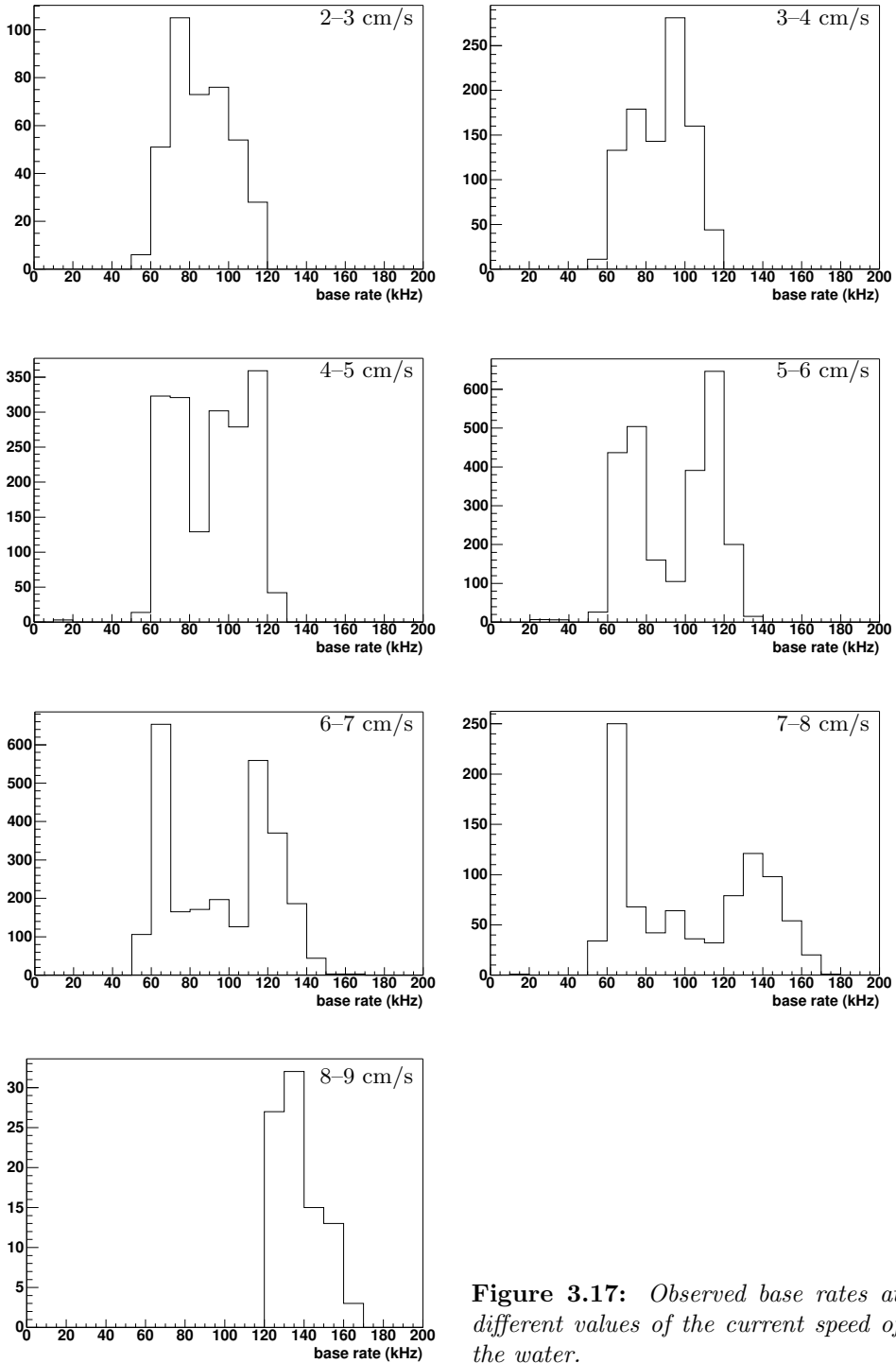
Figure 3.17: *Observed base rates at different values of the current speed of the water.*
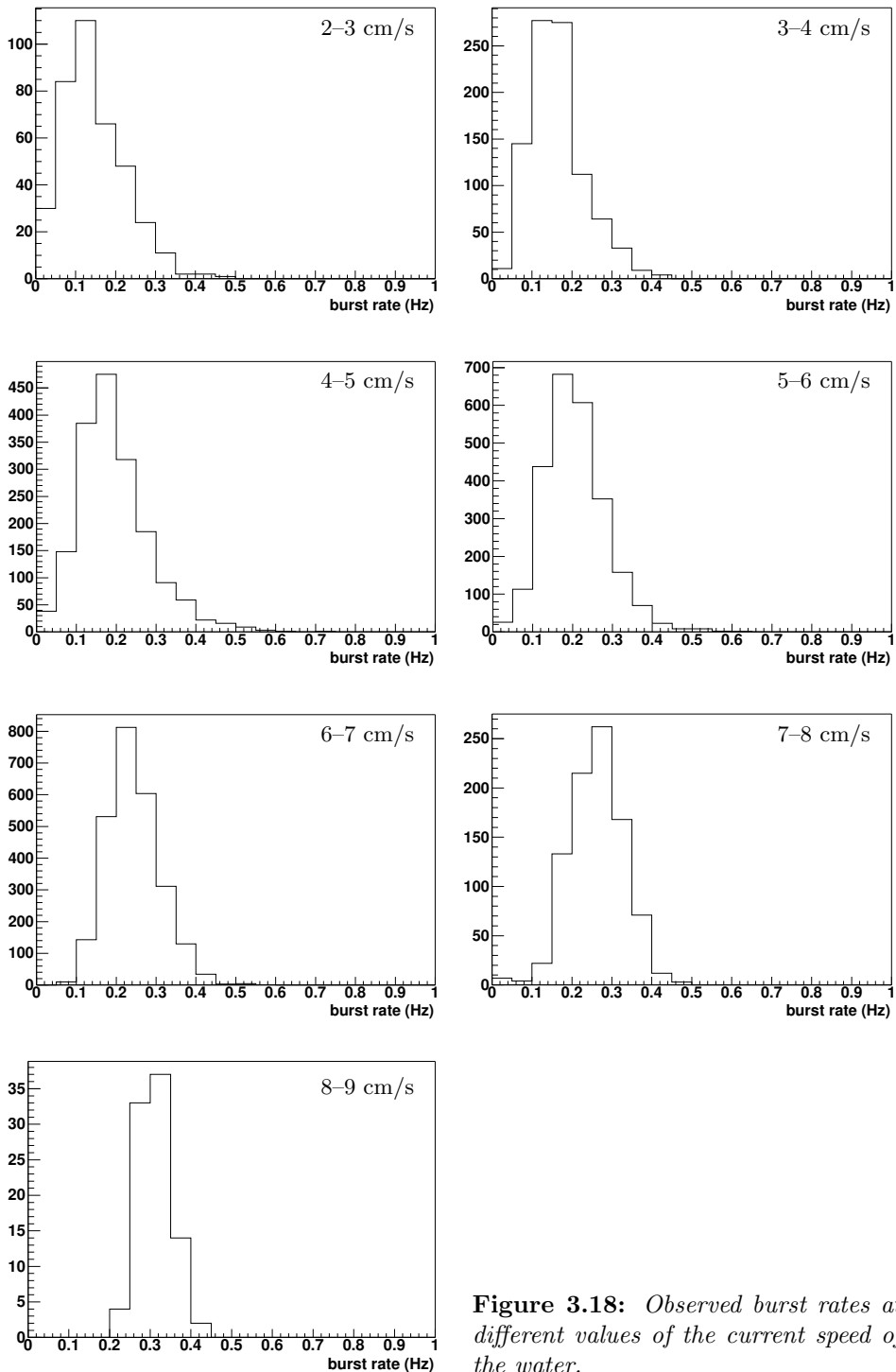
Figure 3.18: *Observed burst rates at different values of the current speed of the water.*
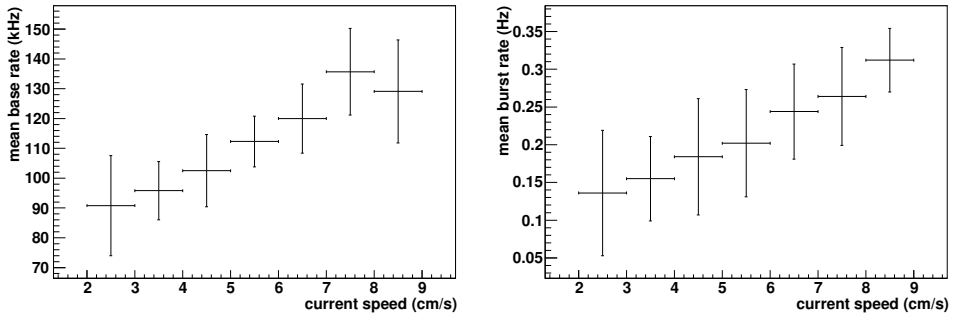
Figure 3.19: *Mean base rate (left) and mean burst rate (right) versus current speed.*

of the distributions of base rate c.q. burst rate in each current speed interval. Although these errors are fairly large, a correlation between mean base rate c.q. burst rate with the current speed is visible.

3.7.2 Periodicity

Another interesting feature of the observed count rates and the current speed as measured by 'test1.17' becomes clear when we study the behaviour in time. Especially during the period from 5 to 9 July, an oscillatory behaviour can be seen in the current speed, as is shown in Fig. 3.20.

In Fig. 3.21a, a fast Fourier transform of the measurements of the current speed is shown. A clear peak is visible at a period of around 17–18 hours. The oscillations are due to the limited amount of available data, as can be seen from Fig. 3.21b, which shows the same fast Fourier transform where a random value for
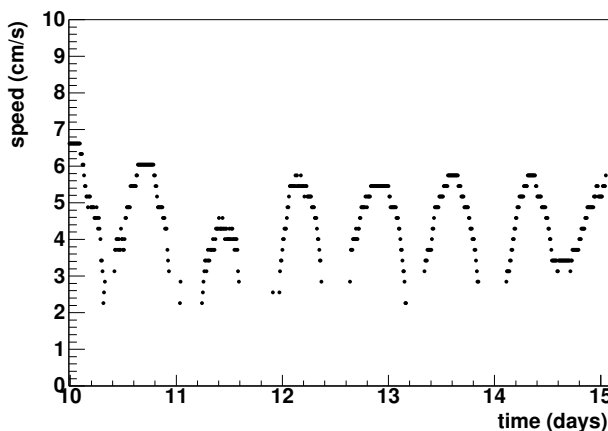
Figure 3.20: *Current speed versus time, during the last five days of data taking with 'test1.17', when an oscillatory behaviour was observed.*

(a) Observed current speed

(b) Random current speed
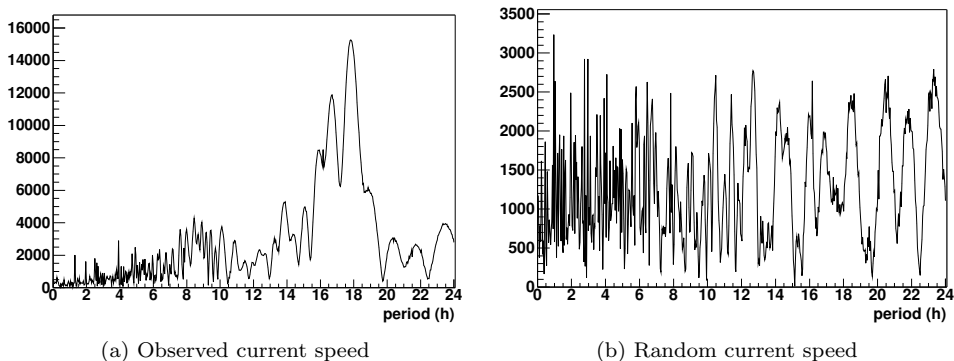
Figure 3.21: *Fast Fourier transform of the current speed, for the true speed as well as for a random speed. The oscillations at longer periods are a result of the finite time of data taking, combined with the resolution of the fast Fourier algorithm.*

the current speed is chosen at each moment.

Because of these oscillations, the exact location of the peak cannot be determined. However, a period of 17–18 hours corresponds quite well to the period of inertial waves at the location of the ANTARES detector. Inertial waves are caused by the Coriolis force acting on moving water particles, due to the rotation of the Earth [36]. The Earth rotates with a frequency $\Omega = \frac{2\pi}{24\,\text{h}}$. At latitude λ, the component of the rotation vector around the local vertical is $\Omega' = \Omega \sin \lambda$. A water particle moving in a horizontal plane experiences a Coriolis force $F_{\text{C}} = 2mv\Omega'$, perpendicular to its velocity $\vec{v}$. It will move in a circle, with the Coriolis force providing the centripetal acceleration:

$$\frac{v^2}{r} = \frac{F_{\text{C}}}{m} = 2v\Omega \sin \lambda. \tag{3.13}$$

Substituting $v = \omega r$, we find

$$\omega = 2\Omega \sin \lambda. \tag{3.14}$$

In other words, the circular motion has a period

$$T = \frac{12\,\text{h}}{\sin \lambda}. \tag{3.15}$$

At the latitude of the ANTARES detector, this amounts to $T = 17.7$ h.

Since the base rate and the burst rate are correlated with the current speed, a periodic behaviour is expected for these quantities too.

A fast Fourier transform of the base rate is shown in Fig. 3.22. A peak may be present around the expected 17.7 hours, but the base rate seems to exhibit a stronger oscillation with a period similar to that of tidal variations (12.4 hours).
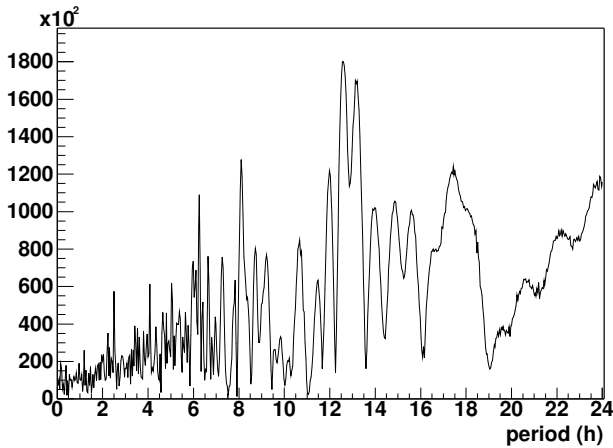
Figure 3.22: *Fast Fourier transform of the observed base rate during the period of simultaneous data taking with the PSL and 'test1.17'.*

Again, because of the oscillations due to the finite time of data taking, the exact location of the peak cannot be determined. It does seem compatible with a period of 12.4 hours.

In order to understand why the base rate would vary with the same periodicity as the tide, we would have to know how luminescent organisms respond to pressure and pressure variations. Unfortunately, not much is known on this topic.

Only luminescent dinoflagellates have been studied in considerable detail. Dinoflagellates are a large group of protists, most of which are marine plankton that live in undeep waters. They can be cultivated quite easily, and cultures are commercially available. Most laboratory experiments investigating bioluminescence are done with dinoflagellates. In the following discussion, we will use properties of dinoflagellates, bearing in mind that luminescent organisms that live at the depth of the ANTARES detector may (and probably do) have different properties.

Dinoflagellates are not sensitive to static pressure: the threshold for luminescent response is of the order of 10^6 N m^{-2}. Neither are they sensitive to varying pressure, with a threshold of about 10^5 N m^{-2} s^{-1}. This is orders of magnitude larger than the level of ambient noise in the sea. The sensitivity to shear stress is much larger: at about 0.1 N m^{-2} dinoflagellates start to luminesce. Thus, tidal variations in sea level, or steady, laminar currents cannot explain the periodic increase in base rate. Turbulent flow is needed in order for dinoflagellates to give a luminescent response [37].

Assuming that the base rate is mainly determined by the steady background bioluminescence emitted by bacteria and other microscopic organisms, this means that an increase in base rate corresponds to an increase in turbulent flow. It is possible that the breaking of internal tidal waves gives rise to turbulence, and that the periodicity of the internal waves is reflected by the periodicity of the bioluminescent base rate.

Of course, this argument relies on the behaviour of dinoflagellates, and it is not known whether other organisms have comparable sensitivities to pressure and
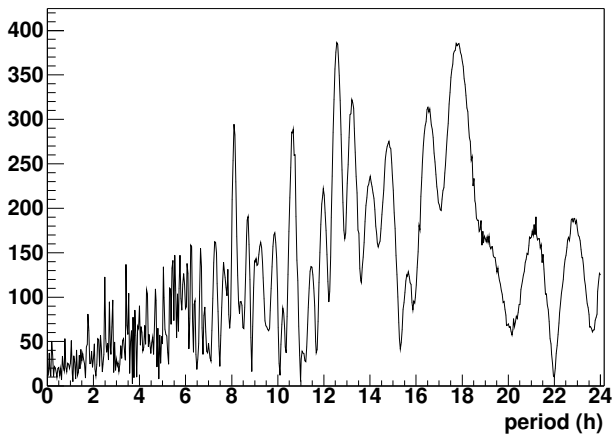
Figure 3.23: *Fast Fourier transform of the observed burst rate during the period of simultaneous data taking with the PSL and 'test1.17'.*

shear stress.

An alternative explanation could be that the bacteria responsible for the variations in base rate are sensitive to the presence of nutrients, which would be transported from the coastal regions to deep water with a tidal periodicity.

Whereas a periodicity of 12.4 hours can be observed in the base rate, it is more problematic to see a clear periodicity in the spectrum for burst rates. A fast Fourier transform of the burst rate is shown in Fig. 3.23. A peak may be present around 17.7 hours, as well as a less prominent one around 12.4 hours, but they are not at all very clear.

It might well be that macroscopic organisms, which are responsible for the bursts in the count rate, are more sensitive to the current speed, because they flash when colliding with the detector. Bacteria that contribute to the steady bioluminescent background may be more sensitive to turbulence or to the presence of nutrients. This could explain the stronger periodicity in the base rate at 12.4 hours as well as the stronger periodicity in the burst rate at 17.7 hours.

For a better understanding of the relationship between water current and bioluminescence, more data are needed, with the current speed being monitored over a longer period of time.

3.8 Simulation of bioluminescence

The question arises if the characteristics of the observed count rates can be explained in a simple way. Let us assume that the observed light is caused by ^{40}K and by bioluminescence, and that luminescent organisms emit light only when they collide with the mechanical structure of the detector. In view of the discussion in Section 3.2, this is a reasonable approximation. Based on these assumptions, we simulated the optical background in the PSL.

The simulation of bioluminescence is based on the following model.

3.8.1 Collisions

There is a fixed number n_{org} of luminescent organisms per volume unit of water.

There are organisms of different sizes: a 'larger size' merely means that the organism emits more light. The size x is distributed according to a power law:

$$\frac{\mathrm{d}n_{\mathrm{org}}}{\mathrm{d}x} \propto x^{-\gamma}, \tag{3.16}$$

where the minimum and maximum size and the exponent γ can be adjusted. The choice for a power law distribution is motivated by the fact that distributions of species size often follow such a law [38].

Due to the water current and their own movements, these organisms collide with the detector's mechanical structure. The collision rate F is proportional to n_{org}, to the area A of the structure, and to the mean relative velocity v:

$$F = n_{\mathrm{org}} v A, \tag{3.17}$$

where v depends on the water current speed v_w and the proper movement v_p of the organism:

$$v = \sqrt{v_w^2 + v_p^2}. \tag{3.18}$$

At higher current speeds, the flow becomes more and more turbulent, giving a stronger stimulus for the luminescent organisms. To account for this, we take A to represent an effective area rather than the geometric area A_g, to which it is related by

$$A = (1 + a v_w) A_g, \tag{3.19}$$

where a is some constant indicating the strength of the effect of turbulence.

3.8.2 Light emission and propagation

In response to a collision, a luminescent organism emits light with a fixed intensity profile as a function of time: a linear rise followed by exponential decay. The rise and decay times depend on the size of the organism, according to a power law. The exponent in this power law can be adjusted. The light is emitted isotropically over a solid angle of 4π.

For each OM, the intensity seen from this particular flash is calculated. There are two possibilities: either the organism collided with the OM itself, and the flash takes place on the surface of the sphere, or the organism collided with another part of the detector, and the flash takes place at a larger distance.

Collision on other detector part

In the case of a collision on another part, the observed intensity at time t, $F_o(t)$, is given by:

$$F_o(t) = \epsilon \, \frac{A \cos \alpha}{4\pi r^2} \, e^{-r/\lambda} \, F_e(t), \tag{3.20}$$

where ϵ is the PMT's quantum efficiency, A is its sensitive area, α is the direction of the flash with respect to the PMT's line of view, r is the distance between the location of the flash and the PMT, λ is the attenuation length of light in the seawater, and $F_e(t)$ is the intensity of the light emitted by the organism at time t.

Collision on the sphere itself

If the flash takes place on the sphere itself, F_o is given by:

$$F_o(t) = \epsilon \, f(\alpha) \, F_e(t), \tag{3.21}$$

where $f(\alpha)$ is the fraction of emitted light that reaches the sensitive photocathode area. It is calculated as the solid angle Ω_{PMT} subtended by the photocathode, as seen from the position of the collision, divided by 4π. The value of Ω_{PMT} depends on the radii of the sphere and the PMT, and on the PMT's opening angle, as shown in Fig. 3.24. From this picture, an expression for Ω_{PMT}, and hence $f(\alpha)$, as a function of α can be derived. Internal reflection on the glass-water boundary is neglected. The fraction of emitted light seen by the PMT is shown as a function of α in Fig. 3.25.
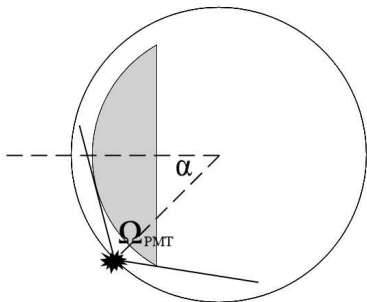
Figure 3.24: *Collision on the sphere. Ω_{PMT} is the solid angle subtended by the PMT, as seen from the location of the collision. The solid lines indicate the light rays that just touch the edge of the PMT, or follow a tangent to the surface of the PMT. α is the angle between the two dashed lines, which indicate the PMT's line of view and the direction in which it sees the collision.*

For each OM, the contributions from all flashes are added to give the observed count rate at each moment.

3.8.3 Steady background

On top of the light from these bioluminescent bursts, the light from ^{40}K decay is seen in the PMT. It contributes a steady 60 kHz to the count rate.

In addition, there is a steady, non-pulsed bioluminescent contribution, caused by bacteria or other microscopic organisms. Its intensity may vary from time to time, independent of the luminescence from larger organisms.

To summarise, we have the following sources of background:

- ^{40}K decay: a steady rate of 60 kHz;
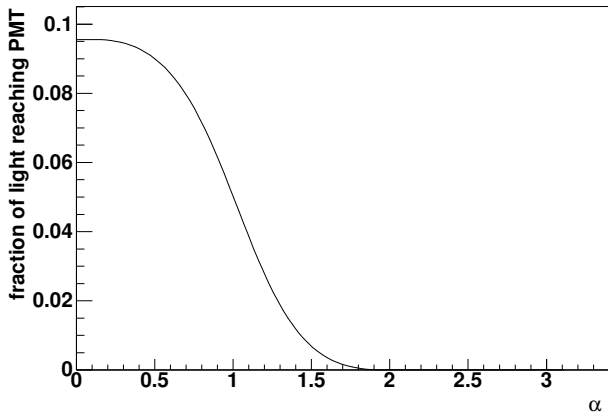
Figure 3.25: *Fraction of light reaching the photocathode as a function of the angle α.*

- luminescent organisms that emit flashes of light in response to collisions with the detector;

- a steady bioluminescent contribution f_s, independent of water current.

3.8.4 Limitations of the model

The simple model presented here has its limitations. It is rather naïve in its assumptions on the way luminescent organisms respond to flow. Some approximations have been made:

- In the model, organisms emit light only when physically colliding with the detector structure. In reality, there is turbulent flow around the cables, frames and spheres, which will induce luminescence also at some distance from the surface of the detector itself.

- Luminescent organisms are assumed to be homogeneously distributed in the water, but in reality they might cluster together. Whether this is the case, and if so, what the length scale of such clusters would be, is unknown. The homogeneous distribution is the best approximation we can make.

- The model allows for some variation in the size of organisms, assuming that the number density decreases with size according to a power law. Yet all organisms are treated similarly in their response to collisions, the only difference being the intensity of light they emit.

- The model only takes into account bioluminescence in response to mechanical stimulation in the form of collisions. Communication, searching for prey, and other behaviour is ignored.

- Some organisms can eject blobs of luminescent matter, which might stick to the detector. This possibility is left out of the model.

Despite these obvious shortcomings, we will see that the model seems to be reasonably able to reproduce the patterns observed with the PSL. Some of the more complicated features seen with the PSL are not in the simulated bioluminescence data, but overall there is a fair agreement.

The increase in bioluminescence with the speed of the water current, as predicted by this model, corresponds well with the measurements of the PSL during the short period in which the PSL and 'test1.17' took data simultaneously.

3.8.5 Reproducing the time profiles

Simulations were performed using various values for the input parameters, such as the concentration of luminescent organisms, the intensity and duration of the individual flashes, etc. Time profiles for different settings are shown in Fig. 3.26.

By varying the parameters of the model, it is possible to reproduce the time profiles measured with the PSL. The burst rate depends strongly on the speed of the water current. A stronger current causes more peaks. The quiet and noisy regimes discussed in Section 3.4 can be reproduced by varying the current. The steady bioluminescence background is needed to reproduce the quiet periods with a high base rate. This regime could perhaps also be reproduced by tuning the settings such that many tiny bursts overlap in such a way that the individual bursts are completely undistinguishable, and a steady rate results. However, in order to do that, the number of photons emitted by each organism would have to be smaller by several orders of magnitude than the values given by biologists (cf. Section 3.2).

3.9 Effect on detector performance

The bioluminescent component of the optical background in the ANTARES detector is larger than had been expected. The design of the detector and the DAQ system was optimised for count rates of 60–80 kHz. Higher count rates make readout, triggering and track reconstruction more difficult or even, in the case of very high count rates, impossible. For instance, the CPU time needed for the triggering algorithm is proportional to the tenth power of the count rate [39].

It turned out that the trigger system was able to handle quite high count rates, up to about 600 kHz. In this respect, the large bioluminescent background has been very useful, since it gives a good indication of what count rates are still acceptable. However, higher count rates also imply more frequent local coincidences, and more fake L1 hits (see Section 2.4): the local coincidence rate increases quadratically with the singles rate. This makes it more difficult to detect cosmic neutrinos amidst the optical background. For a larger underwater neutrino telescope, such as KM3NET, it is therefore desirable to search for a location with less bioluminescent activity.

ANTARES is located at 2.5 km depth, but it is quite close to the coast and to the mouth of the river Rhône. Other locations, farther away from the shore, or at

(a) n=10 m^{-3}, v_w=0.01 m/s, f_s=0 kHz.

(b) n=100 m^{-3}, v_w=0.01 m/s, f_s=0 kHz.

(c) n=10 m^{-3}, v_w=0.05 m/s, f_s=0 kHz.

(d) n=10 m^{-3}, v_w=0.01 m/s, f_s=150 kHz.
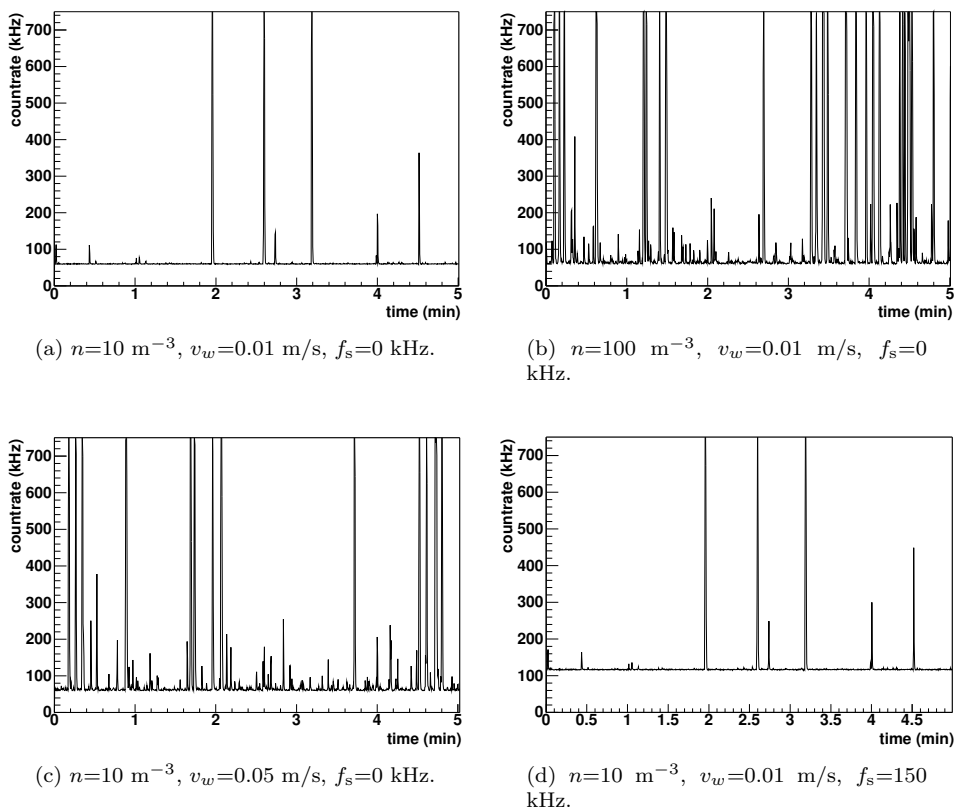
Figure 3.26: *Time profiles simulated with various settings. In all of these profiles, organisms of all sizes were simulated.*

a larger depth, may suffer less from bioluminescence. Data on concentrations of luminescent organisms at different depths are scarce, but bioluminescent activity seems to decrease with depth [40]. For instance, a site in the Ionian Sea has been studied by the NEMO collaboration [41]. Below a depth of 2500 m, there is a negligible concentration of luminescent organisms; the sea is 3500 m deep at this location. It is recommended that at any site under consideration for a large volume underwater neutrino telescope, bioluminescent activity be investigated with great care.

Meanwhile, ANTARES has to deal with the bioluminescent background being as high as it is, if physics results are to be obtained. One strategy is to keep note of the background base rate during data taking, and to take this rate into account when triggering and during physics analysis. If one wishes to eliminate bursts, one can use the instantaneous count rate instead of the base rate. This is a bit more CPU-intensive, however. Since the count rate is higher than the base rate for only

(a) Count rates   (b) Base rates
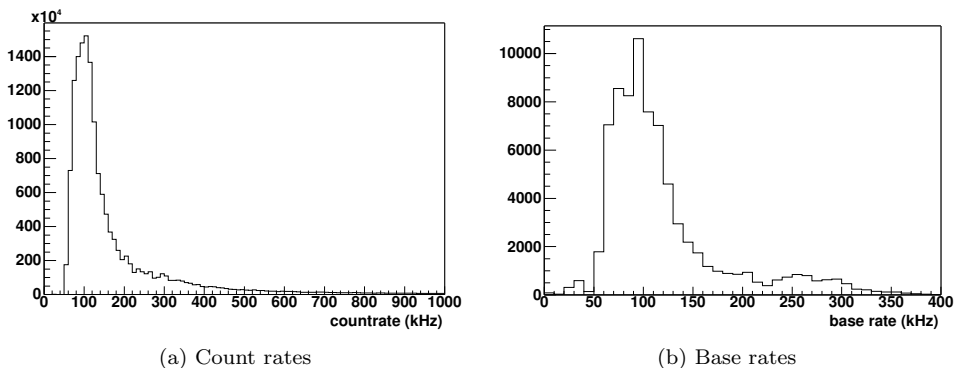
Figure 3.27: *Distribution of count rate and base rate, during the 90 days of data taking with the PSL.*

5% of the time, using the base rate as an approximation for the count rate will suffice. In Fig. 3.27, the distribution of count rate and base rate is shown.

The exact effect of a higher count rate on the performance of trigger and reconstruction software remains to be studied. If the trigger efficiency as well as the efficiency and accuracy of the reconstruction are acceptable for count rates below 400 kHz, the bioluminescent background will not hinder the analysis of the data taken with ANTARES.

If, on the other hand, the trigger purity or the reconstruction accuracy is unacceptably low at high count rates, it will be necessary to discard all data from a PMT as soon as it records a count rate higher than a certain value. If this value is chosen so high that it can only be reached during a burst, one can even discard all data from the entire LCM, since a burst seen in one PMT is often also seen in the other PMTs in the storey.

In Fig. 3.28, we show, as an example, the fraction of time during which a given number of PMTs observes a count rate higher than 200 kHz, as well as the fraction of time during which a given number of LCMs observes a count rate higher than 200 kHz in at least one of its PMTs. Since there were only three working LCMs on the PSL, we will discuss only the results for individual PMTs.

Each individual PMT measures a count rate higher than 200 kHz for about 20% of the time (see Fig. 3.27a). However, since the count rate is, on average, comparable for all PMTs in the detector, and variations in base rate are global, the probability of all PMTs observing a count rate higher than 200 kHz is much larger than it would be if the count rate variations in individual PMTs were uncorrelated.

During 8.6% of the time, the count rate exceeds the 200 kHz threshold in all PMTs on the string. During 15% of the time, a count rate higher than 200 kHz is seen in at least six out of nine PMTs. The count rate is higher than the threshold in three or more PMTs during 31% of the time. If at least one third of the PMTs

(a) PMTs with count rate above 200 kHz.

(b) LCMs with count rate above 200 kHz.
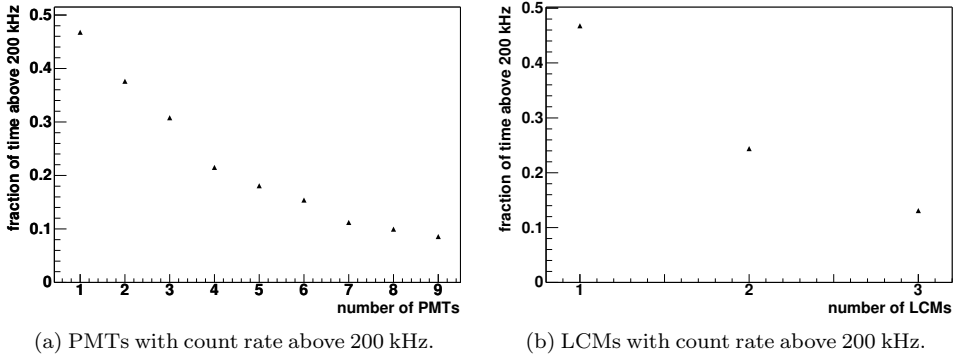
Figure 3.28: *Fraction of time during which at least a given number of PMTs (left) or LCMs (right) observes a count rate higher than 200 kHz.*

is required for a meaningful analysis, a threshold of 200 kHz therefore implies an overall dead time of 15%. The dead time is 31% if at least two thirds of the PMTs must measure a count rate below 200 kHz.

The same percentages can be determined for other values of the count rate threshold. In Fig. 3.29, we show the fraction of time that three, six or nine out of nine PMTs measure a count rate above the threshold, for different threshold values.

It is not clear how these results will extrapolate to the complete ANTARES detector, let alone a km^3-scale detector. Based on the results presented in this chapter, we expect that the count rates will vary coherently even on these length scales. In that case, discarding data from PMTs observing high count rates will give dead times comparable to those presented here.
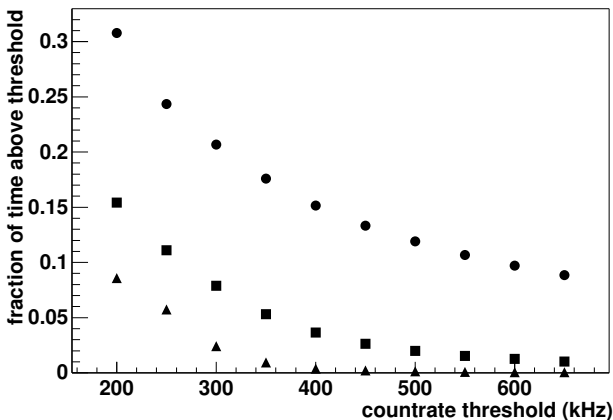
Figure 3.29: *Fraction of time during which a count rate higher than a given threshold is observed in at least 3 (discs), 6 (squares) or 9 (triangles) out of 9 PMTs.*

55

— Mais, demanda alors Ben-Zouf, à quoi servent tous ces calculs que ce savant hargneux vient d'exécuter comme des tours de passe-passe ?

— À rien ! répondit le capitaine Servadac, et c'est précisément ce qui en fait le charme !

Jules Verne, *Hector Servadac*, Vol. 2, Ch. VIII

4

VELOCITY FILTER

As discussed in Chapter 1, a cosmic neutrino can be detected when it undergoes a charged current interaction and produces a muon, which in turn emits Čerenkov radiation.

Several effects combine to make detection easier for high energy neutrinos than for low energy neutrinos. Yet a significant flux can be expected in the 1–100 GeV region, and it is worthwhile to attempt detection, if not reconstruction, of neutrinos in this energy range.

This chapter describes the velocity filter, a new method to search for neutrinos from a known source, by using the knowledge of the source's position at the sky. An analysis with this velocity filter of simulated data from Supernova Remnant RX J1713.7–3946 is presented. The results indicate that the method is sensitive to fluxes a few orders of magnitude larger than the fluxes expected from this source, under the assumption of an unbroken E^{-2} spectrum.

4.1   Motivation

4.1.1   Photon and neutrino fluxes

Many cosmic sources of high energy photons are known, and their properties have been studied in detail.

The photon spectra typically follow a power law:

$$\frac{\mathrm{d}\Phi}{\mathrm{d}E_\gamma} \propto E_\gamma^{-\alpha_\gamma},\qquad(4.1)$$

where the spectral index α_γ varies from 2.0 to as high as 2.7.

The mechanism of shock acceleration is generally thought to explain these spectra [42]. A naïve calculation yields $\alpha_\gamma = 2$, but more detailed studies show that somewhat higher values, 2.1–2.4, are more likely.

If the production of high energy photons in a shockwave is mainly due to hadronic processes, the production of neutrinos is an inevitable consequence.

Hadrons interact with each other or with ambient photons to create pions, which in turn decay into photons, leptons and neutrinos:

$$\pi^0 \quad \rightarrow \quad \gamma\gamma \tag{4.2}$$
$$\pi^+ \quad \rightarrow \quad \mu^+ \nu_\mu \rightarrow e^+ \nu_e \overline{\nu}_\mu \nu_\mu \tag{4.3}$$
$$\pi^- \quad \rightarrow \quad \mu^- \overline{\nu}_\mu \rightarrow e^- \overline{\nu}_e \nu_\mu \overline{\nu}_\mu \tag{4.4}$$

The neutrino spectrum is generally assumed to be similar to the photon spectrum.

One particular object that is considered a likely source of high energy neutrinos is RX J1713.7–3946, a Supernova Remnant in the southern hemisphere, near the Galactic Centre. For this object, the ν_μ flux has been predicted as [43]:

$$\frac{\mathrm{d}\Phi}{\mathrm{d}E_{\nu_\mu}} = 1.55 \cdot 10^{-4} \left(\frac{E_{\nu_\mu}}{\mathrm{GeV}} \right)^{-2.2} \mathrm{m}^{-2}\,\mathrm{s}^{-1}\,\mathrm{GeV}^{-1}. \tag{4.5}$$

We will use this predicted flux as an example, analysing it with the velocity filter.

4.1.2 Limitations of standard triggering and reconstruction at low energies

As discussed in Section 2.4, a minimum cluster size of five L1 hits is often required in the triggering algorithm. This means that at least ten photon hits are needed for an event to be triggered. Events with fewer hits are discarded.

The higher the energy of the muon, the more photons it produces. The number of Čerenkov photons emitted per unit track length and per unit wavelength is given by:

$$\frac{\mathrm{d}N}{\mathrm{d}\lambda\,\mathrm{d}x} = \frac{2\pi\alpha}{\lambda^2} \left(1 - \frac{1}{n^2 \beta^2} \right), \tag{4.6}$$

where α is the fine structure constant.

In the wavelength range from 300 to 600 nm, the blue to green light for which seawater is most transparent, about $3.5 \cdot 10^4$ photons are emitted per metre track length.

Higher energy muons typically have larger path lengths inside the detector, and therefore cause more Čerenkov light to be detected. In addition, above about 1 TeV, the muon starts losing significant energy through the process of bremsstrahlung. The photons produced in this process rapidly produce electromagnetic showers. The electrons and positrons in these showers in turn produce Čerenkov radiation, which can be detected.

A 10 GeV muon produces on average 2 hits in the detector[1]; a 200 GeV muon produces on average 8 hits. If the Čerenkov light of secondary particles is taken into account, these numbers are slightly higher: 3.5 and 10 hits, respectively. A 1 PeV muon illuminates more than 100 PMTs [44].

---

[1]The average is calculated over all muon tracks that produce at least one hit.

The fact that low energy neutrinos produce less light makes standard triggering and track reconstruction problematic at lower energies: the detector efficiency at 100 GeV is two orders of magnitude smaller than it is at 1 TeV.

Even if a much looser triggering algorithm is used, a minimum number of photon hits is needed in order to reconstruct the track. As there are five degrees of freedom in the reconstruction, the absolute minimum number of hits required to reconstruct the muon track unambiguously is five. With more hits, the track can be reconstructed with a higher accuracy, but with fewer hits, reconstruction is impossible.

4.1.3 Detecting low energy neutrinos from a given source

The lower efficiency at low energies is partly compensated by the power law behaviour of the neutrino energy spectrum. The differential flux for a neutrino energy spectrum with spectral index $\alpha_\nu \sim 2$ is much larger at lower energies than at higher energies. Because the cross section is proportional to the neutrino energy, the interaction probability varies linearly with E_ν. The muon range, and hence the effective volume, depends linearly on E_μ, and therefore roughly linearly on E_ν. As a result, the interaction rate per energy interval for a given flux is roughly constant.

For a specific neutrino source, the neutrino direction is known in advance, and therefore the muon direction is known as well, albeit approximately. This information can be used to improve the detection efficiency.

It may not be possible to detect each muon individually, let alone to reconstruct it, but an excess of muons travelling in a given direction can still be observable. This is the strategy on which the velocity filter is based.

4.2 Method

The velocity filter looks for pairs of hits in different OMs. The combinations of arrival times and positions show a different signature for background hits and signal hits. It is not possible to determine for each hit pair individually whether the hits are due to a cosmic neutrino, but after a sufficient amount of time, the presence of a neutrino flux from a given position may be detected.

4.2.1 Velocity between two hits

For a hit occurring at time t_i in OM i at position $\vec{x}_i$, and another hit occurring at time t_j in OM j at position $\vec{x}_j$, the distance vector $\vec{r}$ is given by

$$\vec{r} = \vec{x}_j - \vec{x}_i, \tag{4.7}$$

and the time difference τ is

$$\tau = t_j - t_i. \tag{4.8}$$

The longitudinal distance $r_\parallel$ between two hits is defined as the distance between the two hits projected on the muon track. It can be written in terms of the distance z_i that was introduced in Eq. 2.7:

$$r_\parallel = z_j - z_i. \tag{4.9}$$

The transverse distance $r_\perp$ is the distance between the projections of the two hits on a plane that is perpendicular to $\hat{n}$. It is given by

$$r_\perp{}^2 = r^2 - r_\parallel{}^2. \tag{4.10}$$

Note that, in general, $r_\perp \neq R_j - R_i$, with R_i as defined in Eq. 2.6 (see Fig. 4.1).
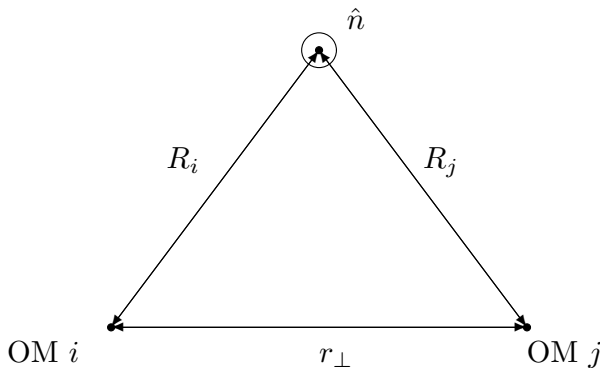
Figure 4.1: *Transverse distance $r_\perp$ between two hits. This is not the same as the difference between R_i and R_j.*

We define the *velocity vector* $\vec{v}$ between the two hits as:

$$\vec{v} = \frac{\vec{r}}{\tau}. \tag{4.11}$$

Similarly, the longitudinal and transverse velocities are defined as:

$$v_\parallel = \frac{r_\parallel}{\tau}, \tag{4.12}$$

$$v_\perp = \frac{r_\perp}{\tau}. \tag{4.13}$$

4.2.2   Selection of hit pairs

Since we are primarily interested in low energy neutrinos, the muons they produce have short tracks. This limits the distance between two hits. By selecting only those hits that are not too far apart, we can reduce the background while keeping most of the signal.

The largest possible transverse distance between two hits from the same neutrino depends on the absorption length λ of light in water (typically about 60 m). Since Čerenkov photons are emitted under an angle $\theta_{\check{C}}$ (in sea water, $\theta_{\check{C}} \approx 42°$), they cannot reach an OM further than a few times $\lambda \sin\theta_{\check{C}}$ from the track. The largest possible transverse distance between two photon hits is twice this value.

The probability of large transverse distances between two hits is further limited by the $1/r$ dependence of the photon flux on the distance r to the neutrino track.

The maximum longitudinal distance between two hits is not only determined by the absorption length λ, but also by the muon range L_μ (a few to a few hundred metres, depending on the muon energy). We will therefore perform separate cuts on $r_\parallel$ and $r_\perp$:

$$
\begin{cases}
r_\parallel < r_{\parallel\max}, \\
r_\perp < r_{\perp\max}.
\end{cases}
\tag{4.14}
$$

The values of $r_{\parallel\max}$ and $r_{\perp\max}$ can be determined according to the properties of the background and the signal under investigation.

A further cut can be made on the time difference τ. The maximum time difference that is possible between two hits originating from the same muon, is r/v_g, where v_g is the group velocity of light in water, the smallest velocity involved. Thus, the cut on τ becomes:

$$
|\tau| < \frac{r}{v_g}.
\tag{4.15}
$$

In particular, this last cut implies that the two hits must not be observed in one and the same PMT. Since in that case v is 0, whatever the time difference between the two hits, no useful information can be extracted from these hit pairs.

Due to the high background rates in the detector, it is impossible to store all data for further analysis. The velocity filter must therefore be applied in real time, and the cuts have to be determined in advance.

4.2.3   Velocity distribution for signal and background

During a period of time, all selected hit pairs are examined, and the longitudinal velocities between the hits are determined. The distribution of $v_\parallel$, which we will denote as $f(v_\parallel)$, has different characteristics for the signal and for each type of background: ^{40}K and other random background, atmospheric neutrinos or atmospheric muons.

Signal

The arrival time of a photon from a given track in a given OM was specified in Eq. 2.9. The time difference between two hits is

$$
\begin{aligned}
\tau &= t_j - t_i \\
&= \frac{1}{c}(z_j - z_i + k(R_j - R_i)) \\
&= \frac{1}{c}(r_\parallel + k\Delta R),
\end{aligned}
\tag{4.16}
$$

where we use the notation $\Delta R = R_j - R_i$. Note that ΔR is not the transverse distance $r_\perp$ between the two OMs, but the difference between the respective distances of the two OMs to the muon track. When considering a muon travelling

in a specific direction, but with an unknown starting point, $r_\parallel$ can be determined, but ΔR cannot. It can vary between $-r_\perp$ and $r_\perp$, depending on the location of the muon track.

From Eqs. 4.12 and 4.16, it follows that

$$v_\parallel = c \frac{r_\parallel}{r_\parallel + k\Delta R}.$$ (4.17)

Without loss of generality, we can order i and j such that $r_\parallel > 0$. The value of $v_\parallel$ is then limited to:

$$c \frac{r_\parallel}{r_\parallel + kr_\perp} \leq v_\parallel \leq c \frac{r_\parallel}{r_\parallel - kr_\perp}.$$ (4.18)

The distribution of $v_\parallel$ for signal hits in the entire detector, $f_S(v_\parallel)$, is the sum of the distributions for each of the OM pairs. Its shape depends on the detector geometry, on water properties, on the distribution of muon track lengths, and on the muon direction.

^{40}K and bioluminescence

For background hits from ^{40}K, any combination of t_i and t_j is possible for two given PMTs, because the hit times are uncorrelated. The value of $v_\parallel$ can be arbitrarily small or large.

At the time scales that are of interest here, the background hits due to bioluminescence are also uncorrelated. As far as the velocity filter is concerned, bioluminescence is undistinguishable from ^{40}K, its only effect being a change in the background count rate. The same applies to dark current in the PMTs and other random optical background.

The shape of $f_B(v_\parallel)$, the distribution of $v_\parallel$ for random background hits, depends on the geometry of the detector, on the background count rate, and on the viewing direction. It can be calculated exactly.

For each value of $v_\parallel$, all combinations of PMTs may contribute to $f_B(v_\parallel)$. Let us consider two PMTs whose positions satisfy the conditions 4.14. We need to know how many hit pairs there are in a time interval T (the duration of the measurement), such that the time difference τ between them satisfies condition 4.15, and such that

$$\frac{r_\parallel}{\tau} \in [v_\parallel, v_\parallel + dv_\parallel].$$ (4.19)

This relation is equivalent to

$$\tau \in \left[\frac{r_\parallel}{v_\parallel + dv_\parallel}, \frac{r_\parallel}{v_\parallel} \right],$$ (4.20)

from which it follows that

$$\tau = \frac{r_\parallel}{v_\parallel}$$ (4.21)

and

$$d\tau = \frac{r_\parallel}{v_\parallel^2} dv_\parallel.$$ (4.22)

The contribution to $f_{\mathrm{B}}(v_\parallel)$ from this particular pair of PMTs is

$$\mathrm{d}N = N_{\mathrm{p}}P(\tau)\mathrm{d}\tau, \tag{4.23}$$

where $P(\tau)$ is the probability density of τ, and N_{p} is the number of pairs, which depends on the count rate f and the duration T of the measurement as $N_{\mathrm{p}} = (fT)^2$.

Since the probability distribution of the time of each hit is flat in $[0, T]$, we find for $P(\tau)$:

$$P(\tau) = \begin{cases} 0 & \tau < -T \\ \frac{1}{T}\left(1 + \frac{\tau}{T}\right) & -T < \tau < 0 \\ \frac{1}{T}\left(1 - \frac{\tau}{T}\right) & 0 < \tau < T \\ 0 & T < \tau \end{cases}, \tag{4.24}$$

Eq. 4.24 can be written as

$$P(\tau) = \frac{1}{T}\left(1 - \left|\frac{\tau}{T}\right|\right), \tag{4.25}$$

provided that $|\tau| < T$. For measurements lasting longer than the time it takes for a photon to cross the detector, the condition $|\tau| < T$ is less strict than the cut applied with 4.15:

$$|\tau| < \frac{r}{v_g}, \tag{4.26}$$

which can in turn be written as

$$\left|\frac{r_\parallel}{v_\parallel}\right| < \frac{r}{v_g}. \tag{4.27}$$

Combining these results, we find that this particular pair of PMTs contributes

$$\mathrm{d}N = f^2\left(T - \left|\frac{r_\parallel}{v_\parallel}\right|\right)\frac{|r_\parallel|}{{v_\parallel}^2}\mathrm{d}v_\parallel, \tag{4.28}$$

provided that 4.27 holds.

The value of $f_{\mathrm{B}}(v_\parallel)$ is none other than the sum of the contributions from all PMT pairs satisfying conditions 4.14:

$$\begin{aligned} f_{\mathrm{B}}(v_\parallel) &= \sum_{\alpha,\beta} \frac{\mathrm{d}N}{\mathrm{d}v_\parallel} \\ &= \frac{f^2}{{v_\parallel}^2}\sum_{\alpha,\beta}\left(T - \left|\frac{r_\parallel}{v_\parallel}\right|\right)|r_\parallel|\,\Theta\left(\frac{r}{v_g} - \left|\frac{r_\parallel}{v_\parallel}\right|\right), \end{aligned} \tag{4.29}$$

where α and β number the PMTs, such that each combination only occurs once, and only if it satisfies 4.14.

It will prove convenient to split $f_{\mathrm{B}}(v_\parallel)$ in two parts:

$$f_{\mathrm{B}}(v_\parallel) = T \cdot f_1(v_\parallel) + f_2(v_\parallel), \tag{4.30}$$

where

$$f_1(v_\parallel) = \frac{f^2}{v_\parallel^2} \sum_{\alpha,\beta} |r_\parallel| \, \Theta\left(\frac{r}{v_g} - \left|\frac{r_\parallel}{v_\parallel}\right|\right) \tag{4.31}$$

and

$$f_2(v_\parallel) = -\frac{f^2}{|v_\parallel|^3} \sum_{\alpha,\beta} r_\parallel^{\,2} \, \Theta\left(\frac{r}{v_g} - \left|\frac{r_\parallel}{v_\parallel}\right|\right). \tag{4.32}$$

For $T \gg 1000$ ns and distances on the scale of ANTARES' dimensions, $f_2(v_\parallel)$ becomes negligible with respect to $T \cdot f_1(v_\parallel)$. This means that, for all practical purposes, the background distribution is a fixed function of $v_\parallel$, scaled linearly with the duration of the measurement.

One particular characteristic of $f_{\mathrm{B}}(v_\parallel)$ is that it is symmetric in $v_\parallel$. Because each combination $\{t_i, t_j\}$ is as probable as $\{t_j, t_i\}$, each time difference τ is as probable as its negative, $-\tau$, and therefore each velocity $v_\parallel$ is as probable as its negative, $-v_\parallel$. This symmetry will be vital in the analysis.

Atmospheric neutrinos

To a very good approximation, the incoming flux of atmospheric neutrinos is expected to be isotropic. Since the neutrino-nucleon cross section is extremely low at the energies that are of interest here, the shielding effect by the Earth is negligible.

The exact shape of the distribution of $v_\parallel$ due to atmospheric neutrinos from a particular direction $\hat{n}_\nu$ will, in general, be different from the distribution due to cosmic neutrinos coming from the direction $\hat{n}$ used by the velocity filter. For neutrinos coming from the direction $-\hat{n}_\nu$, the situation is symmetric with respect to neutrinos coming from $\hat{n}_\nu$. The time differences between hits in a given pair of OMs, due to neutrinos from $-\hat{n}_\nu$, are the opposite of the time differences for neutrinos from $\hat{n}_\nu$. The velocity filter always looks in direction $\hat{n}$, therefore the value of $r_\parallel$ is fixed for each pair of OMs. The $v_\parallel$-distributions due to neutrinos from $\hat{n}_\nu$ and $-\hat{n}_\nu$ are each other's mirror image. Since there are as many neutrinos coming from $\hat{n}_\nu$ as from $-\hat{n}_\nu$, the total distribution $f_\nu(v_\parallel)$ is symmetric in $v_\parallel$.

A possible complication might be that the detector is, by design, slightly more sensitive to upgoing neutrinos than to downgoing ones, which could cause an asymmetry in $f_\nu(v_\parallel)$.

We will ignore atmospheric neutrinos in our analysis, since the small contribution they give to $f(v_\parallel)$ is mostly symmetric.

Atmospheric muons

The flux of atmospheric muons arriving at the detector is sharply peaked at small zenith angles. For larger zenith angles, the muon has to traverse a longer path

through the Earth's atmosphere and through the sea, which makes it much more likely for the muon to be absorbed or to decay before reaching the detector.

Since, in general, the velocity filter does not look exactly at the nadir, the atmospheric muon flux is not symmetric around $\hat{n}$. A similar argument as for atmospheric neutrinos cannot be made. Atmospheric muons will cause an asymmetric distribution $f_A(v_\parallel)$, which is a background to the signal distribution $f_S(v_\parallel)$. Special care has to be taken to take this background into account.

4.2.4 Asymmetry

The distribution of longitudinal velocities that is measured during a period of data taking, $f_O(v_\parallel)$, is, at each value of $v_\parallel$, a stochastic variable fluctuating around a certain value. This value is the sum $f_T(v_\parallel)$ of all contributions from signal, random background and atmospheric muons:

$$f_T(v_\parallel) = f_S(v_\parallel) + f_B(v_\parallel) + f_A(v_\parallel). \tag{4.33}$$

Note that the contribution from combinations of a signal hit with a background hit is again symmetric (due to the random nature of the background), and hardly adds to the already huge background distribution.

In view of the overwhelming excess of background, the signal $f_S(v_\parallel)$ can never be extracted from $f_O(v_\parallel)$. Simply subtracting the known distribution $f_B(v_\parallel)$ is not possible, because this distribution depends on the (*a priori* unknown) background count rate.

But now we can use the symmetry of $f_B(v_\parallel)$, by subtracting the distribution of $f_O(-v_\parallel)$ from $f_O(v_\parallel)$. We define the *asymmetry* $g_O(v_\parallel)$ as:

$$g_O(v_\parallel) = f_O(v_\parallel) - f_O(-v_\parallel). \tag{4.34}$$

Analogously, we define $g_B(v_\parallel)$, $g_S(v_\parallel)$ and $g_A(v_\parallel)$.

Since $f_B(-v_\parallel) = f_B(v_\parallel)$, but $f_{S,A}(-v_\parallel) \neq f_{S,A}(v_\parallel)$, we find:

$$g_B(v_\parallel) = 0, \tag{4.35}$$
$$g_S(v_\parallel) \neq 0, \tag{4.36}$$
$$g_A(v_\parallel) \neq 0. \tag{4.37}$$

By subtracting the mirror image of $f_O(v_\parallel)$ from $f_O(v_\parallel)$ itself, the random background will be eliminated.

The result will still contain a contribution from atmospheric muons. This contribution $g_A(v_\parallel)$ can be determined with the help of simulations, based on the observed primary fluxes. We can then subtract $g_A(v_\parallel)$ from $g_O(v_\parallel)$ to find $g_S(v_\parallel)$.

In the following, we will omit the subscript $_\parallel$ for notational convenience.

4.2.5 Sensitivity

We will now determine how intense a signal should be in order to be detected with 3σ or 5σ confidence level within a given time period, or, conversely, how long it will take to detect a given signal at the 3σ or 5σ level.

The two questions we will address are:

1. Can the atmospheric muons be distinguished from the random background?

2. Can a signal from a cosmic source be observed above the random background and the atmospheric muons?

We divide the relevant range of v into bins, and focus on the k bins that are likely to contain the signal we are looking for. Thus, rather than the continuous functions $f_{S,B,A}(v)$ and $g_{S,B,A}(v)$, we consider the discrete equivalents $F_{S,B,A}(v_i)$ and $G_{S,B,A}(v_i)$. $F(v_i)$ denotes the number of entries in the bin that contains v_i.

After a certain period of data taking, we have observed a distribution $F_O(v_i)$, from which we construct $G_O(v_i)$.

Observing atmospheric muons

Let us assume for the moment that no cosmic sources contribute to $G_T(v_i)$, and investigate whether the contribution from atmospheric muons can be detected amidst the random background.

Let H_B be the hypothesis that only random background is present:

$$H_B : \ G_T(v_i) = G_B(v_i). \tag{4.38}$$

The contribution from atmospheric muons can be detected at the 3σ (5σ) level if H_B can be rejected at the 3σ (5σ) level, i.e. if the confidence level for H_B is smaller than $2.7 \cdot 10^{-3}$ ($5.7 \cdot 10^{-7}$).

We will use Pearson's χ^2 test to determine the confidence level for H_B.

Under hypothesis H_B, we can calculate the χ^2 of this distribution:

$$\chi^2 = \sum_{i=1}^{k} \left(\frac{G_O(v_i) - G_B(v_i)}{\sigma_B(v_i)} \right)^2 . \tag{4.39}$$

$G_B(v_i)$ is equal to 0 for all i.

Assuming that there is only background, $F_O(v_i)$ is a Poisson distributed variable with mean $F_B(v_i)$ and variance $\sigma_F^2(v_i) = F_B(v_i)$. $G_O(v_i)$ is then the difference of the two independent variables $F_O(v_i)$ and $F_O(-v_i)$, hence it follows a Skellam distribution [45]:

$$
\begin{aligned}
P\left(G_B(v_i)\right) \ = \ & e^{-(F_B(v_i)+F_B(-v_i))} \left(\frac{F_B(v_i)}{F_B(-v_i)} \right)^{G_B(v_i)/2} \\
& \times I_{G_B(v_i)}(2\sqrt{F_B(v_i)F_B(v_i)}),
\end{aligned} \tag{4.40}
$$

where $I_a(z)$ is the modified Bessel function of the first kind of order a.

The mean of this distribution is

$$\mu = F_B(v_i) - F_B(-v_i) = 0 \tag{4.41}$$

and its variance is

$$\sigma_{\mathrm{B}}^2(v_i) = F_{\mathrm{B}}(v_i) + F_{\mathrm{B}}(-v_i) = 2F_{\mathrm{B}}(v_i). \tag{4.42}$$

The variance given in Eq. 4.42 includes only the statistical error due to random fluctuations. The systematic error depends on the uncertainty in the random background rate. This rate may fluctuate significantly, as was shown in Chapter 3, but it is easy to keep track of the background rate, and to use the variance resulting from an appropriately scaled $f_{\mathrm{B}}(v)$.

Eq. 4.39 now becomes:

$$\chi^2 = \sum_{i=1}^{k} \left(\frac{G_{\mathrm{O}}(v_i)}{2F_{\mathrm{B}}(v_i)} \right)^2. \tag{4.43}$$

From the value of χ^2, the confidence level (CL) of H_{B} can be calculated with:

$$\mathrm{CL}(\chi^2) = \int_{\chi^2}^{\infty} f_k(z)\mathrm{d}z, \tag{4.44}$$

where $f_k(z)$ is the χ^2 distribution for k degrees of freedom.

Observing cosmic sources

A similar calculation can be performed for the signal from a cosmic neutrino source.

A distribution $F_{\mathrm{O}}(v_i)$ is observed, and $G_{\mathrm{O}}(v_i)$ is constructed from it. The predicted distribution from atmospheric muons, $G_{\mathrm{A}}(v_i)$, is subtracted. Let us call the result $\tilde{G}_{\mathrm{O}}(v_i)$:

$$\tilde{G}_{\mathrm{O}}(v_i) = G_{\mathrm{O}}(v_i) - G_{\mathrm{A}}(v_i). \tag{4.45}$$

Let H_{A} be the hypothesis that there is no cosmic neutrino source, i.e. the observed $G_{\mathrm{O}}(v_i)$ is completely due to random background and atmospheric muons:

$$H_{\mathrm{A}} : \ G_{\mathrm{O}}(v_i) = G_{\mathrm{B}}(v_i) + G_{\mathrm{A}}(v_i). \tag{4.46}$$

A neutrino signal is observed when H_{A} is rejected.

The χ^2 that is calculated from $\tilde{G}_{\mathrm{O}}(v_i)$ is:

$$\chi^2 = \sum_{i=1}^{k} \left(\frac{\tilde{G}_{\mathrm{O}}(v_i) - G_{\mathrm{B}}(v_i)}{\sigma_{\mathrm{B,A}}(v_i)} \right)^2, \tag{4.47}$$

where $\sigma_{\mathrm{B,A}}(v_i)$ now includes both the random background and the atmospheric muons:

$$\sigma_{\mathrm{B,A}}^2(v_i) = \sigma_{\mathrm{B}}^2(v_i) + \sigma_{\mathrm{A}}^2(v_i). \tag{4.48}$$

For the background we find, like before, $\sigma_{\mathrm{B}}^2(v_i) = 2F_{\mathrm{B}}(v_i)$. A similar result follows for the variance of $G_{\mathrm{A}}(v_i)$: $\sigma_{\mathrm{A}}^2(v_i) = F_{\mathrm{A}}(v_i) + F_{\mathrm{A}}(-v_i)$.

The systematic error on $G_A(v_i)$ is more troublesome than that on $G_B(v_i)$. It is mainly due to the uncertainty of the fluxes of the primaries that produce the atmospheric muons. Various authors give different primary fluxes. We have to choose one of these values to evaluate $G_A(v_i)$. When the chosen primary flux is too high or too low, $G_A(v_i)$ will not be appropriately scaled. An overcorrection for the atmospheric muons results in larger values for $\tilde{G}_O(v_i)$, especially in the v-range where the signal is expected. The uncertainty in $G_A(v_i)$ due to the uncertainty in primary fluxes has to be taken into account.

We evaluate this uncertainty by subtracting the $G_A(v_i)$ that results when using a primary proton flux of

$$2.35 \cdot 10^4 \ \mathrm{m}^{-2} \, \mathrm{s}^{-1} \, \mathrm{sr}^{-1} \, \mathrm{GeV}^{-1} \, (E/\mathrm{GeV})^{-2.77} \,,$$

as given in [46], from the $G_A(v_i)$ that results when using a primary proton flux of

$$1.18 \cdot 10^4 \ \mathrm{m}^{-2} \, \mathrm{s}^{-1} \, \mathrm{sr}^{-1} \, \mathrm{GeV}^{-1} \, (E/\mathrm{GeV})^{-2.71} \,,$$

as given in [47]. The difference between the resulting $F_A(v_i)$ and $G_A(v_i)$ distributions is taken as the systematic error. The total $\sigma_A(v_i)$ is now the squared sum of the statistical and systematic errors.

Eq. 4.47 now becomes:

$$\chi^2 = \sum_{i=1}^{k} \left(\frac{\tilde{G}_O(v_i)}{2F_B(v_i) + F_A(v_i) + F_A(-v_i) + \sigma^2_{\mathrm{syst,A}}(v_i)} \right)^2 . \qquad (4.49)$$

The confidence level of H_A is calculated from the observed χ^2. If the confidence level is smaller than $2.7 \cdot 10^{-3}$ ($5.7 \cdot 10^{-7}$), a neutrino source is detected at the 3σ (5σ) level.

4.3   Simulation of event samples

The analysis presented here is based on data simulated with the tools described in Section 2.6.

Data were simulated for each of the categories of events, equivalent to one year of data taking. We will give a brief description of each kind of event sample.

4.3.1   Signal events from specified directions

Muon neutrino events were simulated with GENHEN for RX J1713.7–3946.

When using GENHEN in point mode, the declination of the source is specified, and the hour angle is taken randomly between 0 and 24 hours for each event. The neutrino direction in the detector is calculated from the declination and the hour angle. The resulting data set is therefore equivalent to the data set that would be obtained when following this source for one day.

Neutrino energies are taken from an $E^{-\gamma_{\mathrm{g}}}$ spectrum, with E in the range $[E_{\min}, E_{\max}]$. The spectral index γ_{g} typically has a value of 1.4. This is chosen such that also at high energies sufficient statistics are available.

Since the resulting energy spectrum is not the same as the energy spectrum expected from an astrophysical source, some rescaling has to be performed when using these simulated data. To that end, each event is assigned a generation weight w_{g}, depending on its energy E and neutrino direction $\vec{d}$:

$$w_{\mathrm{g}} = V \cdot \frac{\left(E_{\max}^{1-\gamma_{\mathrm{g}}} - E_{\min}^{1-\gamma_{\mathrm{g}}}\right)}{1 - \gamma_{\mathrm{g}}} E^{\gamma_{\mathrm{g}}} \cdot P_{\oplus}(E, \vec{d}) \cdot \sigma(E) \cdot \rho(\vec{x}) N_A, \tag{4.50}$$

where the respective factors represent the generation volume, the energy phase space, the probability for the neutrino to cross the Earth and reach the generation volume without interactions, the cross section, and the number density of nucleons at the interaction point [48].

At the analysis stage, the generation weight is scaled to a global weight w_{glob}:

$$w_{\mathrm{glob}} = w_{\mathrm{g}} \frac{1}{N_{\mathrm{g}}} T \frac{\mathrm{d}\Phi}{\mathrm{d}E}, \tag{4.51}$$

where N_{g} is the number of generated events, T is the observation time, and $\frac{\mathrm{d}\Phi}{\mathrm{d}E}$ is the neutrino differential flux before penetrating the Earth:

$$\frac{\mathrm{d}\Phi}{\mathrm{d}E} = \Phi_0 \left(\frac{E}{\mathrm{GeV}}\right)^{-\gamma}. \tag{4.52}$$

The global weight is a dimensionless quantity. Applying w_{glob} for each event gives the correct scaling of event rates. Some care must be taken in the evaluation of statistical errors when numbers of events are calculated as sums of weights: the error on $N = \sum w_i$ is not $\sqrt{N}$, but $\sqrt{\sum w_i^2}$.

The neutrino interactions generated with GENHEN were processed with KM3. Only events that caused at least one signal hit were kept for further analysis.

4.3.2 Isotropic neutrino events

Upgoing neutrinos from all directions were simulated for cut optimisation. In this case, azimuth angles are taken randomly between 0 and 2π, and zenith angles are distributed flat in $\cos\theta$.

The generation weight now acquires an additional phase space factor:

$$
\begin{aligned}
w_{\mathrm{g}} &= V \cdot \frac{\left(E_{\max}^{1-\gamma_{\mathrm{g}}} - E_{\min}^{1-\gamma_{\mathrm{g}}}\right)}{1 - \gamma_{\mathrm{g}}} E^{\gamma_{\mathrm{g}}} \cdot 2\pi \left(\cos\theta_{\min} - \cos\theta_{\max}\right) \\
&\quad \times P_{\oplus}(E, \vec{d}) \cdot \sigma(E) \cdot \rho(\vec{x}) N_A,
\end{aligned}
\tag{4.53}
$$

where $\theta_{\min}$ and $\theta_{\max}$ are the minimum and maximum zenith angles, respectively.
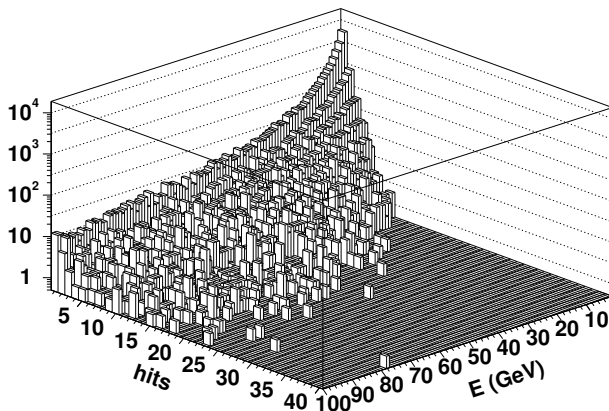
Figure 4.2: *Number of observed hits as a function of neutrino energy.*

All other details of the simulation are the same as in the case of neutrinos from a specified source.

The number of observed hits in an isotropic event sample is shown as a function of energy in Fig. 4.2, where only events with at least one hit were taken into account. A neutrino spectral index of -2 was used for this sample. There are many events with just a few hits, and most of these events are caused by a low energy neutrino.

As could be expected, many of the low energy events do not reach the 5 observed hits that are necessary for the standard track reconstruction. This confirms that for low energies, the standard reconstruction is inefficient.

4.3.3   Background hits

Normally, KM3 can simulate ^{40}K hits in addition to hits from muons and showers. Since in our analysis an analytic expression can be used to evaluate the effect of this background, it was not necessary to include ^{40}K hits in the event files. Instead, we created a separate set of background hits, which we used only to cross-check the result derived in Eq. 4.29 and to optimise the cuts to be applied in the analysis. By excluding ^{40}K hits from the simulated events, CPU power and disk space can be saved.

Since the expression for $f_B(v)$ in Eq. 4.29 agrees well with the result from simulated ^{40}K hits (see Fig. 4.3), we will only use the exact mathematical formula from now on.

4.3.4   Atmospheric muons

Mass productions of atmospheric muon events are available, which were created using CORSIKA [49]. Simulations have been performed for various types of primaries (H, He, Fe and a few others), various energy intervals, and various zenith angle intervals.
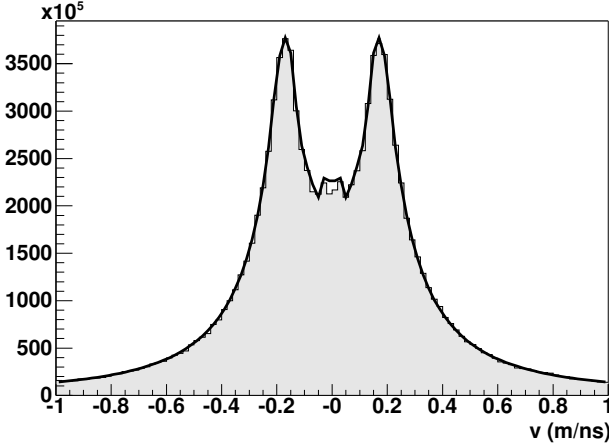
Figure 4.3: $f_{\mathrm{B}}(v)$ *for simulated background hits (shaded area) and according to the analytic expression in Eq. 4.29 (black curve).*

In the following analysis, we restrict ourselves to muons induced by H, He and Fe nuclei. Together, these primaries make up the majority of cosmic rays impinging on the Earth's atmosphere [47]. We also excluded the data for muons with a zenith angle larger than $60°$, since the flux of muons reaching the detector is orders of magnitude lower at these angles than at $\theta \approx 0$.

A weighting scheme similar to that for neutrino events is used: each event is assigned a generation weight

$$
\begin{aligned}
w_{\mathrm{g}} \quad = \quad & \frac{\left(E_{\max}^{1-\gamma_{\mathrm{g}}} - E_{\min}^{1-\gamma_{\mathrm{g}}} \right)}{1 - \gamma_{\mathrm{g}}} E^{\gamma_{\mathrm{g}}} \\
& \times 2\pi \left(\cos\theta_{\min} - \cos\theta_{\max} \right) \cdot A(E, \vec{d}),
\end{aligned} \tag{4.54}
$$

where $A(E, \vec{d})$ is the irradiated area.

In the analysis, each generation weight is scaled to a global weight in the same way as for neutrino events, using the flux of primaries before they impinge on the Earth's atmosphere.

Primaries were generated flat in $\cos\theta$. The primary energies were drawn from an E^{-2} distribution, with an energy range of 1–10^8 GeV.

A differential flux of the form

$$
\frac{\mathrm{d}\Phi}{\mathrm{d}E} = \Phi_0 \left(\frac{E}{\mathrm{GeV}} \right)^{-\gamma} \tag{4.55}
$$

is assumed. The values of Φ_0 and γ are given in Table 4.1. Each event with a primary energy E_i from direction $\vec{d}_i$ is weighted by a factor

$$
w_{\mathrm{glob}} = w_{\mathrm{g}} \frac{1}{N_{\mathrm{g}}} T \frac{\mathrm{d}\Phi}{\mathrm{d}E}. \tag{4.56}
$$

Primary	Φ_0 (m^{-2}s^{-1}sr^{-1}GeV^{-1})	γ
H	$1.18 \cdot 10^4$	2.71
He	$4.75 \cdot 10^3$	2.64
Fe	$1.20 \cdot 10^3$	2.64

Table 4.1: *Differential flux parameters for H and He. Values were taken from [47] and expressed in $m^{-2}s^{-1}sr^{-1}GeV^{-1}$.*

4.4 Results

4.4.1 Cut selection

The effect of cuts on the longitudinal and transverse distances between hits in a pair was studied in a large sample of isotropic upgoing neutrino events and in a large sample of random background hits. In the neutrino event sample, $r_\parallel$ and $r_\perp$ were defined with respect to the neutrino direction. In the background sample, a random viewing direction was chosen for each pair of hits.

The distributions of r, $r_\parallel$ and $r_\perp$, for upgoing neutrinos with energies between 1 and 100 GeV, are shown in Figs. 4.4 and 4.5, along with the same distributions for pure background.

The granularity in these plots, especially in the r distributions, is caused by the detector geometry. The smallest possible distance is that between two OMs in one storey: 1.4 m. The next smallest distance is that between two OMs that are one storey apart: 14.5 m. Multiples of 14.5 m represent hit pairs on the same string, two, three or more storeys apart. At about 60 m, the next string becomes visible, and many more combinations are possible. From this point onwards, the granularity is less pronounced.

(a) Neutrino events
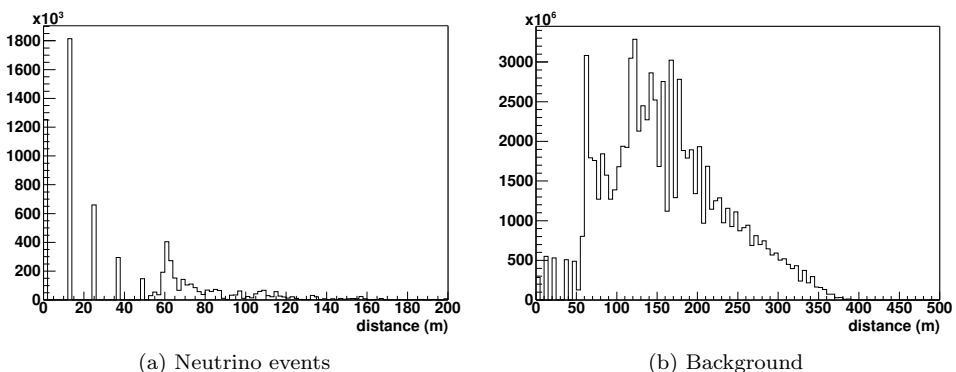
(b) Background

Figure 4.4: *Distances between hits in events with E_ν between 1 and 100 GeV and between background hits. The horizontal scales are different.*

(a) $r_\parallel$, neutrino events

(b) $r_\parallel$, background

(c) $r_\perp$, neutrino events
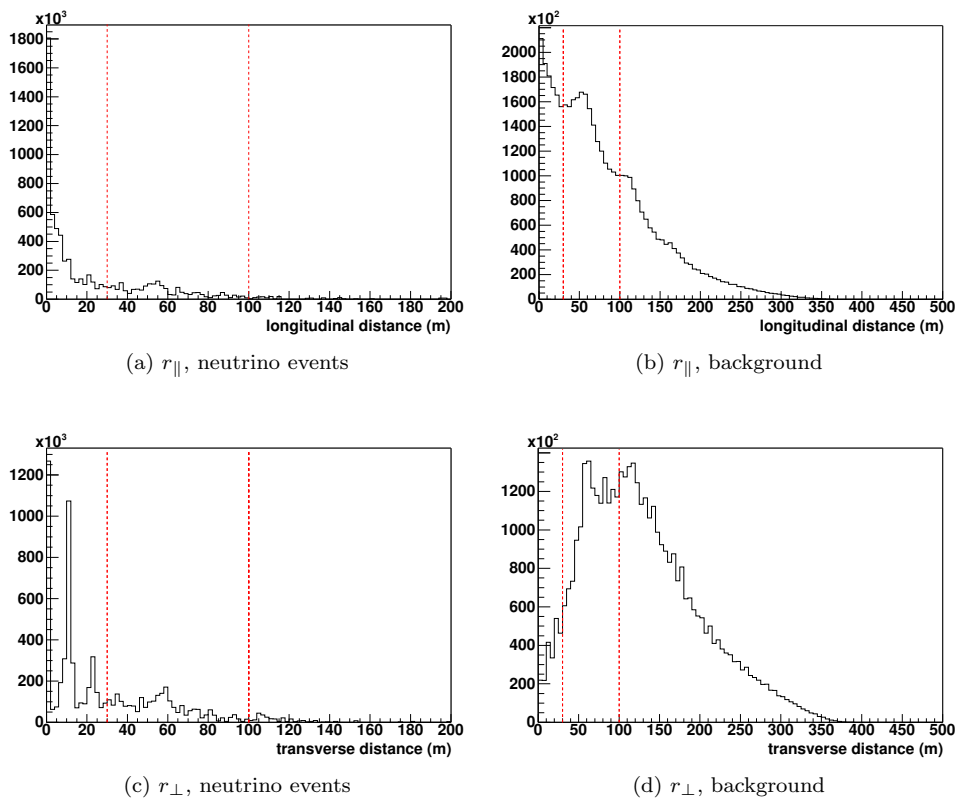
(d) $r_\perp$, background

Figure 4.5: *Longitudinal and transverse distances between hits in events with E_ν between 1 and 100 GeV and between background hits. The horizontal scales are different. The dashed lines indicate the cuts 4.57 and 4.58.*

Based on these results, we select the following values for $r_{\parallel\,\mathrm{max}}$ and $r_{\perp\,\mathrm{max}}$:

$$\begin{cases} r_{\parallel\,\mathrm{max}} = 100 \text{ m}, \\ r_{\perp\,\mathrm{max}} = 100 \text{ m}. \end{cases} \tag{4.57}$$

This eliminates 73% of the background hit pairs, while keeping 94% of the signal hit pairs.

A much stricter cut,

$$\begin{cases} r_{\parallel\,\mathrm{max}} = 30 \text{ m}, \\ r_{\perp\,\mathrm{max}} = 30 \text{ m}, \end{cases} \tag{4.58}$$

eliminates 99.3% of the background hit pairs, while keeping 55% of the signal hit pairs. With this cut, only pairs of hits on one string are kept, where the hits are at most two floors apart.

We will perform the analysis with each of these cuts.

4.4.2 Velocity distributions

Neutrino events were simulated for RX J1713.7–3946, assuming the flux given in Eq. 4.5.

A number of atmospheric muons equivalent to one year of data taking was simulated, using the primary fluxes given in [47]. The events from H, He and Fe were added to yield a total atmospheric muon sample.

For the random background, the analytic expression given in Eq. 4.29 was used, assuming a background count rate of 60 kHz.

These samples were analysed with the velocity filter. The viewing direction was taken to be the neutrino direction for the signal event sample, and drawn randomly along the path of RX J1713.7–3946 across the sky for atmospheric muons and for random background (see Fig. 4.6). This is equivalent to following the source across the sky.

The resulting distributions $F_\mathrm{S}(v_i)$, $F_\mathrm{B}(v_i)$ and $F_\mathrm{A}(v_i)$, as well as the total observed $F_\mathrm{O}(v_i)$, are shown in Fig. 4.7.

As has been discussed before, the background hits give a symmetric distribution in v. The distribution of signal velocities, on the other hand, shows a clear asymmetry, with a peak around 0.2 m/ns. The atmospheric muons show a much broader distribution. The peak at negative v is due to the fact that the source is below the horizon for most of the time, and the atmospheric muons come from above.

The observed $F_\mathrm{O}(v_i)$ cannot be distinguished from $F_\mathrm{B}(v_i)$, since the contributions from $F_\mathrm{S}(v_i)$ and $F_\mathrm{A}(v_i)$ are orders of magnitude smaller.

The asymmetry distributions $G_\mathrm{B}(v_i)$, $G_\mathrm{S}(v_i)$, and $G_\mathrm{A}(v_i)$ are shown in Fig. 4.8.

The total observed distribution $G_\mathrm{O}(v_i)$, shown in Fig. 4.9, is dominated by the contribution from atmospheric muons.

The signal peak is most pronounced between 0.12 and 0.28 m/ns. We will
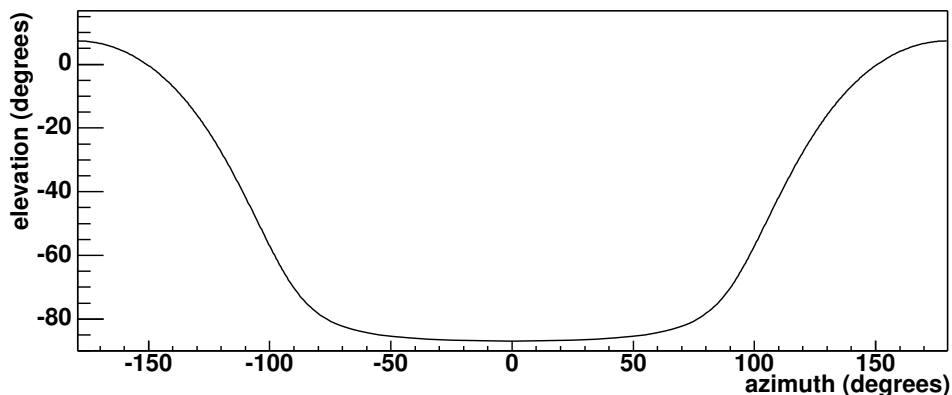
Figure 4.6: *The path of RX J1713.7–3946 across the sky, in horizontal coordinates, as seen from the location of ANTARES.*

(a) Signal: $F_{\mathrm{S}}(v_i)$.

(b) Background: $F_{\mathrm{B}}(v_i)$.

(c) Atmospheric muons: $F_{\mathrm{A}}(v_i)$.

(d) Total: $F_{\mathrm{O}}(v_i)$.
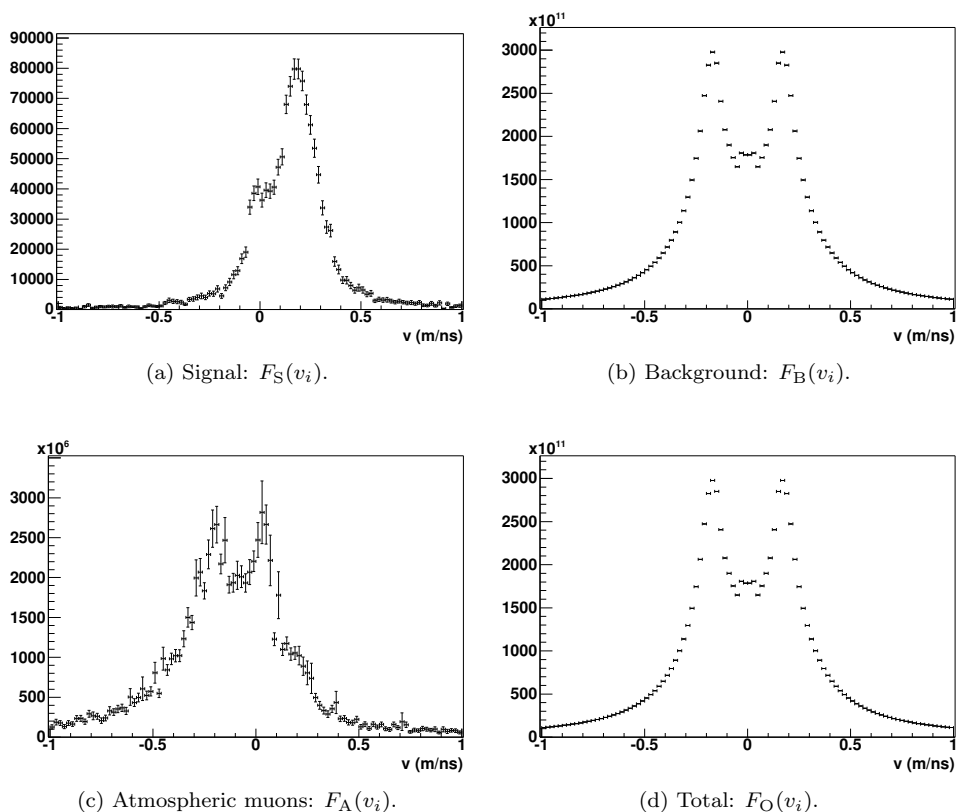
Figure 4.7: *Longitudinal velocity distributions for signal hits, for background hits, for hits from atmospheric muons, and for all hits.*

calculate χ^2 in this interval. With the binning used, this means that the number of bins k is 8.

Calculating χ^2 between 0.12 and 0.28 m/ns under hypothesis H_{B}, we find:

$$\chi^2 = 3.0 \cdot 10^4, \tag{4.59}$$

$$\frac{\chi^2}{k} = 3.8 \cdot 10^3, \tag{4.60}$$

which corresponds to a confidence level for H_{B} of practically 0.

We conclude that the contribution from atmospheric muons can be detected with complete certainty, assuming that the primary fluxes used in this analysis are correct.

Subtracting $G_{\mathrm{A}}(v_i)$ from $G_{\mathrm{O}}(v_i)$ yields the distribution $\tilde{G}_{\mathrm{O}}(v_i)$, which is shown in Fig. 4.10.

(a) Signal: $G_S(v_i)$.

(b) Background: $G_B(v_i)$.

(c) Atmospheric muons: $G_A(v_i)$.
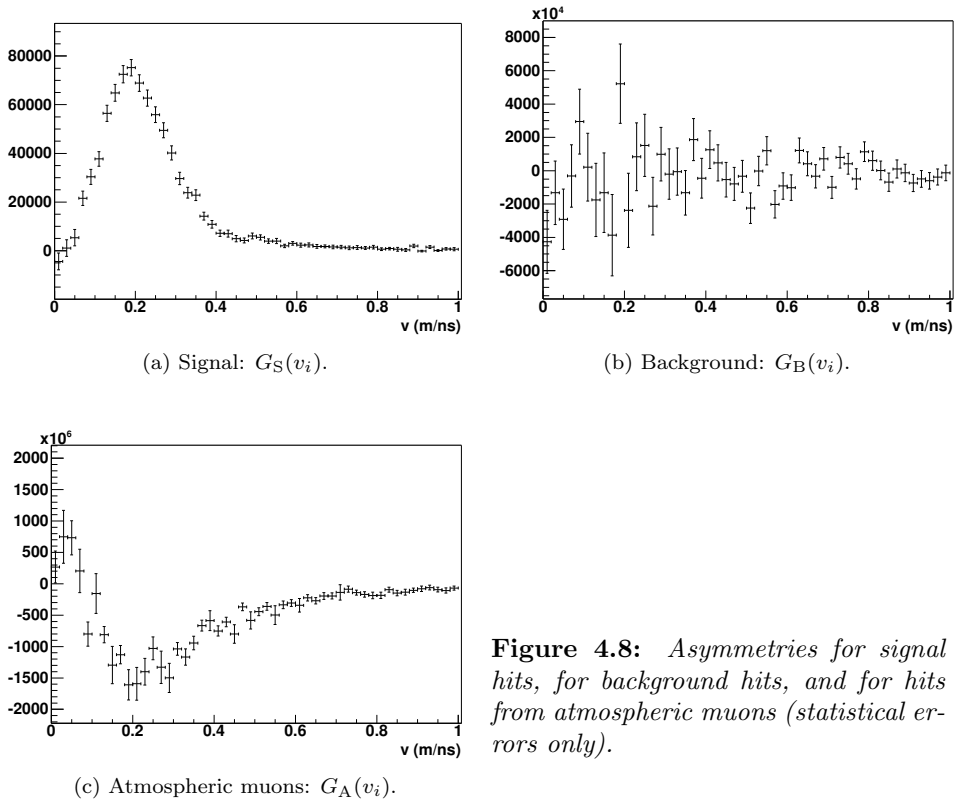
Figure 4.8: *Asymmetries for signal hits, for background hits, and for hits from atmospheric muons (statistical errors only).*
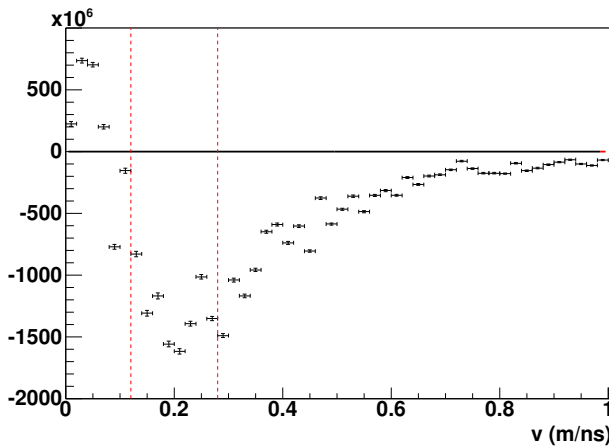
Figure 4.9: *The total observed distribution $G_O(v_i)$. The error bars indicate the statistical error on the background.*
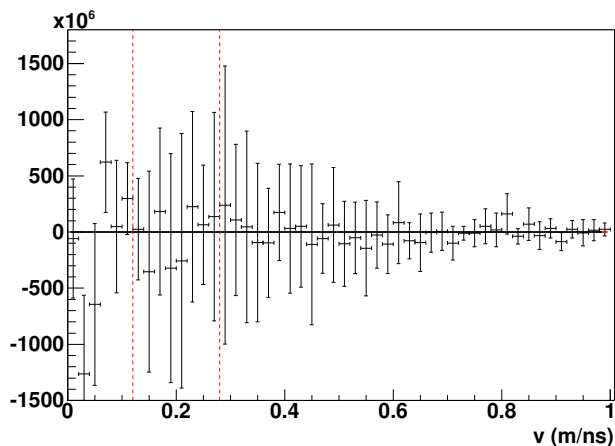
Figure 4.10: *The total observed distribution $\tilde{G}_O(v_i)$, which results after subtracting $G_A(v_i)$ from $G_T(v_i)$. Errors include systematics.*

The χ^2 under hypothesis H_A, evaluated between 0.12 and 0.28 m/ns, yields:

$$\chi^2 \;=\; 4.8 \cdot 10^{-1}, \tag{4.61}$$

$$\frac{\chi^2}{k} \;=\; 6.0 \cdot 10^{-2}, \tag{4.62}$$

corresponding to a confidence level for H_A of 1.0. The signal cannot be detected.

For a 3σ (5σ) discovery, a larger flux from the cosmic neutrino source is needed. In Fig. 4.11, $\tilde{G}_O(v_i)$ is shown for fluxes of

$$3.1 \, (E/\mathrm{GeV})^{-2.2} \;\; \mathrm{m}^{-2}\,\mathrm{s}^{-1}\,\mathrm{GeV}^{-1}$$

(a) 3σ: $C = 3.1 \cdot 10^{-1}$
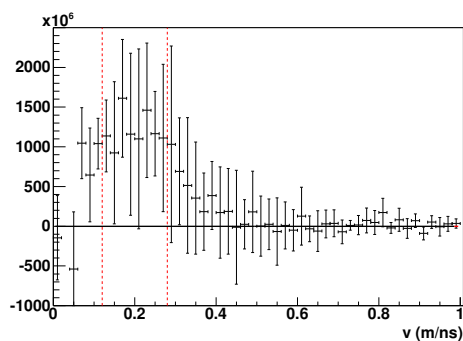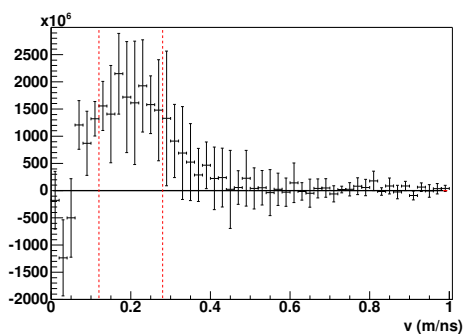
(b) 5σ: $C = 4.2 \cdot 10^{-1}$

Figure 4.11: *The total observed distribution $\tilde{G}_O(v_i)$, for two different fluxes of the form $C \cdot 10^{-2} \left(\frac{E}{\mathrm{GeV}}\right)^{-2.2} \; m^{-2}\, s^{-1}\, sr^{-1}\, GeV^{-1} \, (E/GeV)^{-2.2}$, detectable at the 3σ and 5σ level.*

(a) Signal: $F_S(v_i)$.

(b) Background: $F_B(v_i)$.

(c) Atmospheric muons: $F_A(v_i)$.

(d) Total: $F_O(v_i)$.
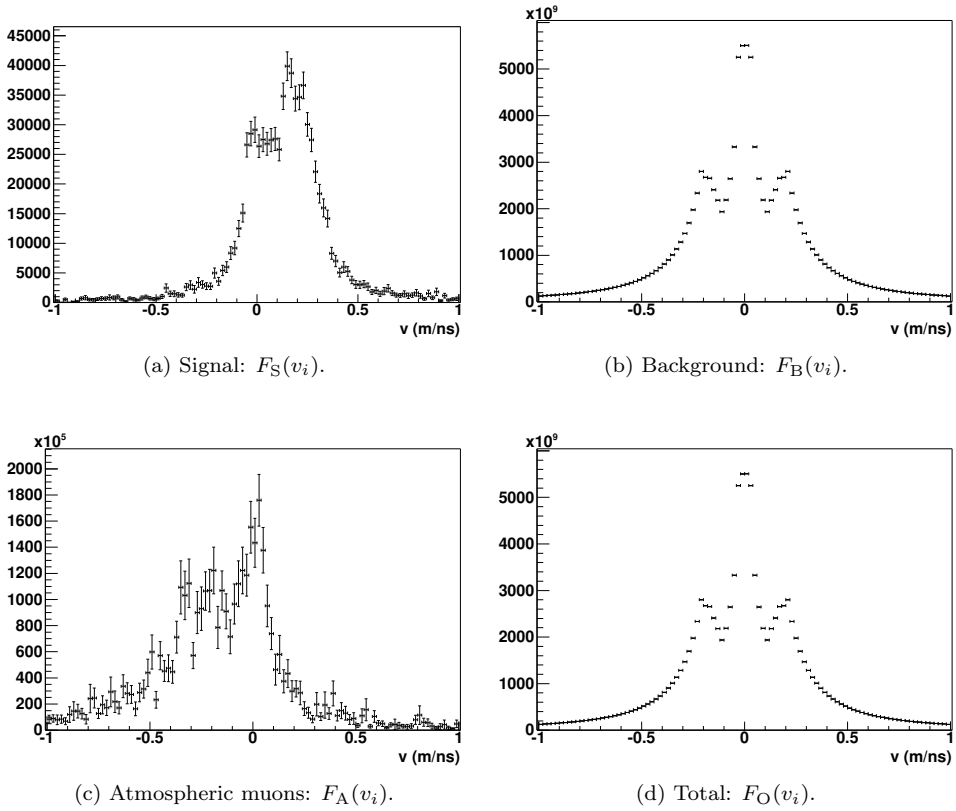
Figure 4.12: *Longitudinal velocity distributions for signal hits, for background hits, for hits from atmospheric muons, and for all hits, using the strict cut $r_\parallel < 30$ m and $r_\perp < 30$ m.*

and

$$4.2\,(E/\text{GeV})^{-2.2}\ \text{m}^{-2}\,\text{s}^{-1}\,\text{GeV}^{-1},$$

that is, $1.1 \cdot 10^3$ ($1.5 \cdot 10^3$) times as large as the predicted flux. For these fluxes, the signal can be detected at the 3σ (5σ) level with a probability of 50%.

Stricter cut

We repeated the entire analysis with the stricter cut specified in Eq. 4.58. In Fig. 4.12, $F_S(v_i)$, $F_B(v_i)$, and $F_A(v_i)$ are shown, together with the total observed $F_O(v_i)$. The distributions $G_B(v_i)$, $G_S(v_i)$, and $G_A(v_i)$ are shown in Fig. 4.13; the total observed $G_O(v_i)$ is shown in Fig. 4.14. The distribution $\tilde{G}_O(v_i)$ is shown in Fig. 4.15.
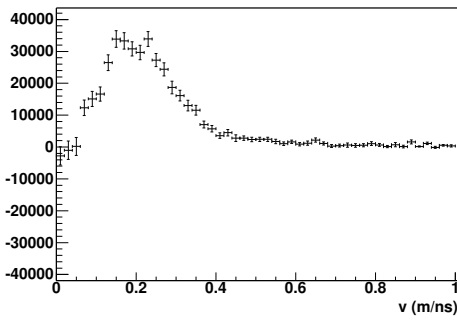
(a) Signal.
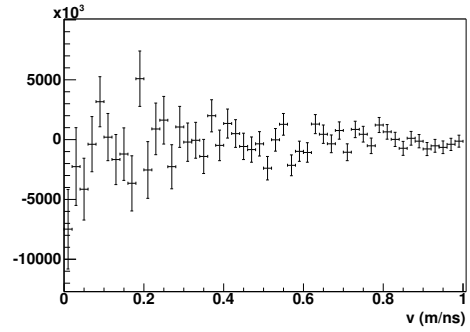
(b) Background.
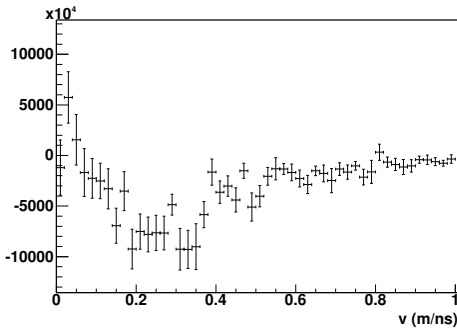
(c) Atmospheric muons.

Figure 4.13: *$G(v_i)$ for signal hits, for background hits, and for hits from atmospheric muons, using the strict cut (statistical errors only).*
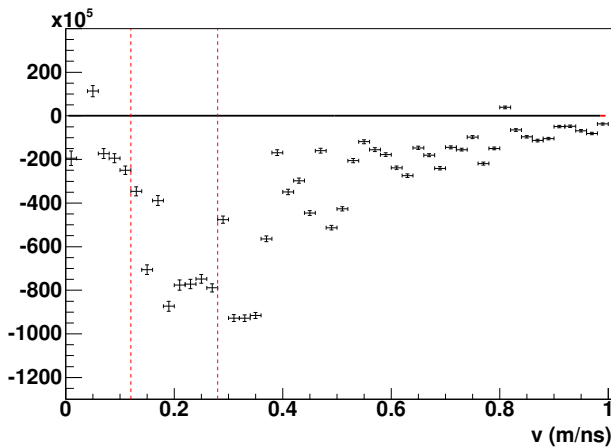
Figure 4.14: *The total observed distribution $G_O(v_i)$, using the strict cut. The error bars indicate the statistical error on the background.*
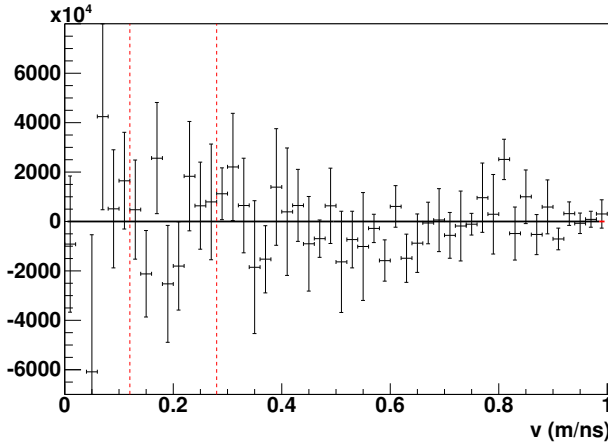
Figure 4.15: *The total observed distribution $\tilde{G}_O(v_i)$, using the strict cut (systematic errors included).*

The χ^2 under H_A, evaluated between 0.12 and 0.28 m/ns, yields:

$$\chi^2 \quad = \quad 7.2 \tag{4.63}$$

$$\frac{\chi^2}{k} \quad = \quad 9.0 \cdot 10^{-1}, \tag{4.64}$$

corresponding to a confidence level for H_A of $5.1 \cdot 10^{-1}$. This is still perfectly compatible with H_A; the signal cannot be observed using this stricter cut either.

For a 50% probability of a 3σ (5σ) discovery, a flux of

$$1.6 \cdot 10^{-1} \, (E/\text{GeV})^{-2.2} \ \text{m}^{-2} \, \text{s}^{-1} \, \text{GeV}^{-1}$$

c.q.

$$2.4 \cdot 10^{-1} \, (E/\text{GeV})^{-2.2} \ \text{m}^{-2} \, \text{s}^{-1} \, \text{GeV}^{-1}$$

is required. This is $8.7 \cdot 10^2$ ($1.3 \cdot 10^3$) times larger than the predicted flux.

4.5 Discussion

With the velocity filter described in this chapter, a flux as predicted for Supernova Remnant RX J1713.7–3946 is not visible. However, the sensitivity may be improved a bit by reducing the systematic error on the contribution from atmospheric muons. One could, for instance, measure $G_O(v_i)$ while looking in a direction where no source is expected, but at the same declination as the source under investigation. Following this point for 24 hours will give a direct estimate of $G_A(v_i)$, without the need to evaluate the primary flux and to perform simulations.

Furthermore, the analysis presented here did not take into account electron neutrinos, tau neutrinos or neutral current interactions. All of these give rise to light in the detector, and the total signal will be larger than what we assumed here. These effects will not make fluxes of the order of

$$10^{-4} \, (E/\text{GeV})^{-2.2} \ \text{m}^{-2} \, \text{s}^{-1} \, \text{GeV}^{-1}$$

detectable at the 3σ level, however.

In a standard point source search using reconstructed muon events, one can observe a flux of about

$$10^{-3}\,(E/\text{GeV})^{-2}\ \text{m}^{-2}\,\text{s}^{-1}\,\text{GeV}^{-1},$$

at the 5σ level, after two years of data taking [18]. The velocity filter is about two orders of magnitude less sensitive than the standard method.

Nevertheless, using the velocity filter to follow a couple of promising sources, such as RX J1713.7–3946, is still advisable, as one never knows what surprises may yet be in store. Should a higher neutrino flux unexpectedly be emitted, then it can be detected by the velocity filter. Moreover, several scenarios can be imagined in which the velocity filter is competitive with the standard search method: for instance, a neutrino energy spectrum that is steeper than E^{-2}, or a cutoff above the energies at which reconstruction becomes efficient. Obviously, this is highly speculative. But at any rate, if neutrino signals are observable, the low energy end is worth investigating too.

Another interesting application of the velocity filter could be the detection of transient sources.

As a crude approximation, the error on the background, $\sigma_{\text{A,B}}$, decreases with the square root of the observation time T. For a steady source, the value of $G_{\text{S}}(v_i)$ decreases linearly with T. For shorter observation times, higher fluxes are needed for a 5σ discovery of the signal above the optical and atmospheric background. In Fig. 4.16, the flux needed for a 5σ discovery is shown as a function of T. The flux from RX J1713.7–3946 is also indicated in this figure.

For transient sources, on the other hand, the value of $G_{\text{S}}(v_i)$ does not depend on the observation time, provided that the entire burst, flare, or whatever other transient event one wishes to study, is fully contained in the observation window. By decreasing T, the ratio of $G_{\text{S}}(v_i)$ to $\sigma_{\text{A,B}}$ increases as $T^{-1/2}$.

A serious issue in this application of the velocity filter is the timing: the variability in photons need not be synchronous with the variability in neutrinos. If
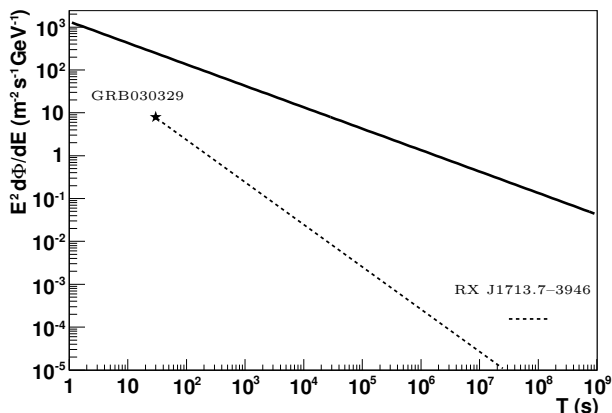
Figure 4.16: *Flux required for a 5σ discovery as a function of observation time T (solid line). The flux from RX J1713.7–3946 and the effective flux from GRB030329 are also indicated (dashed lines). The star represents the true flux and duration of GRB030329.*

one chooses a small time window for the observation, there is a risk of missing the neutrino signal altogether. If the time window is larger than the duration Δt of the transient event, the neutrino signal will be diluted: the 'effective flux' (the average number of photons per unit time) decreases linearly with the observation time:

$$\frac{\mathrm{d}\Phi_{\text{eff}}}{\mathrm{d}E_{\nu_\mu}} = \frac{\mathrm{d}\Phi}{\mathrm{d}E_{\nu_\mu}} \cdot \frac{\Delta t}{T}. \tag{4.65}$$

Consider, as an example, the gamma-ray burst GRB030329 and the associated supernova SN2003dh. The duration of this burst was 30 seconds. In [44], a neutrino flux of about

$$8\,(E/\mathrm{GeV})^{-2}\ \mathrm{m}^{-2}\,\mathrm{s}^{-1}\,\mathrm{GeV}^{-1}$$

is predicted for this source. The effective flux for GRB030329 is indicated in Fig. 4.16.

Using an observation interval of 4 minutes, an effective flux of

$$9 \cdot 10^1\,(E/\mathrm{GeV})^{-2}\ \mathrm{m}^{-2}\,\mathrm{s}^{-1}\,\mathrm{GeV}^{-1}$$

is needed for a 5σ discovery. For GRB030329, this corresponds to a flux of

$$7 \cdot 10^2\,(E/\mathrm{GeV})^{-2}\ \mathrm{m}^{-2}\,\mathrm{s}^{-1}\,\mathrm{GeV}^{-1}.$$

The method outlined in [44], a search for reconstructed muon events where the known direction of the GRB is used, requires a flux of about

$$1 \cdot 10^2\,(E/\mathrm{GeV})^{-2}\ \mathrm{m}^{-2}\,\mathrm{s}^{-1}\,\mathrm{GeV}^{-1}.$$

The velocity filter is about one order of magnitude less sensitive.

The flux from GRB030329 is one or two orders of magnitude too small to be detected. The sensitivity of the velocity filter can be enhanced by reducing the systematic error on $G_{\text{A}}(v_i)$. Another possibility is to observe a large number of GRBs, and to add the $\tilde{G}_{\text{O}}(v_i)$ distributions.

A final application of the velocity filter could be the detection of neutrinos created in the process of neutralino annihilation. For sufficiently low neutralino masses, the resulting neutrino energy falls below the threshold for reconstruction, while the velocity filter is still sensitive to the directionality of the neutrino flux. The filter could be set up to follow the Sun or the Galactic centre, or even to look at the centre of the Earth.

We can conclude that, although neutrino fluxes as expected from currently known objects are too small to be detected by the velocity filter, the difference is not so large that it should discourage all further investigation. In the future, larger detectors and better noise reduction may bring cosmic sources within reach of the velocity filter.

Bibliography

[1] V. F. Hess, Messungen der Durchdringenden Strahlung bei zwei Freibal-lonfahrten, Mitteilungen aus dem Institut für Radiumforschung, Aus den Sitzungsberichten der kaiserlichen Akademie der Wissenschaften in Wien, Mathematisch-naturwissenschaftliche Klasse CXX (1911) 1.

[2] K. Greisen, End to the Cosmic-Ray Spectrum?, Phys. Rev. Lett. 16 (1966) 748.

[3] B. Zhang and P. Mészáros, Gamma-Ray Bursts: Progress, Problems & Prospects, Int. J. Mod. Phys. A 19 (2004) 2385.

[4] K. Hirata *et al.*, Observation of a Neutrino Burst from the Supernova SN1987A, Phys. Rev. Lett. 58 (1987) 1490.

[5] The Super-Kamiokande collaboration, A. Okada, Searches for Astronomical Neutrino Sources and WIMPs with Super-Kamiokande, `astro-ph/0007003`.

[6] The SNO collaboration, J. Boger *et al.*, The Sudbury Neutrino Observatory, Nucl. Inst. & Meth. A 449 (2000) 172, `nucl-ex/9910016`.

[7] B. T. Cleveland *et al.*, Measurement of the Solar Electron Neutrino Flux with the Homestake Chlorine Detector, Astrophys. J. 496 (1998) 505.

[8] E. Andres *et al.*, The AMANDA Neutrino Telescope: Principle of Operation and First Results, Astroparticle Phys. 13 (2000) 1, `astro-ph/9906203`.

[9] The IceCube collaboration, A. Karle, IceCube — The Next Generation Neu-trino Telescope at the South Pole, Nucl. Phys. B (Proc. Suppl.) 118 (2003) 388, `astro-ph/0209556`.

[10] I. A. Belolaptikov *et al.*, The Baikal Underwater Neutrino Telescope: Design, Performance, and First Results, Astroparticle Phys. 7 (1997) 263.

[11] The ANTARES collaboration, E. Aslanides *et al.*, A Deep Sea Telescope for High Energy Neutrinos, `astro-ph/9907432`.

[12] K. S. Capelle *et al.*, On the Detection of Ultra High Energy Neutrinos with the Auger Observatory, Astroparticle Phys. 8 (1998) 321, `astro-ph/9801313`.

[13] The ANTARES collaboration, P. Amram *et al.*, The ANTARES Optical Module, Nucl. Inst. & Meth. A 484 (2002) 369, `astro-ph/0112172`.

[14] Copyright IFREMER.

[15] A. Oppelt, Detection of the Moon Shadow, internal note Phys/2001-012, ANTARES (2001).

[16] A. Heijboer, Observing the Moon Shadow, internal note Phys/2005-004, ANTARES (2005).

[17] M. de Jong, The ANTARES Trigger Software, internal note Soft/2005-005, ANTARES (2005).

[18] A. Heijboer, Track Reconstruction and Point Source Searches with ANTARES, Ph.D. thesis, Universiteit van Amsterdam, Amsterdam (2004).

[19] D. J. Bailey, Monte Carlo Tools and Analysis Methods for Understanding the ANTARES Experiment and Predicting its Sensitivity to Dark Matter, Ph.D. thesis, University of Oxford, Oxford (2002).

[20] G. Ingelman, A. Edin and J. Rathsman, LEPTO 6.5 - A Monte Carlo Generator for Deep Inelastic Lepton-Nucleon Scattering, Comp. Phys. Comm. 101 (1997) 108, `hep-ph/9605286`.

[21] P. Antonioli *et al.*, A Three-dimensional Code for Muon Propagation through the Rock: MUSIC, Astroparticle Phys. 7 (1997) 357, `hep-ph/9705408`.

[22] S. Navas and L. Thompson, KM3 User Guide and Reference Manual, internal note Soft/1999-011, ANTARES (1999).

[23] J. Brunner, GEASIM (2000), `http://antares.in2p3.fr/internal/software/geasim.html`.

[24] A. G. Dickson and C. Goyet (eds.), Handbook of Methods for the Analysis of the Various Parameters of the Carbon Dioxide System in Sea Water; version 2, DOE (1994), ORNL/CDIAC-74, `http://andrew.ucsd.edu/co2qc/handbook/0content.pdf`.

[25] G. Audi *et al.*, The NUBASE Evaluation of Nuclear and Decay Properties, Nucl. Phys. A 729 (2003) 3.

[26] J. Brunner, Simulation of ^{40}K Signals, internal note Site/1999-002, ANTARES (1999).

[27] J. Brunner, Upgrade of ^{40}K Simulation, internal note Site/2006-005, ANTA-RES (2006).

[28] Scripps Institution of Oceanography, Bioluminescence Questions and Answers, `http://siobiolum.ucsd.edu/Biolum_q&a.html`.

[29] P. J. Herring, Systematic Distribution of Bioluminescence in Living Organisms, J. Biolum. Chemilum. 1 (1987) 147.

[30] BBC Natural History Unit, The Blue Planet: The Deep (2001).

[31] P. J. Herring, How to Survive in the Dark: Bioluminescence in the Deep Sea, Sym. Soc. Exp. Biol. 39 (1985) 323.

[32] O. Shimomura, Bioluminescence in the Sea: Photoprotein Systems, Sym. Soc. Exp. Biol. 39 (1985) 351.

[33] J. Hastings, Biological Diversity, Chemical Mechanisms, and the Evolutionary Origins of Bioluminescent Systems, J. Mol. Evol. 19 (1983) 309.

[34] S. D. Miller *et al.*, Detection of a Bioluminescent Milky Sea from Space, Proc. Nat. Acad. Sci. USA 102 (2005) 14181.

[35] T. Legou *et al.*, Clock Distribution System PSL & MIL Status Report, internal note Elec/2003-002, ANTARES (2003).

[36] A. Defant, Über Interne Wellen, Besonders Solche mit Gezeitencharakter, Ocean Dynamics 5 (1952) 231.

[37] J. Rohr *et al.*, Bioluminescence Flow Visualization in the Ocean: an Initial Strategy Based On Laboratory Experiments, Deep-Sea Res. 49 (2002) 2009.

[38] R. May, How many species are there on earth?, Science 247 (1988) 1441.

[39] M. de Jong, Status of Readout, Coll. Meeting, Sheffield (2003), `http://antares.in2p3.fr/internal/minutes/collaboration/coll-030618/mjg1.ps`.

[40] K. Nealson and J. Hastings, Bacterial Bioluminescence: Its Control and Ecological Significance, Microbiol. Rev. 43 (1979) 496.

[41] T. Chiarusi, Environmental Parameters and Water Characteristics from Deep-Sea Surveys at the NEMO Sites. In: *Proceedings of the 29th International Cosmic Ray Conference*, p. 291.

[42] T. K. Gaisser, Cosmic Rays and Particle Physics, Cambridge University Press, Cambridge (1991).

[43] M. L. Costantini and F. Vissani, Expected Neutrino Signal from Supernova Remnant RX J1713.7-3946 and Flavor Oscillations, `astro-ph/0411761 v2`.

[44] M. C. Bouwhuis, Detection of Neutrinos from Gamma-Ray Bursts, Ph.D. thesis, Universiteit van Amsterdam, Amsterdam (2005).

[45] J. G. Skellam, The Frequency Distribution of the Difference between Two Poisson Variates Belonging to Different Populations, J. Roy. Stat. Soc. A Sta. 109 (1946) 296.

[46] B. Wiebel-Sooth, P. L. Biermann and H. Meyer, Cosmic Rays. VII. Individual Element Spectra: Prediction and Data, `astro-ph/9709253`.

[47] J. R. Hörandel, On the Knee in the Energy Spectrum of Cosmic Rays, Astroparticle Phys. 19 (2003) 193.

[48] J. Brunner, Updated Tag List for the New ANTARES Event Format, internal note Soft/1999-003, ANTARES (1999).

[49] D. Heck *et al.*, CORSIKA: A Monte Carlo Code to Simulate Extensive Air Showers, Forschungszentrum Karlsruhe GmbH, Karlsruhe (1998).

Summary

In the early 20th century, it was discovered that highly energetic particles coming from space bombarded the Earth's atmosphere. This discovery opened up a new field of astronomy, as charged particles now formed another source of knowledge about cosmic processes, alongside photons. The study of these cosmic rays has yielded valuable insights.

However, both photons and charged particles present some drawbacks in their use as carriers of information from distant objects. They can be absorbed in gas clouds and other interstellar matter, and at higher energies, they can interact with visible light or with the cosmic microwave background radiation. These effects limit the distance they can travel. Moreover, charged particles are deflected by magnetic fields, so that it is impossible to pinpoint their origin.

Neutrinos do not suffer from these effects. Since they only undergo weak interactions, they can cross large amounts of matter before being absorbed. They do not interact with ambient photons. They carry no electric charge, and cannot be deflected by magnetic fields. In short, they can cross very large distances, and always point back straight to their origin. This makes them a valuable tool for astronomers.

The same properties that give neutrinos an advantage over photons and protons make it hard to detect these elusive messengers. Even for considerable neutrino fluxes, a large volume of target material is needed for a few interactions. To this end, large detectors were constructed, usually consisting of a tank filled with water. Neutrino interactions were detected either by observing Čerenkov light emitted by the interaction products, or by measuring changes in chemical composition of the target as a result of nuclear interactions.

As the need for larger detectors increased, it became less practical to construct dedicated tanks of large volume. Instead, neutrino telescopes have been designed, and some already constructed, in natural environments: in deep water, or in the Antarctic ice. These detectors use the surrounding medium as a target. The resulting light is detected with photomultipliers that are deployed in a

three-dimensional array in the medium.

The easiest to reconstruct is the muon neutrino. When it undergoes a charged current interaction, it creates a muon, which can travel hundreds of metres, depending on its energy. As the muon travels faster than the local speed of light, it emits Čerenkov photons under a specific angle with respect to the muon track. From the arrival times of Čerenkov photons in the photomultipliers, the direction of the muon can be reconstructed with good accuracy, and since at these high energies the muon travels in almost the same direction as the neutrino, the source of the neutrino can be pinpointed.

Two major sources of background are muons and neutrinos that are produced in interactions of cosmic rays with the Earth's atmosphere. The muon background is reduced by building a neutrino telescope at a large depth. The water or ice above it shields the detector from the downward muon flux. The background can be further reduced by discriminating between downward going muons, which are most likely atmospheric, and upward going muons, which must be the result of a neutrino that interacts with water, ice or rock after crossing the Earth. An atmospheric neutrino cannot be distinguished from a cosmic neutrino. The atmospheric neutrino flux forms an irreducible background to the relevant signal.

One neutrino telescope that is currently being constructed is the ANTARES detector. It is located in the Mediterranean, some forty kilometres off the French coast. When completed, it will consist of twelve strings that are anchored to the seafloor and kept upright by a buoy attached to the top. To each string, twenty-five triplets of optical modules are attached, at intervals of fourteen and a half metres. An optical module is a strong glass sphere containing a photomultiplier tube as well as the necessary electronics. The signals from the photomultipliers are sent to shore through optical fibres. No offshore triggering is performed; all data are sent to shore for further processing.

The data from all strings in the detector are combined, and the collective data from separate time intervals are sent to separate computers. These so-called time slices are then processed by the triggering and reconstruction software. The trigger algorithm can be adapted to various needs. In its standard implementation, it searches for local coincidences and hits with large amplitudes. These are then clustered using a causality relation, based on the geometry of the detector and the properties of Čerenkov light. Whenever enough hits are found that could be caused by a muon crossing the detector, all data within 2 μs are written to disk.

The standard reconstruction algorithm implements a maximum likelihood fit to determine the parameters of the muon track. The likelihood of the complete set of photon arrival times is expressed as a function of the track parameters; the best estimate is the set of parameters that maximises the likelihood function.

There are two major sources of optical background in ANTARES: the decay of radioactive potassium and bioluminescence. The β-decay of ^{40}K to ^{40}Ca causes a steady background count rate of about 30 kHz in each photomultiplier. On top op that, there is an additional steady background, as well as bursts of higher intensity, emitted by bioluminescent organisms.

Bioluminescence is a very common phenomenon in the deep sea: over ninety

percent of all organisms living in this environment are luminescent. The absence of daylight makes bioluminescent a powerful means to communicate, to find or attract prey, or to distract and hide from predators. The physiological variation between luminescent organisms is enormous. Some animals have luminous cells distributed over their body, others have symbiont glands in which they keep luminescent bacteria. Some start emitting light as a result of shear stress, others have neurological control over the emission. Pulses can last for a few milliseconds or up to several minutes. One thing that most bioluminescent organisms have in common is the wavelength band in which they emit: from 450 to 490 nanometres, the wavelengths at which seawater is most transparent.

The optical background at the location of ANTARES was studied with a prototype sector line. It took data during ninety days, from March to July 2003. Due to a technical problem, no individual photon hits could be recorded, as had been the intention, but it was still possible to measure the count rate at a timescale of tenths of seconds, with an accuracy of 10 kHz.

Various behaviours of the background count rate were observed. There were periods with a quite stable count rate of varying height and occasional bursts of bioluminescence, periods with frequent bursts, and periods with many overlapping bursts. These characteristics are described, at the timescale of a quarter of an hour, by the 'base rate' and the 'burst rate'. The base rate is the background count rate that is exceeded during 95% of the time in a given period. The burst rate is the frequency of bursts in that period. Individual bursts can be distinguished by their steep rise and trailing flank.

The base rate and the burst rate show strong fluctuations over time. During the ninety days of data taking, the base rate varied from 60 kHz to over 350 kHz. The burst rate varied between 0 and 0.8 Hz. Base rate and burst rate were strongly correlated: in periods with many bursts, the base rate was higher. Both base rate and burst rate were correlated with the speed of the water current. The current was measured only during the last two weeks of data taking, but this limited amount of data shows that higher current speeds cause the base rate and the burst rate to increase.

During some periods, the current speed exhibited a periodicity of 17.7 hours, the period of inertial waves at the latitude of ANTARES. This periodicity can be seen by using a fast Fourier transform. The same periodicity can be seen, although less clearly, in the base rate and the burst rate. In addition, there was a variation in bioluminescence at the tidal period of 12.4 hours. Due to the limited time span of these measurements, the resolution of the fast Fourier transform is not very good, and more simultaneous measurements of current speed and bioluminescence are needed for a firm conclusion.

The characteristics of the bioluminescence can be reproduced by simulations, based on a very simple model. Assuming that luminescent organisms float along with the water current and emit flashes of light as they collide with the mechanical structure of the detector, and that a steady bioluminescent contribution to the count rate is also present, the same pattern of steady background and bioluminescent bursts as was observed in the data could be recreated in the simulations.

Even though he model is limited, it confirms the idea that the bursts are caused by macroscopic bioluminescent organisms, and it gives an explanation of the increase of base rate and burst rate with the current speed.

While the trigger algorithm has been shown to be able to handle count rates of up to 600 kHz, bioluminescence forms an unpleasant background for the detection of cosmic neutrinos. There are two ways to deal with this. Either all data are kept, in which case the higher background rate will cause a higher trigger rate and more fake hits that hinder the reconstruction, or photomultipliers measuring a count rate above a certain threshold are temporarily excluded, in which case an extra dead time of up to ten percent is introduced. For future underwater neutrino telescopes, it is recommended to search for a location with less bioluminescent activity.

The main method of detecting cosmic neutrino sources is to reconstruct muons caused by neutrino interactions. When more muons are detected from a certain direction than can be expected from the atmospheric muon and neutrino background, a source is discovered.

It is assumed that neutrino differential fluxes are roughly of the same shape as their photonic counterparts, that is, a power law with a spectral index of about -2. Since the cross section for neutrino interactions and the effective volume both increase linearly with energy, this implies that the interaction rate per energy interval is roughly constant.

Low energy neutrinos are hard, if not impossible, to detect with the standard triggering and reconstruction. The standard trigger algorithm requires at least five local coincidences. Any events with fewer than ten hits will therefore be discarded. Even with a more lenient trigger, at least five hits are still needed for reconstruction, since there are five degrees of freedom that determine the muon track. Low energy neutrinos produce low energy muons, which have short track lengths inside the detector and therefore emit only a little Čerenkov light. The detector efficiency for neutrino energies below 100 GeV is many orders of magnitude smaller than the efficiency for higher energy neutrinos.

A method has been devised to search for a neutrino flux from a given direction, without reconstructing individual muon tracks. This velocity filter is based on the asymmetry in the combinations of photon arrival times caused by a muon.

The filter determines the longitudinal velocity between all pairs of hits, that is, the distance between the two optical modules measured along the neutrino direction divided by the time difference between the two hits. For random background hits, the distribution of longitudinal velocities is symmetric. For signal hits, the properties of Čerenkov light emitted by a muon give rise to an asymmetry.

Since the random background is much larger than the expected signal, the filter considers not the distribution of longitudinal velocities, but rather the asymmetry in this distribution, by subtracting the mirror image of the velocity distribution from the distribution itself. The symmetric contribution from random background is eliminated, and the signal becomes visible.

Another major source of background in this analysis is the contribution from atmospheric muons, which also produce an asymmetric longitudinal velocity dis-

tribution. This contribution has to be estimated by means of simulations and subtracted from the total observed distribution, in order to find the real signal.

The velocity filter was tested on simulated data, assuming a neutrino flux as is expected from Supernova Remnant RX J1713.7–3946. Atmospheric muons were simulated based on observed primary fluxes. For the contribution from random background hits, an analytic expression was used. The atmospheric muons clearly stand out from the random background. The neutrino signal cannot be detected. This is due partly to the large systematic uncertainty on the primary fluxes that determine the longitudinal velocity distribution from atmospheric muons, but mainly to the fact that the expected neutrino flux is too low to be detectable above the statistical error from background and atmospheric muons. A neutrino flux about three orders of magnitude larger than the flux expected from RX J1713.7–3946 can be detected at the 5σ level.

At the moment of writing, five complete ANTARES strings are in operation, and the sixth string is about to be deployed. Downgoing (atmospheric) muons are routinely reconstructed, and the first preliminary reports of observed upgoing muons have been made. The ANTARES detector is approaching the level at which real neutrino astronomy can be done.

SAMENVATTING

In het begin van de twintigste eeuw werd ontdekt dat hoogenergetische deeltjes uit de ruimte de atmosfeer van de Aarde bombarderen. Deze ontdekking vormde het begin van een nieuw vakgebied in de sterrenkunde. Behalve fotonen kon men nu ook geladen deeltjes gebruiken om informatie te verkrijgen omtrent kosmische processen. De studie van deze kosmische straling heeft tot waardevolle inzichten geleid.

Zowel fotonen als geladen deeltjes hebben echter hun beperkingen als dragers van informatie over ver verwijderde objecten. Ze kunnen geabsorbeerd worden in gaswolken en andere interstellaire materie, en bij hogere energieën kunnen ze wisselwerken met zichtbaar licht of met de kosmische microgolfachtergrondstraling. Deze effecten beperken de afstand waarover fotonen en protonen kunnen reizen. Bovendien worden geladen deeltjes afgebogen door magnetische velden, zodat het onmogelijk is hun oorsprong te achterhalen.

Neutrino's hebben geen last van deze effecten. Doordat ze slechts zwakke wisselwerkingen ondergaan, kunnen ze grote afstanden overbruggen zonder geabsorbeerd te worden. Ze wisselwerken niet met fotonen. Ze hebben geen elektrische lading en worden dus niet afgebogen door magneetvelden. Kortom, ze overbruggen grote afstanden en wijzen altijd terug naar hun plaats van herkomst. Dit maakt neutrino's tot een waardevol hulpmiddel voor sterrenkundigen.

Dezelfde eigenschappen die neutrino's een voordeel opleveren boven fotonen en protonen maken het moeilijk deze ongrijpbare boodschappers waar te nemen. Zelfs voor aanzienlijke neutrinofluxen is een doelwit met een groot volume een vereiste voor een paar wisselwerkingen. Voor dit doeleinde zijn grote detectoren gebouwd, die gewoonlijk bestonden uit een met water gevuld vat. Neutrinowisselwerkingen werden gedetecteerd door waarneming van het Čerenkovlicht dat uitgezonden werd door deeltjes die bij de wisselwerking ontstonden, of door het meten van veranderingen in chemische samenstelling van het doelwit, die veroorzaakt werden door wisselwerkingen met atoomkernen.

Naarmate grotere detectoren nodig werden, werd het steeds onhandiger om spe-

ciale vaten met grote volumes te bouwen. In plaats daarvan werden neutrinotelescopen ontworpen, en deels al gebouwd, in natuurlijke omgevingen: diep onder water of in het Antarctische ijs. Deze detectoren gebruiken het omringende medium als doelwit. Het geproduceerde licht wordt waargenomen met fotomultiplicatoren die in een driedimensionaal patroon in het medium aangebracht zijn.

Het muonneutrino is het eenvoudigst te reconstrueren. In een geladen-stroom-wisselwerking creëert het een muon, dat honderden meters kan reizen, afhankelijk van zijn energie. Doordat het muon sneller reist dan de lokale lichtsnelheid, zendt het Čerenkovfotonen uit onder een specifieke hoek met de voortplantingsrichting van het muon. Uit de aankomsttijden van de Čerenkovfotonen in de fotomultiplicatoren kan het door de muon afgelegde pad nauwkeurig worden bepaald, en aangezien bij deze hoge energieën de richting van het muon vrijwel gelijk is aan die van het neutrino, kan de locatie van de bron van het neutrino op deze manier worden vastgesteld.

De achtergrond wordt gevormd door muonen en neutrino's die ontstaan in wisselwerkingen van kosmische straling met de atmosfeer van de Aarde. De achtergrond van muonen kan verkleind worden door de detector op grote diepte te bouwen. Het water of ijs boven de detector vormt dan een schild voor de omlaaggaande muonflux. De achtergrond kan verder teruggebracht worden door een onderscheid te maken tussen omlaaggaande muonen, die zeer waarschijnlijk van atmosferische oorsprong zijn, en omhooggaande muonen, die het product moeten zijn van een neutrino dat wisselwerkt met rots, ijs of water, nadat het de Aarde doorkruist heeft. Een atmosferisch neutrino is niet te onderscheiden van een kosmisch neutrino. De flux van atmosferische neutrino's vormt een niet weg te werken achtergrond voor het relevante signaal.

Eén van de neutrinotelescopen die op dit moment in aanbouw zijn is de ANTARES-detector. Deze ligt in de Middellandse Zee, zo'n veertig kilometer buiten de Franse kust. Wanneer deze detector voltooid is, zal hij bestaan uit twaalf kabels die met een anker op de zeebodem gehouden worden en door een aan het uiteinde bevestigde boei rechtop gehouden worden. Aan elke kabel zijn vijfentwintig drietallen van optische modules bevestigd, op een onderlinge afstand van veertien en een halve meter. Een optische module is een stevige glazen bol die een fotomultiplicator en de benodigde elektronica bevat. De signalen van de fotomultiplicatoren worden door glasvezels naar de vaste wal getransporteerd. Er wordt buitengaats geen selectie van gegevens uitgevoerd; alle gegevens gaan naar de wal om daar verder verwerkt te worden.

De gegevens van alle kabels in de detector worden samengevoegd en alle gegevens in een tijdsinterval worden naar een aparte computer gevoerd. Deze zogeheten tijdschijven worden dan verwerkt door software voor triggering en reconstructie. Het triggeralgoritme kan aangepast worden aan diverse doeleinden. In de standaardimplementatie zoekt het naar lokaal samenvallende treffers en naar treffers met grote amplitudes. Deze worden dan gegroepeerd door middel van een causaliteitsrelatie, die gebaseerd is op de geometrie van de detector en op de eigenschappen van Čerenkovlicht. Wanneer er genoeg treffers gevonden worden die veroorzaakt zouden kunnen zijn door een muon dat door de detector ging, worden

alle gegevens van de omliggende 2 μs opgeslagen.

Het standaard reconstructiealgoritme past een methode van waarschijnlijkheidsmaximalisatie toe om de parameters van het muonspoor te bepalen. De waarschijnlijkheid van de volledige verzameling aankomsttijden van fotonen wordt uitgedrukt als functie van de parameters van het spoor; de beste schatting is dan de verzameling parameters waarvoor de waarschijnlijkheidsfunctie maximaal is.

Er zijn twee belangrijke bronnen van optische achtergrond in ANTARES: het verval van radioactief kalium en bioluminescentie. Het β-verval van ^{40}K naar ^{40}Ca leidt tot een stabiele achtergrondtelsnelheid van ongeveer 30 kHz. Daarbij komt een tweede, eveneens stabiele achtergrond, evenals pieken van hogere intensiteit. Deze bijdragen in de telsnelheid worden veroorzaakt door lichtgevende organismen.

Bioluminescentie is een veel voorkomend verschijnsel in de diepe zee: meer dan negentig procent van de organismen die in deze omgeving leven is lichtgevend. De afwezigheid van daglicht maakt bioluminescentie tot een krachtig middel voor communicatie, voor het zoeken en lokken van prooidieren, en voor het verjagen van of zich verschuilen voor roofdieren. De fysiologische verscheidenheid tussen lichtgevende organismen is enorm. Sommige dieren hebben lichtgevende cellen verspreid over hun lichaam, andere hebben symbiotische klieren waarin ze lichtgevende bacteriën huisvesten. Sommige zenden licht uit als reactie op schuifkrachten, andere hebben neurologische controle over het uitzenden van licht. De pulsen kunnen enkele milliseconden duren of enkele minuten. Eén ding dat de meeste lichtgevende organismen gemeen hebben is het golflengtegebied waarin ze uitzenden: van 450 tot 490 nanometer, de golflengten waarvoor zeewater het meest doorschijnend is.

De optische achtergrond op de locatie van ANTARES is bestudeerd met behulp van een prototype sectorlijn. Deze vergaarde data gedurende negentig dagen, van maart tot juli 2003. Vanwege een technisch probleem konden geen afzonderlijke fotontreffers worden waargenomen, zoals oorspronkelijk de bedoeling was, maar het was wel mogelijk de telsnelheid te meten op de schaal van tienden van een seconde, met een nauwkeurigheid van 10 kHz.

Er werden verschillende patronen in de achtergrondtelsnelheid waargenomen. Er waren perioden met een tamelijk stabiele telsnelheid van variërende intensiteit en enkele bioluminescente pieken, perioden met veelvuldige pieken, en perioden met vele overlappende pieken. Deze karakteristieken worden op de schaal van een kwartier beschreven door de 'basistelsnelheid' en de 'piekfrequentie'. De basistelsnelheid is de achtergrondtelsnelheid die in een gegeven periode gedurende 95% van de tijd wordt overschreden. De piekfrequentie is de frequentie waarmee pieken optreden gedurende deze periode. Individuele pieken kunnen onderscheiden worden door hun steile aanzet en hun langzame afname.

De basistelsnelheid en de piekfrequentie vertonen grote fluctuaties in de tijd. Gedurende de negentig dagen waarin gegevens werden verzameld varieerde de basistelsnelheid tussen 60 kHz en 350 kHz. De piekfrequentie varieerde tussen 0 en 0.8 Hz. Basistelsnelheid en piekfrequentie zijn sterk gecorreleerd: in perioden met veel pieken was de basistelsnelheid hoger. Zowel de basistelsnelheid als de piekfrequentie was gecorreleerd met de stroomsnelheid van het water. De stroom

werd alleen tijdens de laatste twee weken gemeten, maar deze beperkte hoeveelheid gegevens toont aan dat bij hogere stroomsnelheid de basistelsnelheid en de piekfrequentie toenemen.

Tijdens enkele perioden vertoonde de stroomsnelheid een periodiciteit van 17.7 uur, de periode van traagheidsgolven op de breedtegraad van ANTARES. Deze periodiciteit kan gezien worden met behulp van een snelle Fouriertransformatie. Dezelfde periodiciteit is zichtbaar, zij het minder duidelijk, in de basistelsnelheid en in de piekfrequentie. Daarnaast was er een variatie in de bioluminescentie met een periode van 12.4 uur, de periode van de getijden. Vanwege de beperkte tijdsspanne waarin gemeten werd is de resolutie van de Fouriertransformatie niet zo goed, en meer gelijktijdige metingen van stroomsnelheid en bioluminescentie zijn nodig voor een duidelijker conclusie.

De karakteristieken van de bioluminescentie kunnen gereproduceerd worden door simulaties, gebaseerd op een zeer eenvoudig model. Aangenomen dat lichtgevende organismen met het water meedrijven en lichtpulsen uitzenden wanneer ze in botsing komen met de mechanische structuur van de detector, en dat er ook een stabiele biologische component van de telsnelheid is, kunnen dezelfde patronen van stabiele achtergrond en bioluminescente pieken als die in de gemeten telsnelheden ook in de gesimuleerde gegevens gezien worden. Hoewel dit model beperkt is, bevestigt het het idee dat de pieken veroorzaakt worden door macroscopische lichtgevende organismen, en geeft het een verklaring voor de toename in basistelsnelheid en piekfrequentie bij hogere stroomsnelheden.

Hoewel is aangetoond dat het triggeralgoritme telsnelheden tot 600 kHz aankan, vormt bioluminescentie een ongewenste achtergrond voor de detectie van kosmische neutrino's. Er zijn twee manieren om hiermee om te gaan. Ofwel men bewaart alle gegevens, waarbij de hogere achtergrondtelsnelheid een hogere triggerfrequentie veroorzaakt, en meer valse treffers die de reconstructie hinderen, ofwel men sluit fotomultiplicatoren uit zodra ze een telsnelheid hoger dan een bepaalde drempelwaarde meten, waarbij een extra dode tijd van tot tien procent wordt ingevoerd. Voor toekomstige neutrinotelescopen is het verstandig een locatie te zoeken waar de hoeveelheid licht van bioluminescentie kleiner is.

De belangrijkste methode om kosmische neutrinobronnen te detecteren is het reconstrueren van muonen die ontstaan bij neutrinowisselwerkingen. Wanneer er meer muonen uit een bepaalde richting waargenomen worden dan op grond van de achtergrond van atmosferische muonen en neutrino's verwacht kan worden, is er een bron ontdekt.

Men neemt aan dat de differentiële flux van neutrino's ongeveer dezelfde vorm heeft als de bijbehorende differentiële flux van fotonen, dat wil zeggen, een machtswet met een spectraalindex van rond -2. Aangezien zowel de werkzame doorsnede voor neutrinowisselwerkingen als het effectieve volume van de detector lineair toeneemt met de energie, betekent dit dat de interactiesnelheid per energie-interval ongeveer constant is.

Laagenergetische neutrino's zijn moeilijk, zo niet onmogelijk, te detecteren met de standaardmethoden voor triggering en reconstructie. Het standaard triggeralgoritme vereist tenminste vijf lokale coïncidenties. Alle gebeurtenissen met minder

dan tien treffers zullen dus weggegooid worden. Zelfs met een soepeler trigger zijn minstens vijf treffers nodig voor de reconstructie, aangezien er vijf vrijheidsgraden zijn die het spoor van het muon bepalen. Laagenergetische neutrino's produceren laagenergetische muonen, die korte sporen in de detector maken en daardoor slechts weinig Čerenkovlicht uitzenden. De efficiëntie van de detector voor neutrino's met een energie beneden 100 GeV is vele ordes van grootte kleiner dan de efficiëntie voor neutrino's met hogere energie.

Een methode is ontworpen om te zoeken naar een neutrinoflux uit een gegeven richting, zonder sporen van individuele muonen te reconstrueren. Dit snelheidsfilter is gebaseerd op de asymmetrie in de combinaties van aankomsttijden van fotonen die veroorzaakt worden door een muon.

Het filter bepaalt de longitudinale snelheid in alle paren van treffers, dat wil zeggen, de afstand tussen de twee optische modules, gemeten in de richting van het neutrino, gedeeld door het tijdsverschil tussen de twee treffers. Voor willekeurige achtergrondtreffers is de verdeling van longitudinale snelheden symmetrisch. Voor signaaltreffers veroorzaken de geometrie van de detector en de eigenschappen van Čerenkovlicht een asymmetrie.

Omdat de willekeurige achtergrond veel groter is dan het verwachte signaal, bekijkt het filter niet de verdeling van longitudinale snelheden, maar de asymmetrie in die verdeling, door het spiegelbeeld van de verdeling af te trekken van de verdeling zelf. De symmetrische bijdrage van de willekeurige achtergrond wordt zo geëlimineerd, en het signaal wordt zichtbaar.

Een andere belangrijke achtergrond in deze analyse is de bijdrage van atmosferische muonen, die ook een asymmetrische verdeling van longitudinale snelheden veroorzaken. Deze bijdrage moet door middel van simulaties geschat worden en afgetrokken van de waargenomen verdeling om het werkelijke signaal te vinden.

Het snelheidsfilter is getest op gesimuleerde gegevens, waarbij een neutrinoflux werd aangenomen zoals voorspeld voor het supernovarestant RX J1713.7–3946. Atmosferische muonen werden gesimuleerd op basis van waargenomen fluxen van kosmische straling. Voor de bijdrage van de willekeurige achtergrond werd een analytische uitdrukking gebruikt. De atmosferische muonen onderscheiden zich duidelijk van de willekeurige achtergrond. Het neutrinosignaal kan niet waargenomen worden. Dit is gedeeltelijk te wijten aan de grote systematische fout op de flux van de kosmische straling die de verdeling van longitudinale snelheden voor atmosferische muonen bepaalt, maar vooral aan het feit dat de verwachte neutrinoflux te laag is om zichtbaar te zijn boven de statistische fout op de achtergrond. Een neutrinoflux die ongeveer een factor duizend groter is dan de flux die men van RX J1713.7–3946 verwacht, kan op 5σ-niveau gedetecteerd worden.

Op dit moment zijn vijf volledige lijnen van de ANTARES-detector operationeel, en staat de zesde lijn op het punt geïnstalleerd te worden. Omlaaggaande (atmosferische) muonen worden routinematig gereconstrueerd, en de eerste voorlopige meldingen van waargenomen omhooggaande muonen zijn gemaakt. De ANTARES-detector nadert het niveau waarop echte neutrino-astronomie bedreven kan worden.

Dankwoord

Het schrijven van een proefschrift is een langdurige klus, en het is onmogelijk om iedereen die mij de afgelopen jaren inhoudelijk of moreel gesteund heeft persoonlijk te bedanken. Een aantal mensen wil ik hier in het bijzonder noemen.

Mijn promotor, Paul Kooijman, bedank ik voor zijn goede ideeën en zijn waardevolle adviezen. We zijn onderweg een paar van koers veranderd, maar Paul heeft mij geholpen de grote lijn en het einddoel in beeld te houden.

In de eerste jaren van mijn onderzoek was Gert-Jan Nooren mijn dagelijks begeleider. Met hem heb ik, behalve over het onderzoek, urenlang gepraat over alle mogelijke onderwerpen. Ik vind het jammer dat deze samenwerking beëindigd moest worden voordat ik mijn promotie had afgerond.

Ook met de andere collega's in het instituut SAP heb ik een plezierige tijd gehad. Vooral in BBL 764, met mijn kamergenoten Eugène, PC, Emanuele, Federica en Martijn, was het vaak gezellig druk. Daarnaast was de dagelijkse koffie (met koekjes!) een goede gelegenheid om even te ontspannen, en ook op andere momenten was er altijd wel iemand om even over al dan niet werkgerelateerde zaken te kletsen. De legendarische kerstlunches zal ik nooit vergeten!

Een extra woord van dank voor Nick van Eijndhoven. Weliswaar hebben we niet zo nauw samengewerkt als we eigenlijk hadden gewild, maar toch heeft Nick met zijn oprechte enthousiasme mijn motivatie voor het wetenschappelijk onderzoek in stand helpen houden. En die samenwerking halen we nu ruimschoots in!

Een deel van mijn tijd bracht ik door op het Nikhef. Hoewel ik daar, vooral de laatste tijd, niet dagelijks was, heb ik goede herinneringen aan de contacten met de ANTARES-collega's in Amsterdam.

During meetings and shifts, I spent a lot of time with my colleagues from other institutes. Climbing Mount Etna, skiing in Les Houches, a family diner in Moscow, or just having a beer together in the CERN canteen, made these trips abroad very pleasant indeed.

Aan het thuisfront kreeg ik altijd steun, of ik nu met veel plezier over mijn werk vertelde, of, zoals vooral in de laatste maanden, soms wat minder goedgehumeurd

was. Het vertrouwen en de de warme belangstelling die ik van mijn familie kreeg hebben mij veel goed gedaan.

Vooral mijn ouders, die mij van jongs af aan de mogelijkheid hebben gegeven mij te ontplooien en bij wie ik altijd terecht kan voor een goed gesprek, wil ik daarvoor hartelijk bedanken.

Ook mijn vrienden hoorden mijn uiteenzettingen over neutrinoastrofysica en over de voor- en nadelen van een AiO-positie geduldig aan. Van dat laatste zijn ze nu verlost, van het eerste nog niet.

De ereplaats in deze lijst bedankjes is voor mijn vrouw Anita. Zij heeft, al sinds we nog op school zaten en net een stelletje waren, altijd achter mij gestaan. Anita, ik heb enorm veel bewondering voor je doorzettingsvermogen en je gedrevenheid om taken die je op je neemt te voltooien, en ik heb geprobeerd er een voorbeeld aan te nemen. Ik wens je veel succes bij jouw eigen inspanningen op wetenschappelijk terrein, en je mag op net zoveel steun en liefde van mij rekenen als ik van jou heb gekregen!

CURRICULUM VITAE

Ik ben geboren op 4 juni 1977 in Apeldoorn. In deze stad doorliep ik de kleuter- en de basisschool, en haalde ik in 1995 mijn diploma aan het Stedelijk Gymnasium. Daarna vertrok ik naar Utrecht om natuurkunde en geofysica te studeren. Van beide studies haalde ik cum laude de propedeuse, waarna ik mij volledig op de natuurkunde stortte. In 1997 begon ik een studie wijsbegeerte van de exacte wetenschappen.

Intussen was ik voor mijn afstudeeronderzoek natuurkunde terechtgekomen bij de vakgroep Subatomaire Fysica, waar ik onder begeleiding van dr. Nick van Eijndhoven onderzoek deed naar directe fotonen die in quark-gluon-plasma geproduceerd worden. In het kader van dit onderzoek bracht ik enkele bezoeken aan het CERN in Genève. Zowel het CERN als de stad Genève leerde ik in 1999 nog beter kennen als zomerstudent.

In augustus 2000 voltooide ik mijn studie, en behaalde ik cum laude het doctoraal in zowel de theoretische als de experimentele natuurkunde.

In september van dat jaar begon ik als AiO aan de Universiteit Utrecht met het onderzoek waarvan het resultaat in dit proefschrift beschreven is. Dit onderzoek verrichtte ik grotendeels bij de Universiteit Utrecht en bij het Nikhef in Amsterdam, met enkele perioden in Marseille en La Seyne-sur-Mer.